Final Report for
Diode-pumped Laser Altimeter

Contract: NAS5-30882

Reporting Period:
1 June 1990 - 31 March 1993

D. Welford and Y. Isyanova
Schwartz Electro-Optics Inc.
45 Winthrop Street
Concord, MA 01742

Table of Contents

1 Introduction.

In the Phase II proposal, we proposed the following statement of work:

1. Output energy scaling to the 10 mJ level.

   a) Purchase diode laser arrays, drivers and optical components.

   b) Optimise the pumping geometry and resonator for maximum conversion efficiency in TEM_{00}, normal-mode operation.

   c) Investigate the use of Nd:BEL as a means to improve efficiency and/or reduce the spectral requirements of the diode laser array.

2. PTM Q-switch development.

   a) Purchase the Q-switch crystal and its associated components.

   b) Design and fabricate a compact mechanical resonator structure for the PTM Q-switched laser.

   c) Build the Q-switch driver.

   d) Assemble and operate a 1.06 μm Q-switched laser.

3. Technology development for wavelength diversity.

   a) Purchase nonlinear crystals for doubling and sum generation.

   b) Build a second Q-switched laser operating on the 1.32 μm Nd^{3+} transition.

   c) Investigate extracavity doubling of both the 1.06 μm and 1.32 μm Q-switched lasers.

   d) Investigate intracavity sum-frequency generation of 1.06 μm and 1.32 μm Q-switched lasers.

We have been successful in attaining every goal set forth in the original proposal and have performed additional work to expand our knowledge of diode-laser pumping, short Q-switched pulse generation, and efficient harmonic conversion in milli-Joule systems. The remainder of this section provides a short summary of our achievments in each of the areas defined by our original statement of work.

Output energy scaling to the 10 mJ level.

We were able to scale our original pumping geometry to 22.5 mJ, TEM_{00}-mode output energies in 200-μs duration pulses at 1.064 μm in Nd:YAG with slope efficiencies of 23%. 1.32-μm performance was equally impressive at 10.2 mJ output energy with 15% slope efficiency. The same pumping geometry was successfully carried forward to several complex Q-switched laser resonator designs with no noticeble degradation of beam quality. Output beam profiles were consistently shown to have greater than 90% correlation with the ideal TEM_{00}-order Gaussian profile.

Given this level of performance with Nd:YAG, nothing would be gained in efficiency by using Nd:BEL and this material was not persued. Note, that in the meantime Nd:BEL is no longer commercially available.

PTM Q-switch development.

Some difficulties were encounterd with the Q-switch driver and optical damage to laser rods, that limited the pulse energies to the 5-mJ level for the pulse-transmission-mode (PTM), Q-switched laser at 1.064 μm. However, this technique was successful in generating 5-ns duration pulses with nanosecond timing jitter.

Additional work was performed in a comparison study on pulse-reflection-mode (PRM) and passive Q-switching techniques. The PRM Q-switched laser technique generated 8.3 mJ pulses with durations as short as 10 ns. Further development of the PTM Q-switch driver should allow for similar energy extraction, but with the shorter pulse duration and improved timing jitter.

The passively Q-switched laser had a shorter resonator and used F_2^- color-centers in LiF as a saturable absorber. 5-mJ pulses were obtained with durations as short as 2.4 ns. Timing jitter was typically on the order of one microsecond. An additional benefit of this technique was that the laser operated in a single longitudinal mode as a result of the evolutionary dynamics of the laser Q-switching process.

Technology development for wavelength diversity.

We were able to demonstrate frequency doubling of both 1.064 μm and 1.32 μm with conversion efficiencies of 56% in lithium triborate and 10% in rubidium titanyl arsenate, respectively. The input pulse energies were at the milli-Joule level, in both cases. These materials were the most efficient out of five tested at 1.064 μm and three tested at 1.32 μm.

Sum-frequency generation of the 1.064 μm and 1.32 μm radiations was demonstrated in KTP to generate 1.1 mJ of 0.589 μm output with 11.5% conversion efficiency. The conversion efficiency was reduced because the duration of the two input pulses were different by a factor of two. Future work could be expected to push the conversion efficiency to 50% for this process.

2 Normal-Mode Laser Development.

Our proposed pumping geometry was to use a single three-bar stacked, quasi-cw, diode-laser array to pump a 1-cm-long Nd:YAG "rod" (self-imaging D-shaped "rod" as demonstrated in the Phase I effort) and optimize TEM_{00}-mode energy extraction by matching the laser mode volume with the pumped volume of the rod. This provides a single-rod gain-module with 36 mJ of pump laser energy, that can be scaled in energy by adding other modules. The cost reduction in diode laser arrays allowed the use of a five-bar diode-laser array per 1-cm laser "rod" and the combination of two such rods in one gain-module. This improved gain-module design offers:

1) increased pump laser energies of up to 120 mJ per gain-module.
2) cancellation of beam displacement and dispersion effects when the Brewster-angled laser rods are arranged in an opposing configuration (see figure 2.1.).
3) improved overlap of the elliptical TEM_{00}-mode of the laser resonator in the rod with the pumped region. Figure 2.2 illustrates this effect.

The reduction in price of the diode laser arrays was the result of the introduction of products by two new vendors (Laser Diode, Inc. (LDI) and Advanced Opto-Electronics (AOE)) in direct competition Spectra Diode Labs, Inc. (SDL). However, the relative performance of the three products was not adequately defined in the manufacturers' data and we were not able to determine the optimum device for our application. We ordered a three-bar diode-laser array for evaluation from each manufacturer. The choice of three-bar devices left us with more buying power for five-bar devices, while still allowing us to evaluate the thermal performance of the stacking technologies (a single-bar device would not have allowed us to do this).

Our primary requirement was for a high-spectral brightness pump laser. So, our device evaluation concentrated on the spectral and spatial distribution of the diode laser array output. AOE was unable to deliver devices and the LDI device was clearly inferior to the SDL device. All of our laser work was performed using SDL devices.

In summary, the normal-mode laser development consisted of quantifying thermo-optic effects in the laser rod(s) and designing a resonator to ensure TEM_{00}-mode operation. The design uses the laser rod(s) as an aperture(s) to prevent higher-order modes lasing. The correct choice of Brewster-angled orientation allows the TEM_{00}-mode to better overlap the pumped volume in the rod(s).

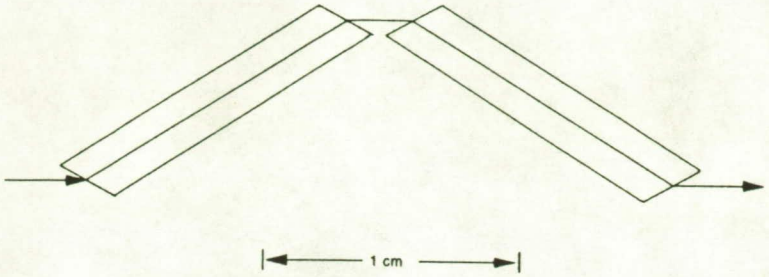

Figure 2.1 Dual Brewster-angled laser rod beam path.

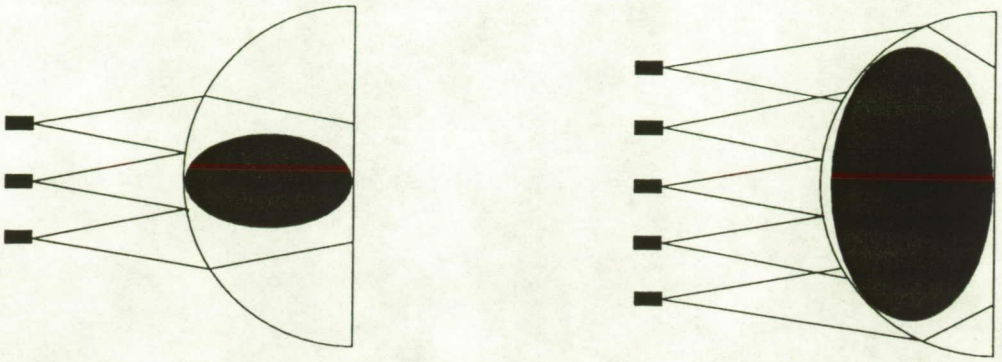

Figure 2.2 Illustration of the overlap of TEM_{00}-modes and pumped regions for three- and five-bar diode-laser arrays.

TEM_{00}-mode operation was obtained at 1.064 μm and 1.32 μm with output powers of 22.5 mJ and 10.5 mJ, respectively, for 120 mJ of incident pump energy or 78 mJ of absorbed pump energy. These output energies represent approximately 80% of the corresponding multi-mode output energies.

2.1 *Quasi-CW Laser Diode Characterization.*

We characterized the spatial and temporal characteristics of the emission spectrum of three-bar diode-laser arrays from two vendors in order to determine their relative merits for transverse optical pumping of Nd:YAG. This characterization was required to determine their spectral/temporal brightness, which is a suitable figure-of-merit when optically pumping laser media. The diode-laser array characteristics were used to choose the vendor for the five-bar diode-laser arrays.

The diode-laser arrays were mounted on thermoelectric coolers, which in turn were mounted to a water-cooled copper plate. The heat load was removed by cooling water from an

SEO designed liquid-to-air heat exchanger based cooling unit. Temperature stabilization to better than 0.1°C was performed with a Marlow Model SE5010 closed-loop temperature controller.

We assembled a spectral diagnostic system consisting of a computer controlled, 0.64-m grating spectrometer with a 1200 gr/mm grating capable of resolving to 0.1 A, outfitted with a fast photomultiplier detection system. The detection system was used with a lock-in amplifier for time-averaged spectral scans and with a transient digitizer for time-resolved spectral measurements.

Output power data.

Our investigation was limited to devices from SDL and LDI. Our third vendor, AOE, was unable to deliver devices. We began by measuring the peak output power as a function of the drive current. The laser diodes were driven with 200 μs rectangular current pulses at pulse repetition rates (p.r.r) up to 100 Hz from a SDL Model 922 driver. The data shown in figures 2.1.1 and 2.2.2 are for a heatsink temperature of 25°C. These data closely match those supplied by the manufacturers.

Threshold current and slope efficiency were similar for both devices. However, the maximum drive current was limited to 60 A (manufacturer's data sheet) for reliable operation of the LDI device, thereby limiting the available peak output power to 55% of that available from the SDL device.

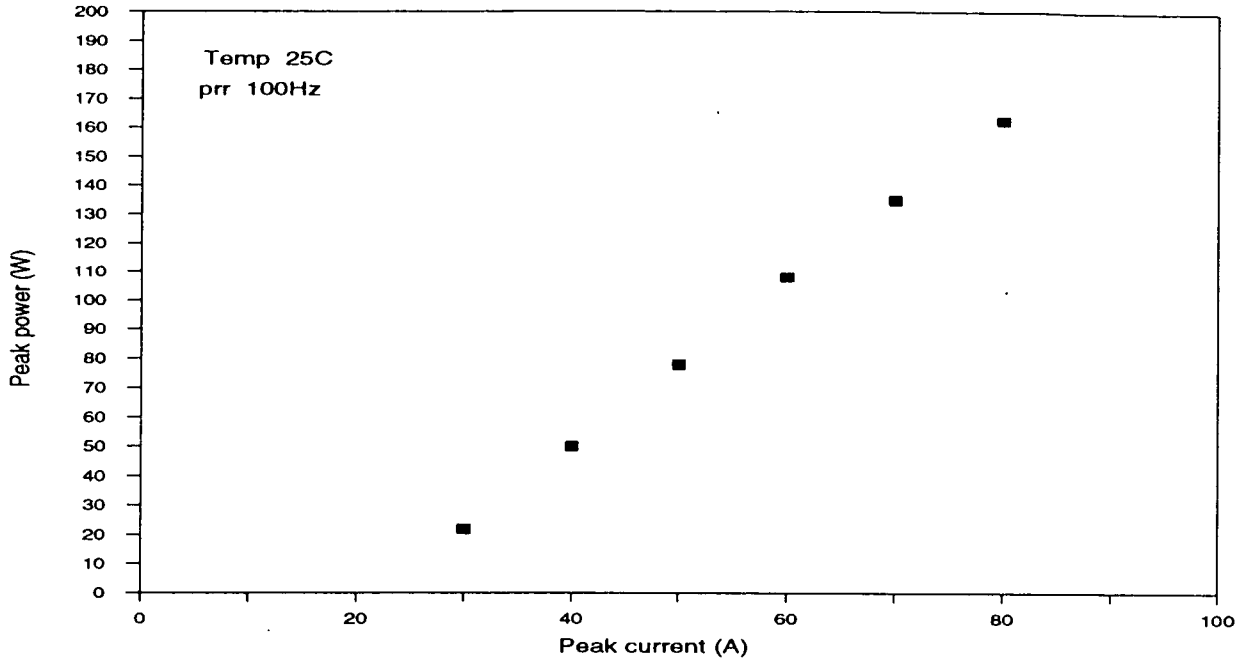

Figure 2.1.1 Output power data for a SDL three-bar diode-laser array.

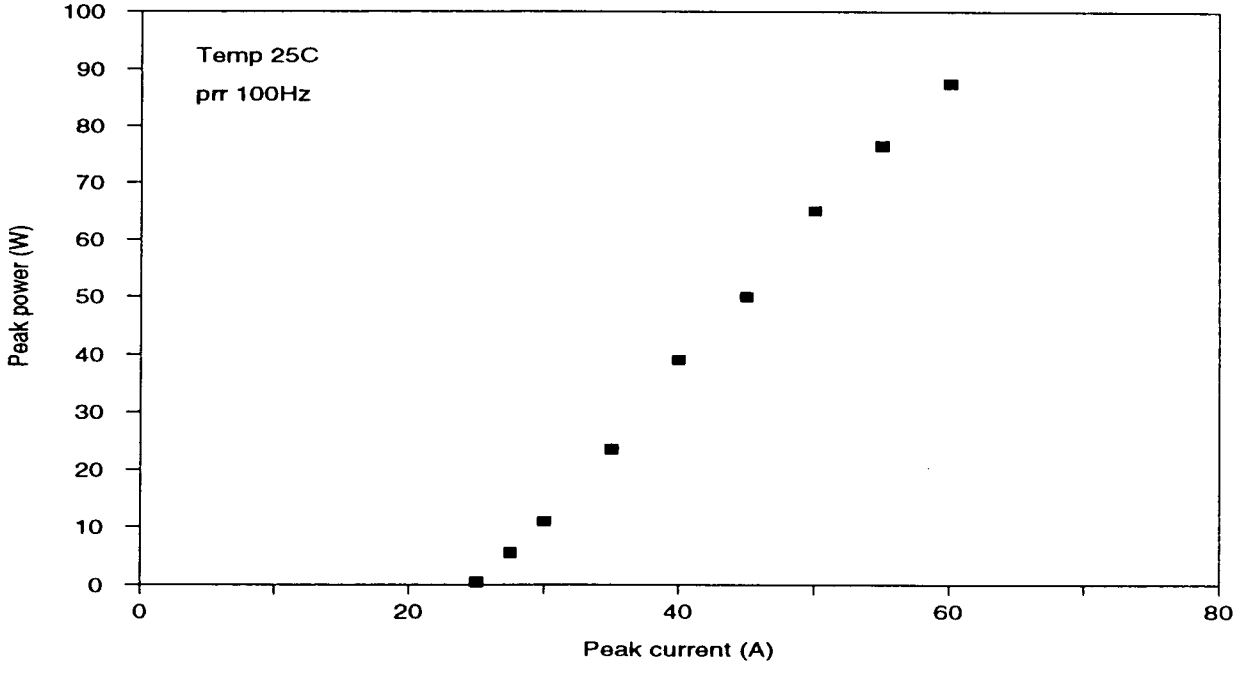

Figure 2.1.2 Output power data for a LDI three-bar diode-laser array.

Spatially resolved spectra.

We recorded the time-averaged spectra of both devices with spatial resolution at both the bar-level and the individual emitter-level. The spatial resolution was obtained by imaging the three-bar diode-laser array on the entrance slit of the grating spectrometer with a 55-mm focal length camera lens. To obtain the spectral emission of a single-bar, the devices were oriented with their bar-images parallel to the spectrometer entrance slit and only one bar overlapping the slit at any time. To obtain single emitter-level spectra the bar images were orthogonal to the spectrometer entrance slit and the slit width of 30 μm sampled a section of the bar approximately 4 μm long when imaged at x8 magnification. In this mode of operation the vertical height of the entrance slit was apertured to admit light from only one bar at a time.

Prior to taking spectral data we defined a labelling format for the spatial locations in the three-bar stack (see figure 2.1.3). The bar closest to the heatsink is the lower bar, the bar farthest from the heatsink is the upper bar, and the one in between these two is the center bar. We also chose to measure spectra from the center and ends of each bar and labelled these locations 1 through 9. The end of each bar may not be representative of typical thermal conditions in the outer 25% of each bar so our actual sample points were 1 mm inside the end of each 1-cm-long bar.

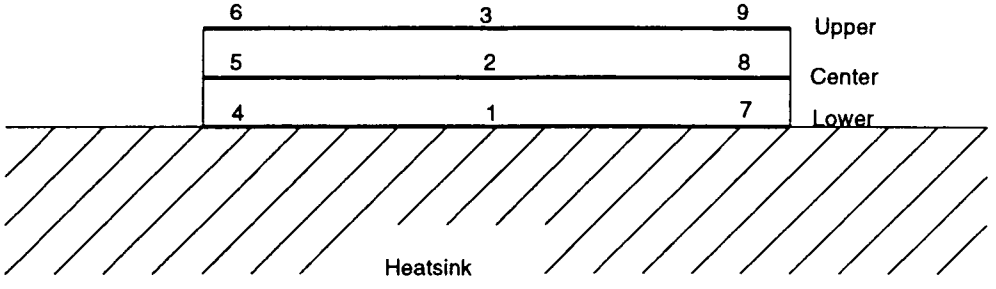

Note: View looking at the diode laser array.

Figure 2.1.3 Spatial sample points for spectral measurements.

All the spectral data taken is summarized in Tables 2.1.1 and 2.1.2 at the end of this section. Some spectral scans are discussed below. In general, if we assume the three bars of material are from the same region of an epitxially grown wafer, the spectra will be primarily influenced by the thermal properties of the position in the stack assembly. When the laser is pulsed "on", two mechanisms come into play to determine the wavelength. Initially, during the first tens of nanoseconds, the laser spectrum narrows as mode selection takes place in the

transition from spontaneous to stimulated emission and the wavelength may be influenced by changes in carrier density in the active region. Then, during the next few to tens of microseconds (depending on the thermal transient response of the structure), the whole assembly will heat up and reach a thermal equilibrium. This heating causes the laser to temperature tune. Each bar will experience a different thermal transient and the individual emitters on each bar will have different wavelength chirped spectra.

The steady-state tuning characteristics of the laser array are required for us to determine the heatsink temperature required to optically pump the Nd:YAG absorption at 808 nm. Figures 2.1.4 and 2.1.5 show temperature tuning data for the SDL and LDI devices, respectively. All the data was for emitters in spatial position #1 at the maximum device drive current.

Figures 2.1.6 and 2.1.8 show spectra for all three bars in each laser array, that indicate increasing bar temperatures as a function of distance from the heatsink. It is interesting to note that there is much less difference in temperature between the upper and center bars than the center and lower bar. The sum of the three bars is the spectral average and the data shown as x's is the center bar spectrum renormalized to the same peak height. This comparison of a single bar with the sum shows that the spectral was broadened by approximately 15% and 44% for the SDL and LDI devices, respectively.

Figures 2.1.7 and 2.1.9 show emission from the best and worst heatsunk regions of the each laser array and we see greater wavelength chirp from the emitter farthest from the heatsink. In an ideal device all emitters would be well heatsunk and have closely matched peak wavelengths and exhibit negligible wavelength chirp. One technology which claims to provide such uniformity of heatsinking is the Si-microchannel cooler [1]. However, at the time this work was done this technology was not available.

Unlike the SDL diode-laser array, the spectral profiles and widths for the LDI diode-laser array vary dramatically for the three bars and are all spectrally wider than those of SDL device. The laser structure used by LDI consists of an array of large optical cavity emitters which may be exhibiting spatial and spectral filamentation as a result of temperature and/or current density variations across the emitter width.

Tables 2.1.1 and 2.1.2 list the operating conditions, peak wavelength, spectral widths and a spectral skew parameter for each spectral scan. The skew parameter was defined to quantify the spectral assymetry in a time-averaged spectrum resulting from wavelength chirp and is given by:

Skew = (spectral FWHM with chirp)/(spectral FWHM without chirp)

Figure 2.1.10 illustrates the definition of the skew parameter. The solid line is the measured spectrum with wavelength chirp and the dashed line shows the lineshape without chirp. When there is no chirp the skew parameter is unity and for finite chirp the skew parameter is approximately equal to the ratio of total pulse energy to that which is within the spectral bandwidth of an unchirped device.

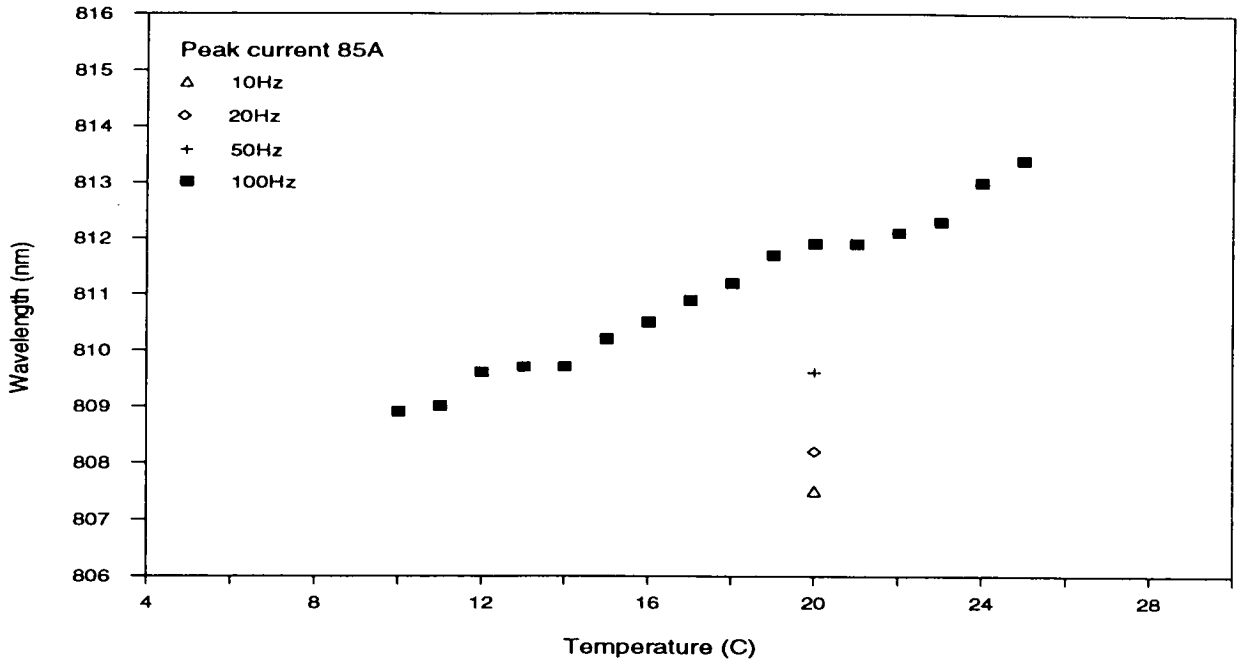

Figure 2.1.4 Tuning characteristics of a SDL three-bar diode-laser array.

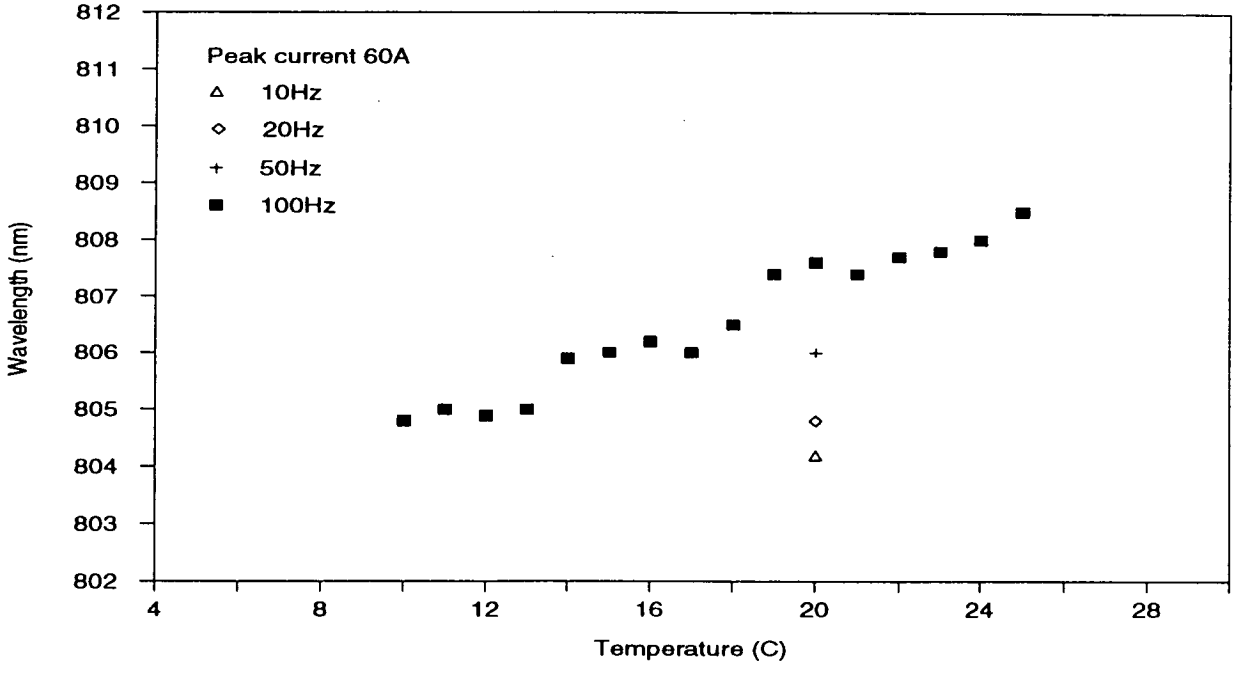

Figure 2.1.5 Tuning characteristics of a LDI three-bar diode-laser array.

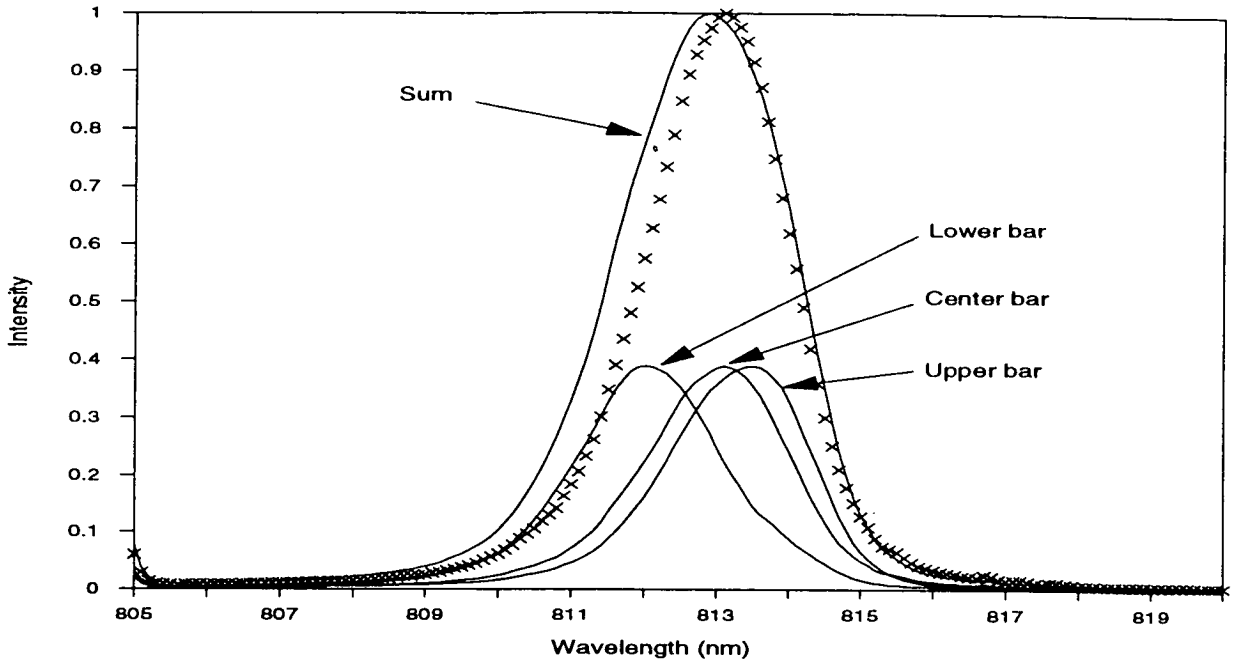

Figure 2.1.6 Spatially resolved time-averaged spectra of a SDL three-bar diode-laser array operating at 100Hz p.r.r.

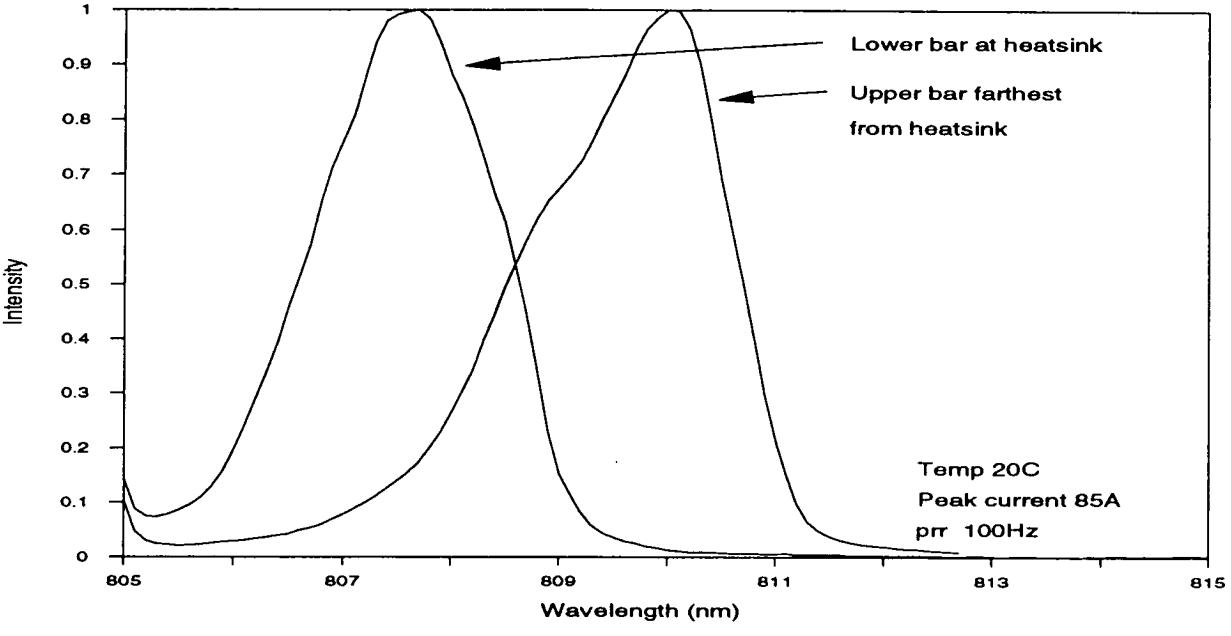

Figure 2.1.7 Spatially resolved time-averaged spectra of a SDL three-bar diode-laser array as a function of emitter position.

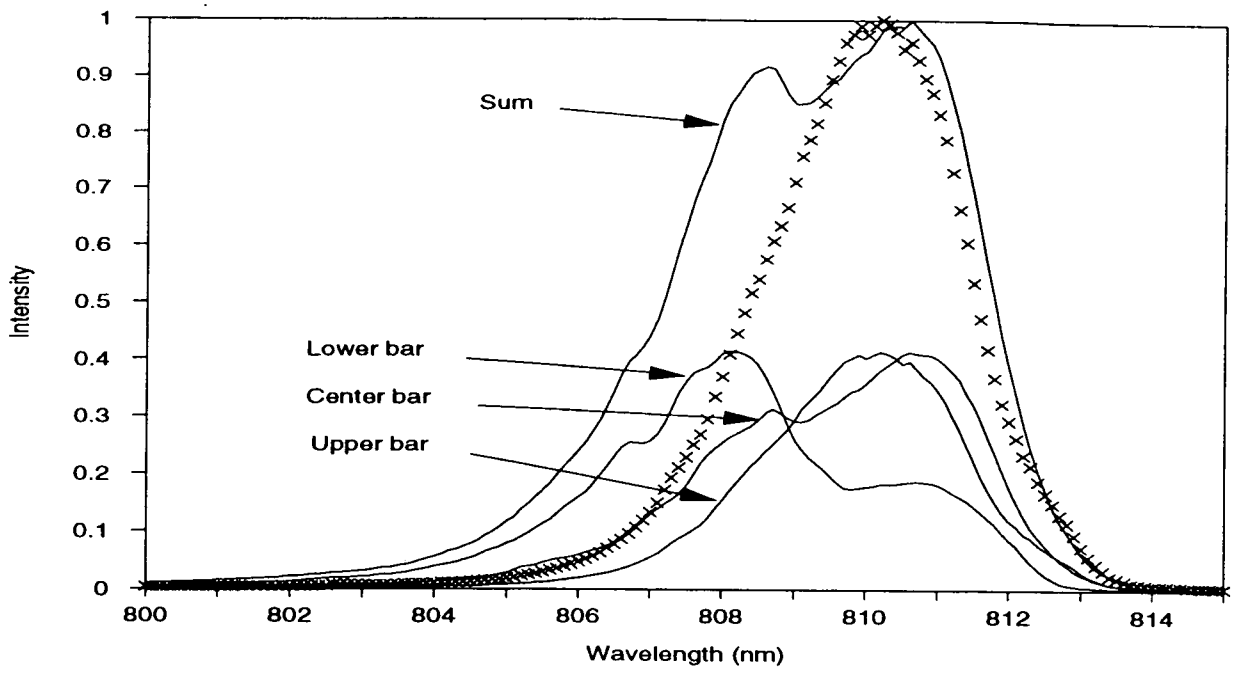

Figure 2.1.8 Spatially resolved time-averaged spectra of a LDI three-bar diode-laser array.

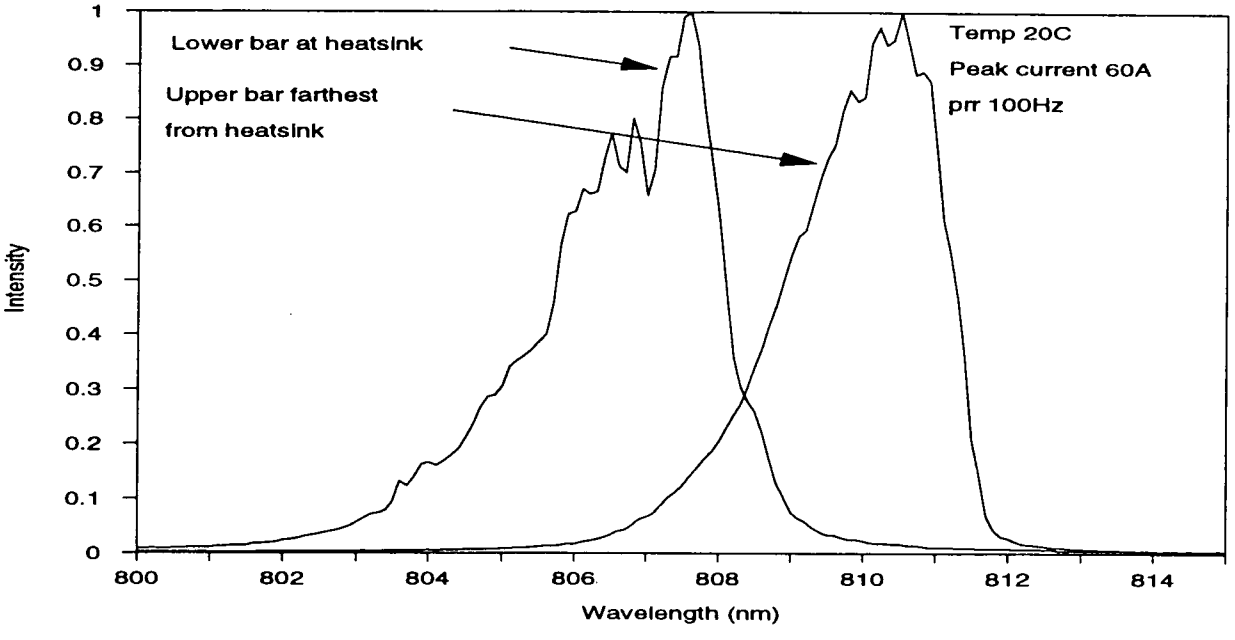

Figure 2.1.9 Spatially resolved time-averaged spectra of a LDI three-bar diode-laser array as a function of emitter position.

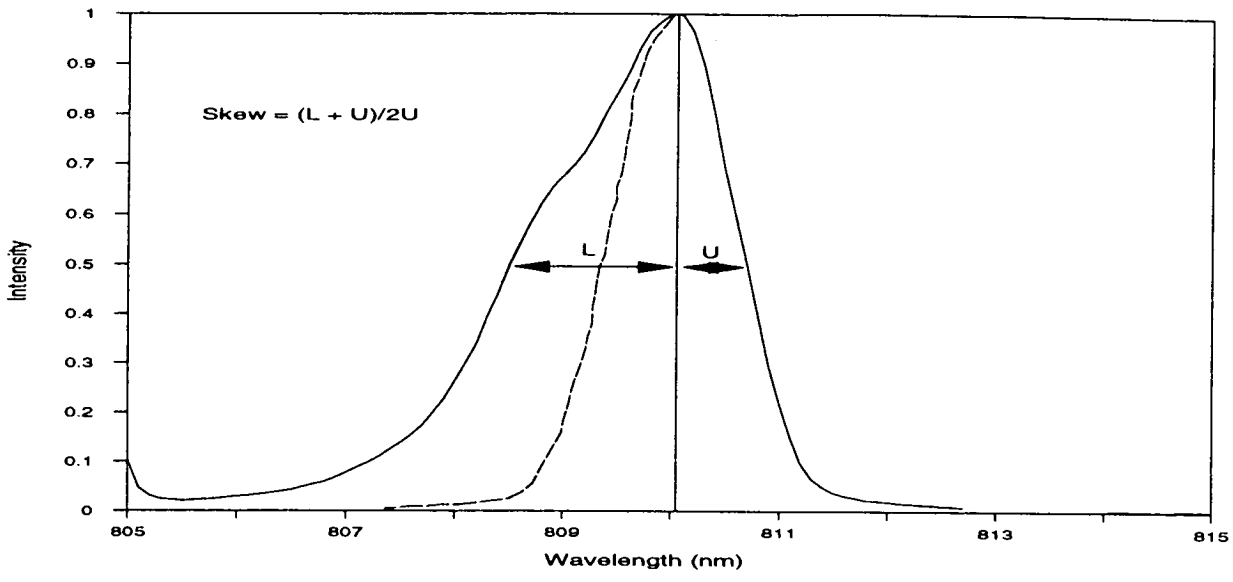

Figure 2.1.10 Schematic representation of the skew parameter.

Some parameters listed in Table 2.1.2 are negative due limitations of our data analysis program in dealing with the multiple spectral peaks characteristic of the LDI diode-laser array. These parameters should be ignored.

Time resolved spectra.

Time resolved spectra of each individual bar were taken for both the SDL and LDI diode-laser arrays using the same imaging arrangement and grating spectrometer described earlier. The time resolution was obtained by using a gated integrator (commonly called a boxcar averager) detection system to sample a 1-μs wide window at a fixed delay during the laser pulse while the spectrometer scanned the wavelength. Several such time resolved spectral scans were then combined graphically to obtain the three dimensional spectral evolutions shown in figures 2.1.11 through 2.1.13 and 2.1.15 through 2.1.17. The same data sets were also used to generate the peak wavelength chirp plots shown in figures 2.1.14 and 2.1.18.

All the spectral evolutions exhibit qualitatively similar wavelength chirp and spectral narrowing with time. Yet, the peak intensity characteristics are radically different for the two devices. The LDI laser array turns on smoothly with negligible overshoot and follows the rectangular profile of the drive current pulse. In contrast, the SDL laser array exhibits up to 50% overshoot and 50% ringing with approximately 100 μs period.

Table 2.1.1 Summary of time-averaged spectral data of a SDL three-bar diode-laser array.

PRR(Hz)	T(C)	I(A)	Position	Peak(nm)	FWHM(nm)	Skew
100.00	25.00	85.00	1.00	813.40	2.00	1.54
100.00	24.00	85.00	1.00	813.00	2.10	1.75
100.00	23.00	85.00	1.00	812.30	2.00	2.86
100.00	22.00	85.00	1.00	812.10	1.80	2.57
100.00	21.00	85.00	1.00	811.90	1.60	2.29
100.00	20.00	85.00	1.00	811.90	1.70	1.55
100.00	19.00	85.00	1.00	811.70	1.70	1.42
100.00	18.00	85.00	1.00	811.20	1.90	1.90
100.00	17.00	85.00	1.00	810.90	2.10	1.91
100.00	16.00	85.00	1.00	810.50	1.90	2.11
100.00	15.00	85.00	1.00	810.20	1.60	2.29
100.00	14.00	85.00	1.00	809.70	1.60	3.20
100.00	13.00	85.00	1.00	809.70	1.70	2.12
100.00	12.00	85.00	1.00	809.60	1.60	1.78
100.00	11.00	85.00	1.00	809.00	1.70	2.83
100.00	10.00	85.00	1.00	808.90	1.60	2.29
50.00	20.00	85.00	1.00	809.60	1.90	1.58
20.00	20.00	85.00	1.00	808.20	1.60	1.60
10.00	20.00	85.00	1.00	807.50	2.10	2.10
10.00	20.00	85.00	1.00	807.70	2.00	1.82
10.00	20.00	85.00	2.00	809.00	2.10	1.40
10.00	20.00	85.00	3.00	808.40	1.80	2.25
10.00	20.00	85.00	4.00	807.10	2.00	1.67
10.00	20.00	85.00	5.00	807.60	1.50	1.50
10.00	20.00	85.00	6.00	808.40	1.70	1.89
10.00	20.00	85.00	7.00	808.70	2.60	1.86
10.00	20.00	85.00	8.00	808.80	2.00	1.67
10.00	20.00	85.00	9.00	810.00	2.10	1.50
100.00	20.00	85.00	1.00	811.80	1.80	2.00
100.00	20.00	85.00	2.00	813.30	2.00	1.54
100.00	20.00	85.00	3.00	813.30	1.90	1.73
100.00	20.00	85.00	4.00	810.50	2.00	2.22
100.00	20.00	85.00	5.00	811.20	2.00	2.00
100.00	20.00	85.00	6.00	812.60	1.70	1.70
100.00	20.00	85.00	7.00	813.00	2.60	1.62
100.00	20.00	85.00	8.00	812.90	2.30	1.64
100.00	20.00	85.00	9.00	814.30	2.20	1.83
100.00	20.00	85.00	lower	812.00	2.20	2.20
100.00	20.00	85.00	center	813.10	2.20	1.83
100.00	20.00	85.00	upper	813.50	2.20	1.69
10.00	20.00	85.00	lower	807.60	2.20	1.83
10.00	20.00	85.00	center	808.80	2.30	1.77
10.00	20.00	85.00	upper	809.00	2.10	1.75

Table 2.1.2 Summary of time-averaged spectral data of a LDI three-bar diode-laser array.

PRR(Hz)	T(C)	I(A)	Position	Peak(nm)	FWHM(nm)	Skew
100.00	25.00	85.00	1.00	808.50	1.80	1.50
100.00	24.00	85.00	1.00	808.00	1.80	2.00
100.00	23.00	85.00	1.00	807.80	1.70	2.12
100.00	22.00	85.00	1.00	807.70	1.70	1.55
100.00	21.00	85.00	1.00	807.40	-0.20	-0.17
100.00	20.00	85.00	1.00	807.60	2.20	1.22
100.00	19.00	85.00	1.00	807.40	0.00	0.00
100.00	18.00	85.00	1.00	806.50	2.90	1.71
100.00	17.00	85.00	1.00	806.00	2.70	1.93
100.00	16.00	85.00	1.00	806.20	2.40	1.41
100.00	15.00	85.00	1.00	806.00	2.70	1.35
100.00	14.00	85.00	1.00	805.90	2.70	1.23
100.00	13.00	85.00	1.00	805.00	2.60	1.86
100.00	12.00	85.00	1.00	804.90	-0.10	0.11
100.00	11.00	85.00	1.00	805.00	2.20	1.22
100.00	10.00	85.00	1.00	804.80	2.20	1.29
50.00	20.00	85.00	1.00	806.00	2.50	1.67
20.00	20.00	85.00	1.00	804.80	3.40	2.43
10.00	20.00	85.00	1.00	804.20	4.10	2.93
10.00	20.00	85.00	1.00	804.20	4.10	2.93
10.00	20.00	85.00	2.00	804.90	2.80	2.80
10.00	20.00	85.00	3.00	806.70	4.30	2.69
10.00	20.00	85.00	4.00	808.80	3.40	2.83
10.00	20.00	85.00	5.00	805.70	0.20	0.09
10.00	20.00	85.00	6.00	809.50	3.50	1.84
10.00	20.00	85.00	7.00	805.60	3.50	2.33
10.00	20.00	85.00	8.00	809.40	3.40	2.00
10.00	20.00	85.00	9.00	806.80	4.00	2.22
100.00	20.00	85.00	1.00	807.60	2.20	1.22
100.00	20.00	85.00	2.00	808.00	0.90	2.25
100.00	20.00	85.00	3.00	809.40	2.60	2.17
100.00	20.00	85.00	4.00	813.10	2.30	1.44
100.00	20.00	85.00	5.00	811.10	2.30	1.44
100.00	20.00	85.00	6.00	812.30	2.30	1.92
100.00	20.00	85.00	7.00	808.50	1.40	1.27
100.00	20.00	85.00	8.00	812.30	2.10	1.40
100.00	20.00	85.00	9.00	810.50	2.30	1.44
100.00	20.00	85.00	lower	808.10	3.00	1.76
100.00	20.00	85.00	center	810.60	4.20	1.45
100.00	20.00	85.00	upper	810.20	3.10	1.72

The same ringing is also present in the wavelength chirp data (see figure 2.1.14) and is less pronounced for the upper and center bars, which are not as well heatsunk as the lower bar. This implies a thermal origin or contribution to the ringing mechanism that may be an artifact of the temperature control system.

The wavelength chirp data indicates thermal equilibration times are approximately 100 μs and 130 μs for the SDL and LDI laser arrays, respectively. In addition, the magnitude of the wavelength chirp is almost the same (2.7 nm) for all three bars in the SDL device, an indication of good heatsinking. The LDI device shows a sizeable increase in chirp for the center and upper bars (3.3 nm) compared to the lower bar (2.2 nm), an indication of poor heatsinking.

The impact of the spectral evolution of the diode-laser arrays on the performance of the Nd:YAG laser cannot be readily predicted. However, the data clearly show higher spectral brightness for the SDL devices. These were chosen for the remainder of the Phase II effort.

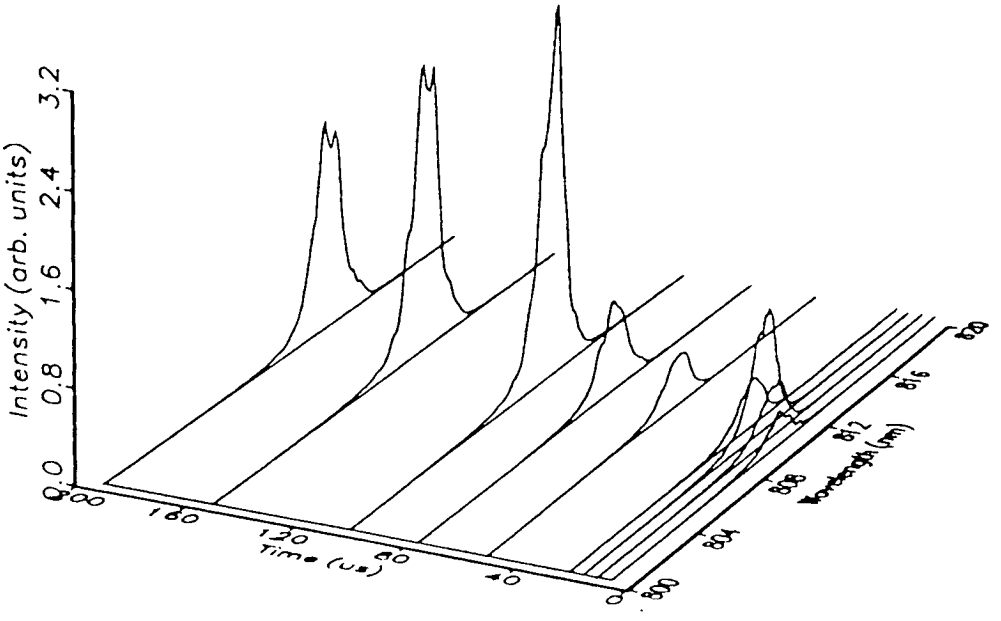

Figure 2.1.11 Time-resolved spectrum of the lower bar of the SDL diode-laser array.

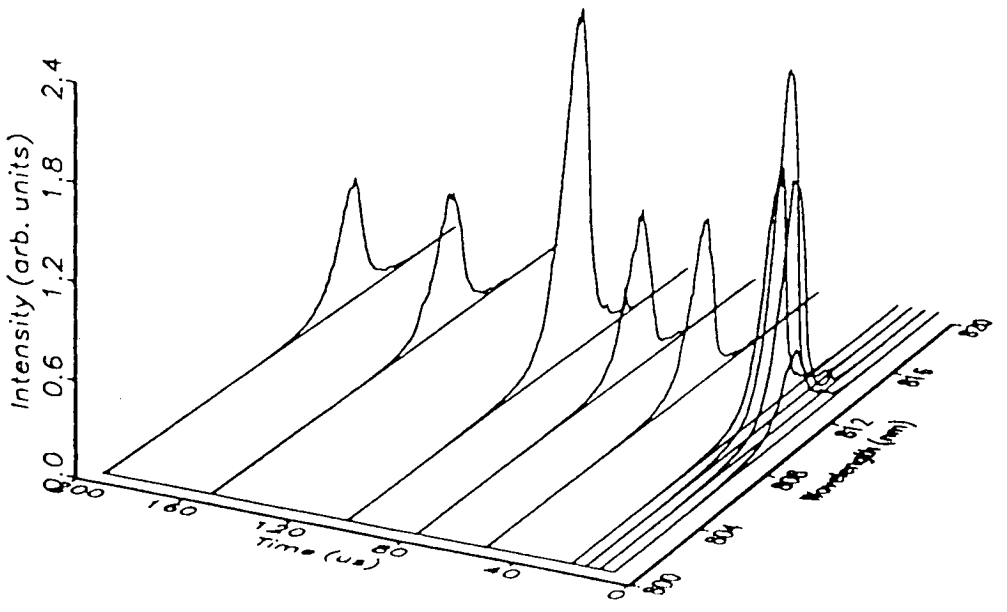

Figure 2.1.12 Time-resolved spectrum of the center bar of the SDL diode-laser array.

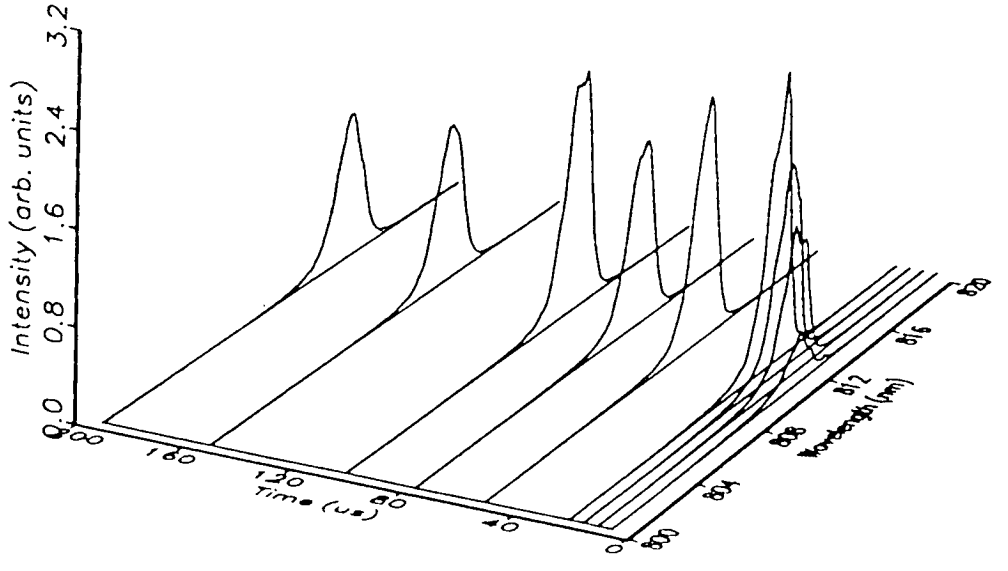

Figure 2.1.13 Time-resolved spectrum of the upper bar of the SDL diode-laser array.

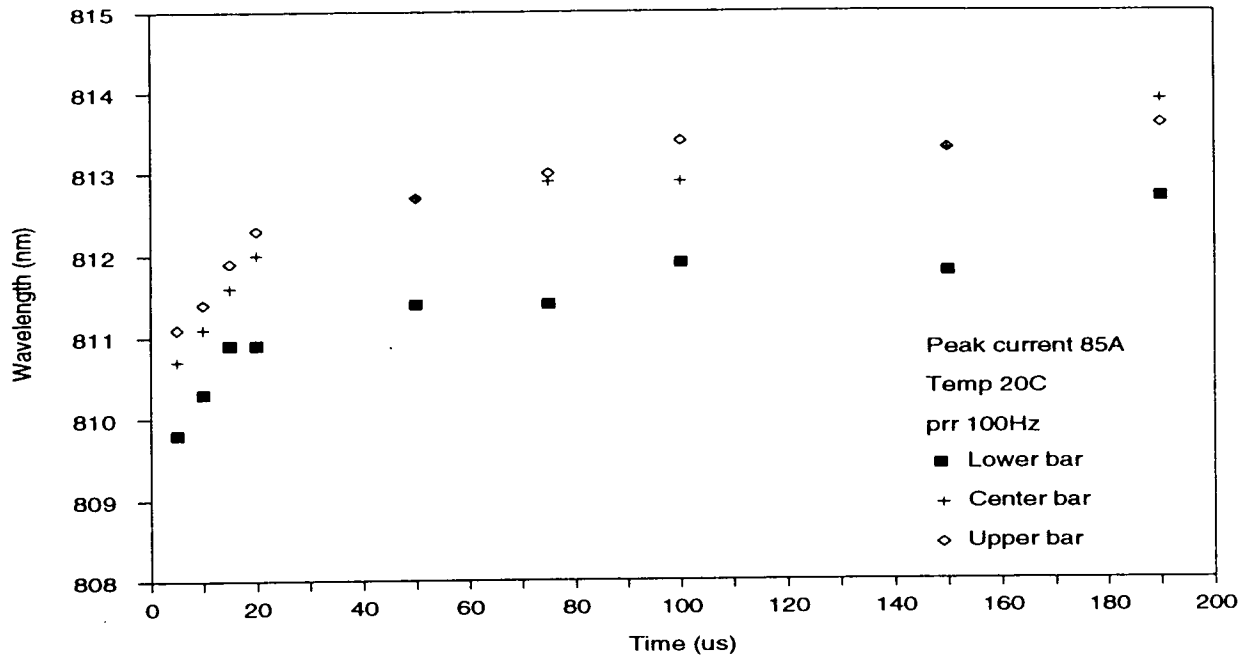

Figure 2.1.14 Wavelength chirp characteristics of the SDL diode-laser array.

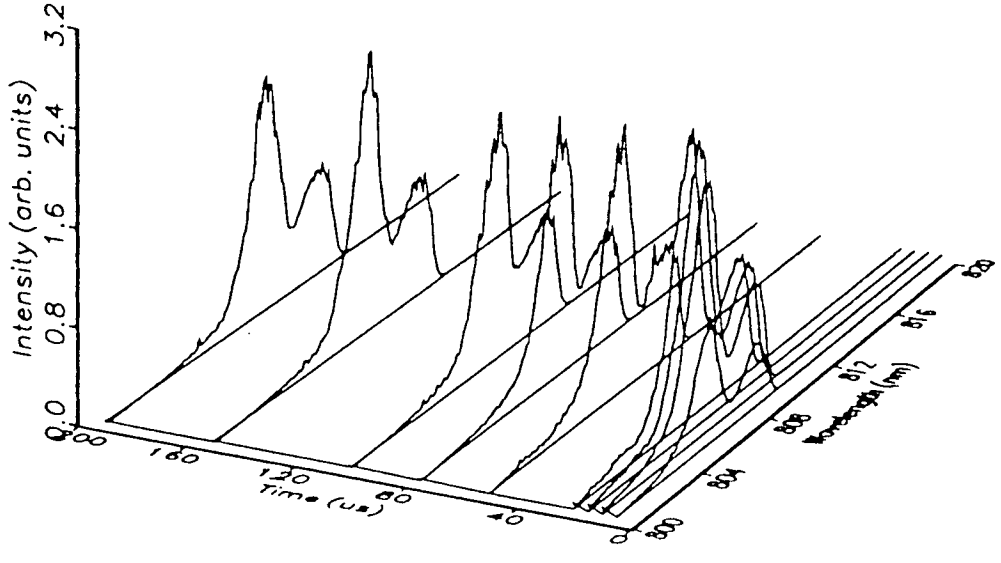

Figure 2.1.15 Time-resolved spectrum of the lower bar of the LDI diode-laser array.

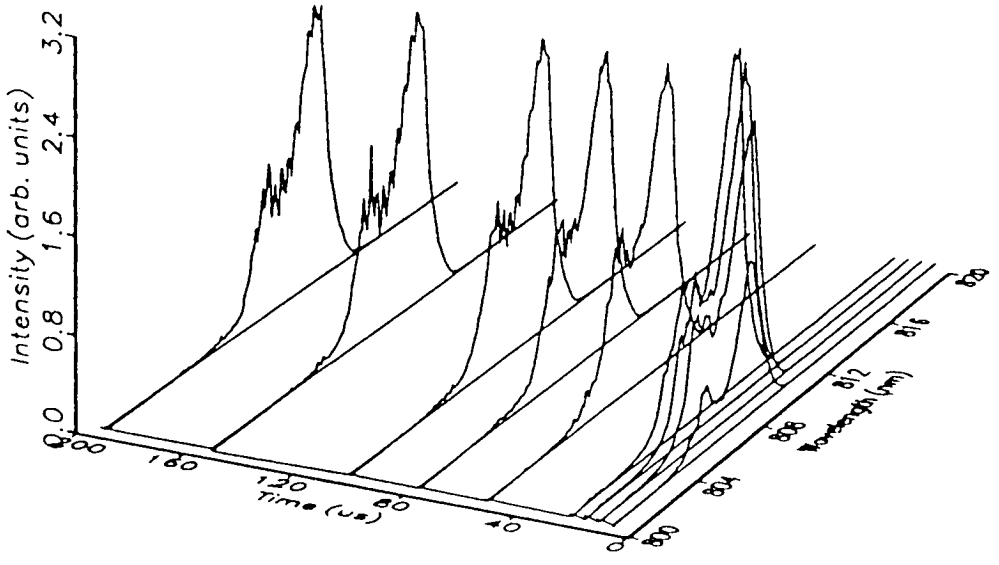

Figure 2.1.16 Time-resolved spectrum of the center bar of the LDI diode-laser array.

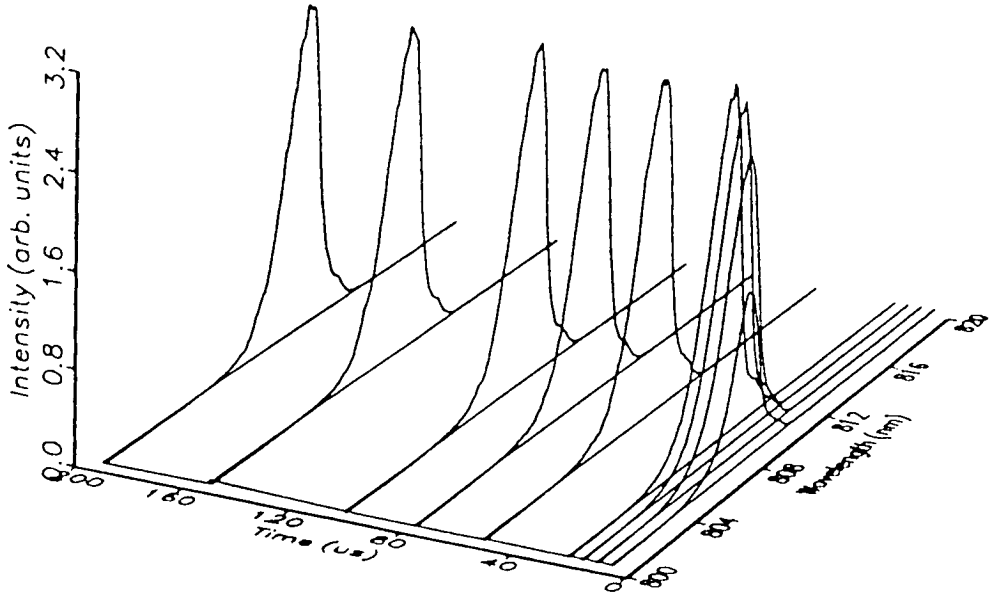

Figure 2.1.17 Time-resolved spectrum of the upper bar of the LDI diode-laser array.

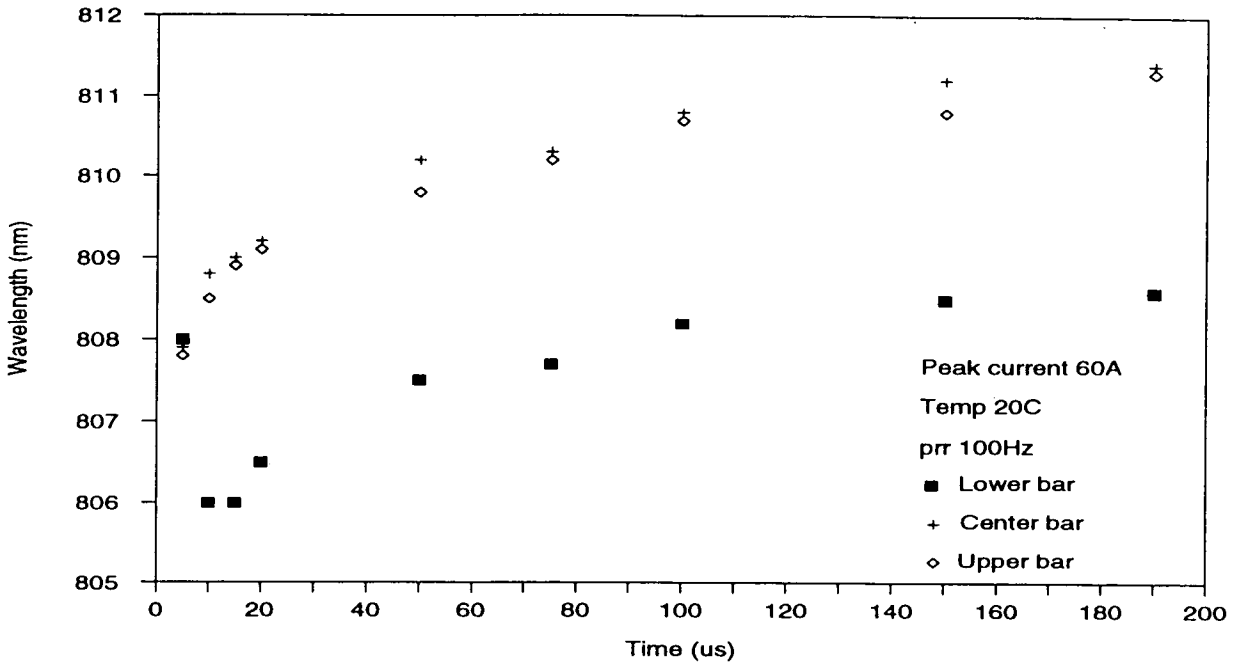

Figure 2.1.18 Wavelength chirp characteristics of the LDI diode-laser array.

2.2 *Pumped Laser Rod Characterization.*

Fluorecence profiles.

The deposited energy profiles in both orientations of our Brewster-angled, D-shaped laser rods were determined by imaging the fluorescence from the center of the laser array pumped rod onto a CCD detector array interfaced to a frame grabber and computer (Montana Laser Corp, Multicam beam profile analysis system). The fluorescence image intensity is directly proportional to the excited state density of Nd-ions in the laser rod.

Relative to the D-shaped laser rod cross section, two Brewster-angled face orientations have been defined. Horizontal orientation is when the electric field is perpendicular to the rear surface of the laser rod (i.e. the long face opposite the curved barrel). Vertical orientation is when the electric field is parallel to the rear surface of the laser rod.

The data shown in figures. 2.2.1 through 2.2.6 are corrected for the Brewster rod orientation because the observation point is beyond the Brewster faces. These fluorescence profiles correspond to the excited state density profiles in the resonator, outside the laser rod. Each rod orientation (horizontal and vertical Brewster faces) was optically pumped with the SDL

three-bar diode-laser array spaced 0.5 mm, 1 mm, and 1.5 mm from the nearest point on the curved surface of the D-shaped laser rods. The 1.5-mm spacing corresponded to our original design.

The data shows that the vertical orientation of the Brewster faces produces a more circular beam profile than the horizontal orientation. The excited state density in the horizontal direction of both rod orientations is almost uniform from the flat rear surface to the front curved surface of the D-shape. The beam profile in the vertical direction is almost Gaussian in shape and therefore ideally matched to a TEM_{00}-mode profile filling the laser rod. The circularization improved when we used the five-bar diode-laser array as shown in figure 2.2.7.

In addition, the fluorescence contour plots show motion of the peak excited state density towards the front (curved surface) of the rod and decreasing pump spot size for smaller rod-to-array spacing. The normal-mode laser performance was more efficient for smaller rod-to-array spacings as would be expected (see Section 2.3). This decentering of the deposited pump energy decenters the thermally induced lens and introduces a beam path deflection in the laser rod (see the following sub-section on thermal lensing)

Thermal-lensing.

We investigated the presence of thermally induced lensing in a five-bar diode-laser array-pumped laser rod. A He-Ne laser operating at 632.8 nm probed the laser rod after passing through a 54.7-cm plano-convex lens. The measurement technique was based on analyzing changes to the Gaussian beam waist as a result of the thermally induced lens in the pumped laser rod. The thermal lens focal length can be determined from equation (67) of [2]. We used a beam profile analyzer (Spiricon Model LBA-100) to determine the position and diameter of the initial beam waist from the center of the unpumped laser rod and the diameters of the beam waists obtained at different pump-laser energies.

Figure 2.2.8 shows the focal length of the thermally induced lens as a function of average pump power incident on the laser rod. The functional form was similar to the inverse-power dependence commonly seen in lamp-pumped, circular cross section rods in which a radial refractive index distribution (i.e. lens) is the result of a radial heat flow in the rod cooling system. Yet, the present system has a more complex heatflow pattern that is strongly influenced by both the nonuniform pump deposition and the asymmetric cooling geometry.

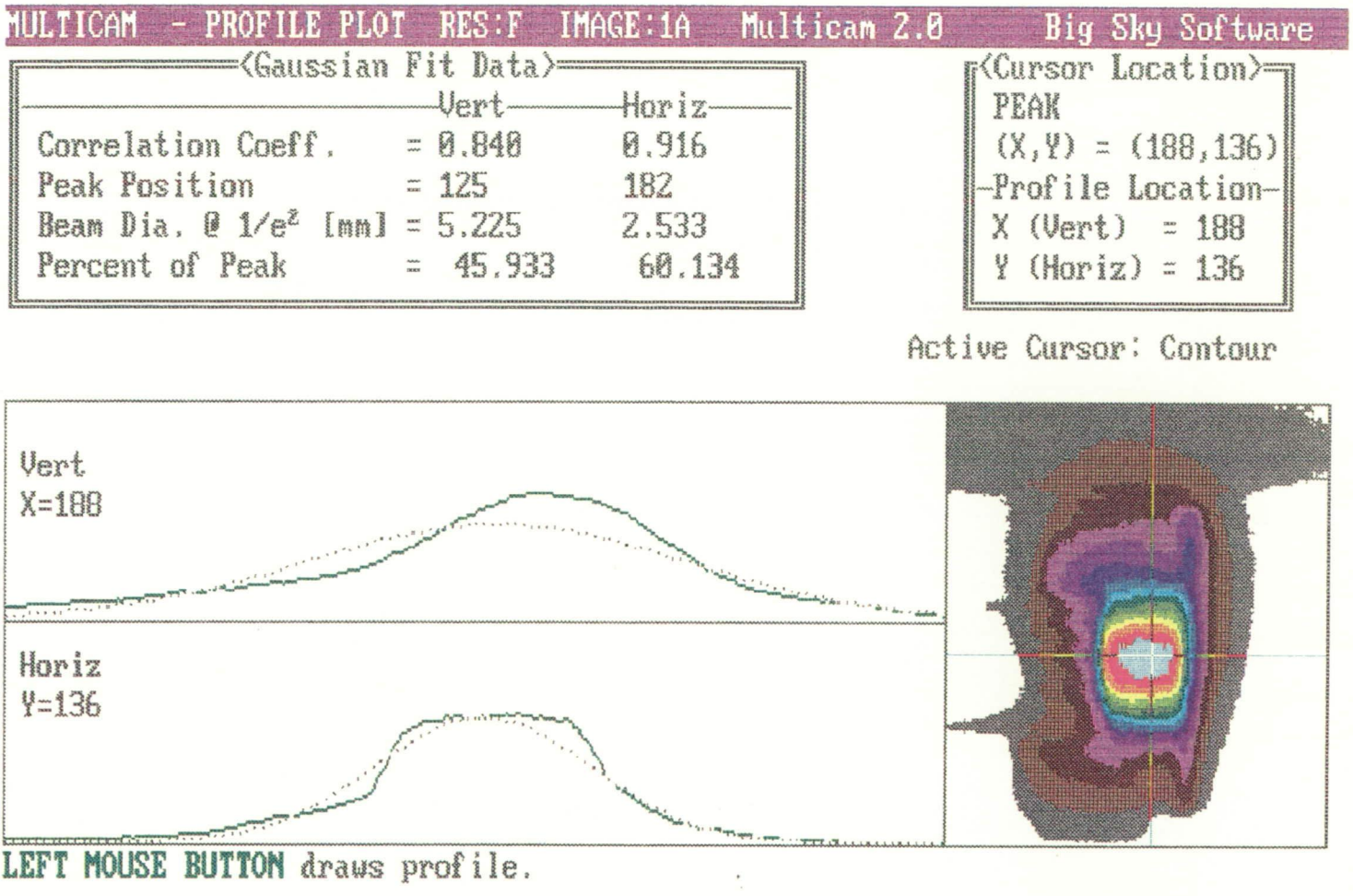

Figure 2.2.1 Fluorescence profile of the horizontal Brewster-angled, D-shaped laser rod with the three-bar diode-laser array 0.5 mm from the rod.

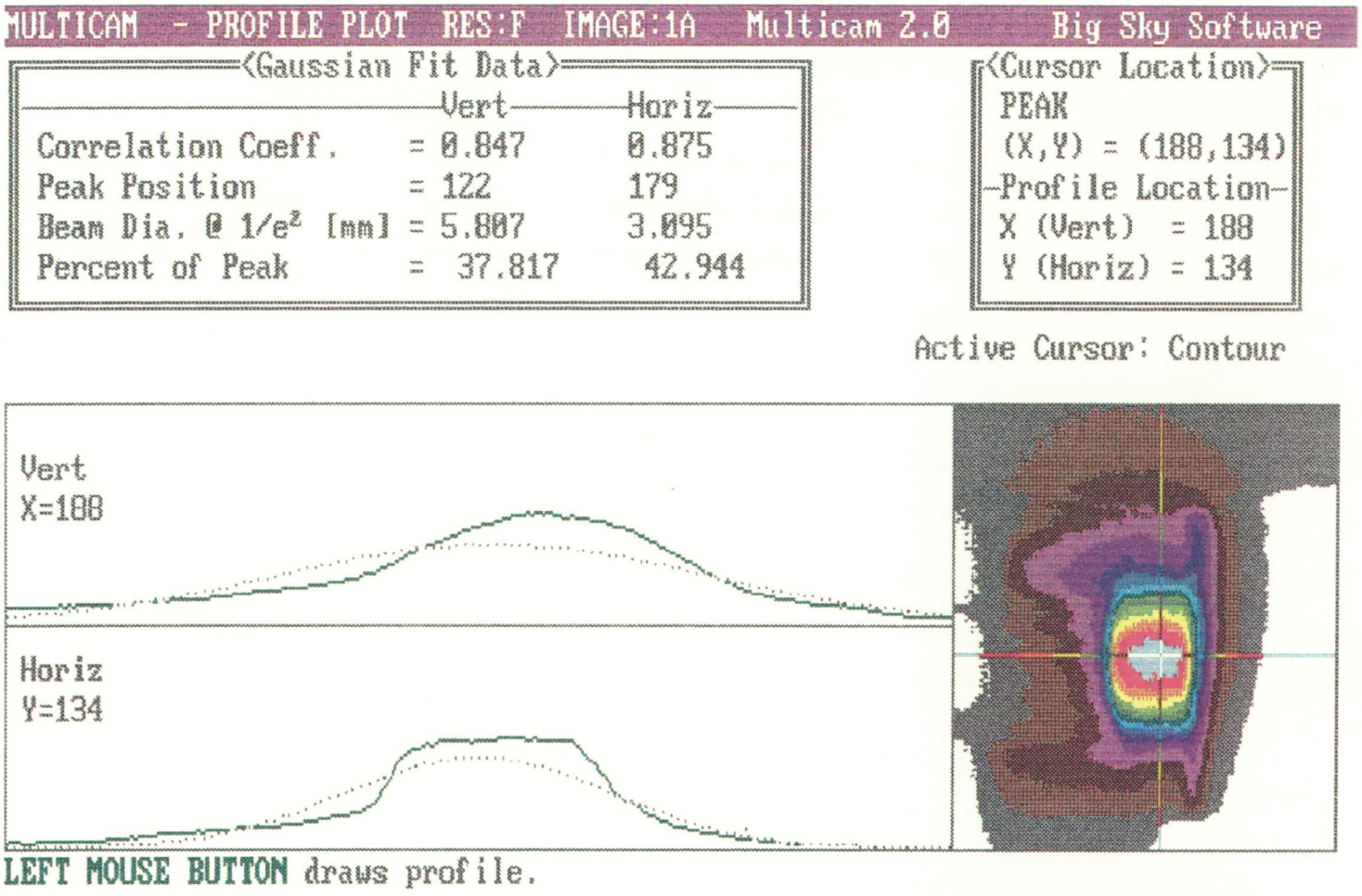

Figure 2.2.2 Fluorescence profile of the horizontal Brewster-angled, D-shaped laser rod with the three-bar diode-laser array 1 mm from the rod.

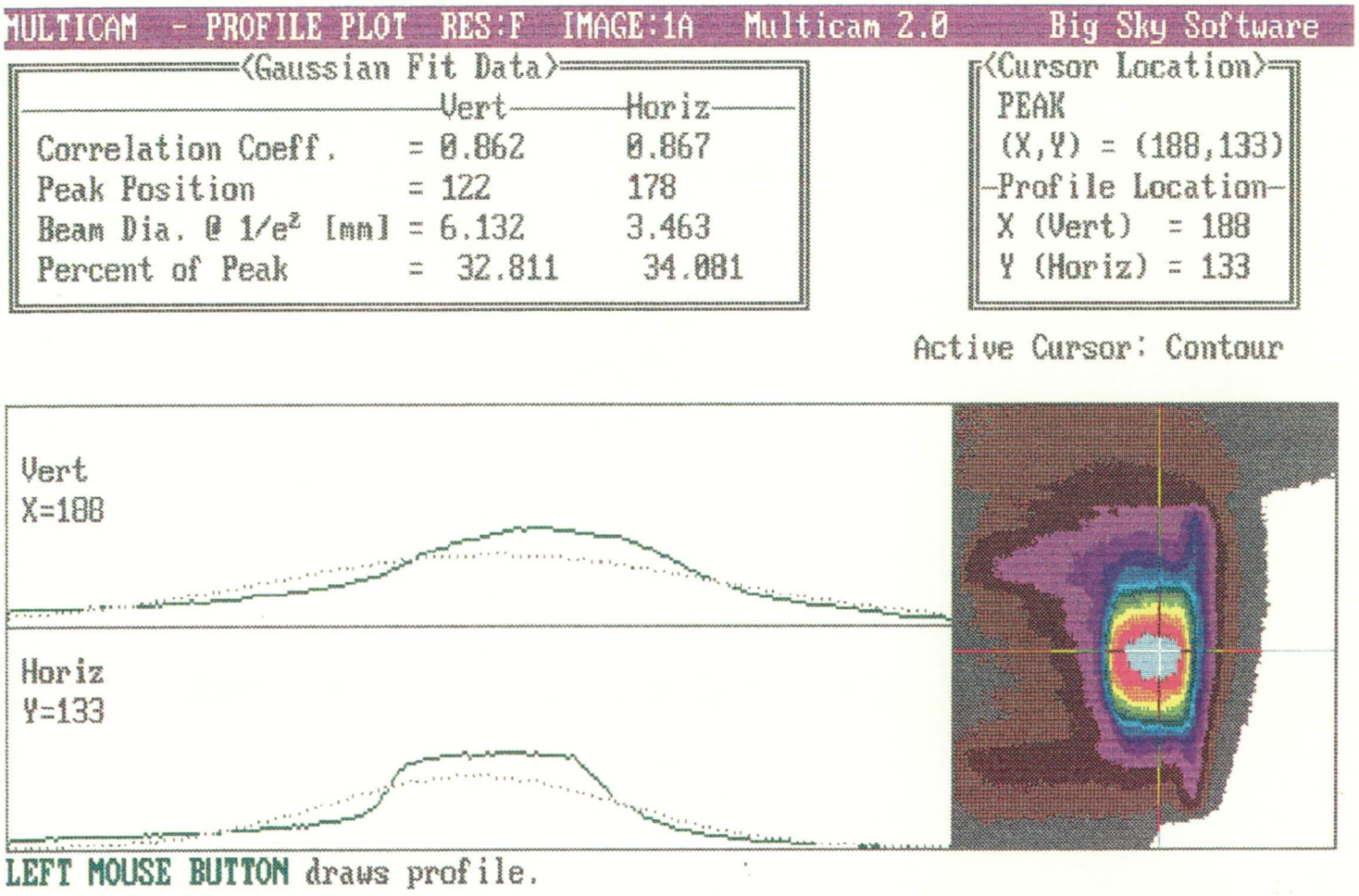

Figure 2.2.3 Fluorescence profile of the horizontal Brewster-angled, D-shaped laser rod with the three-bar diode-laser array 1.5 mm from the rod.

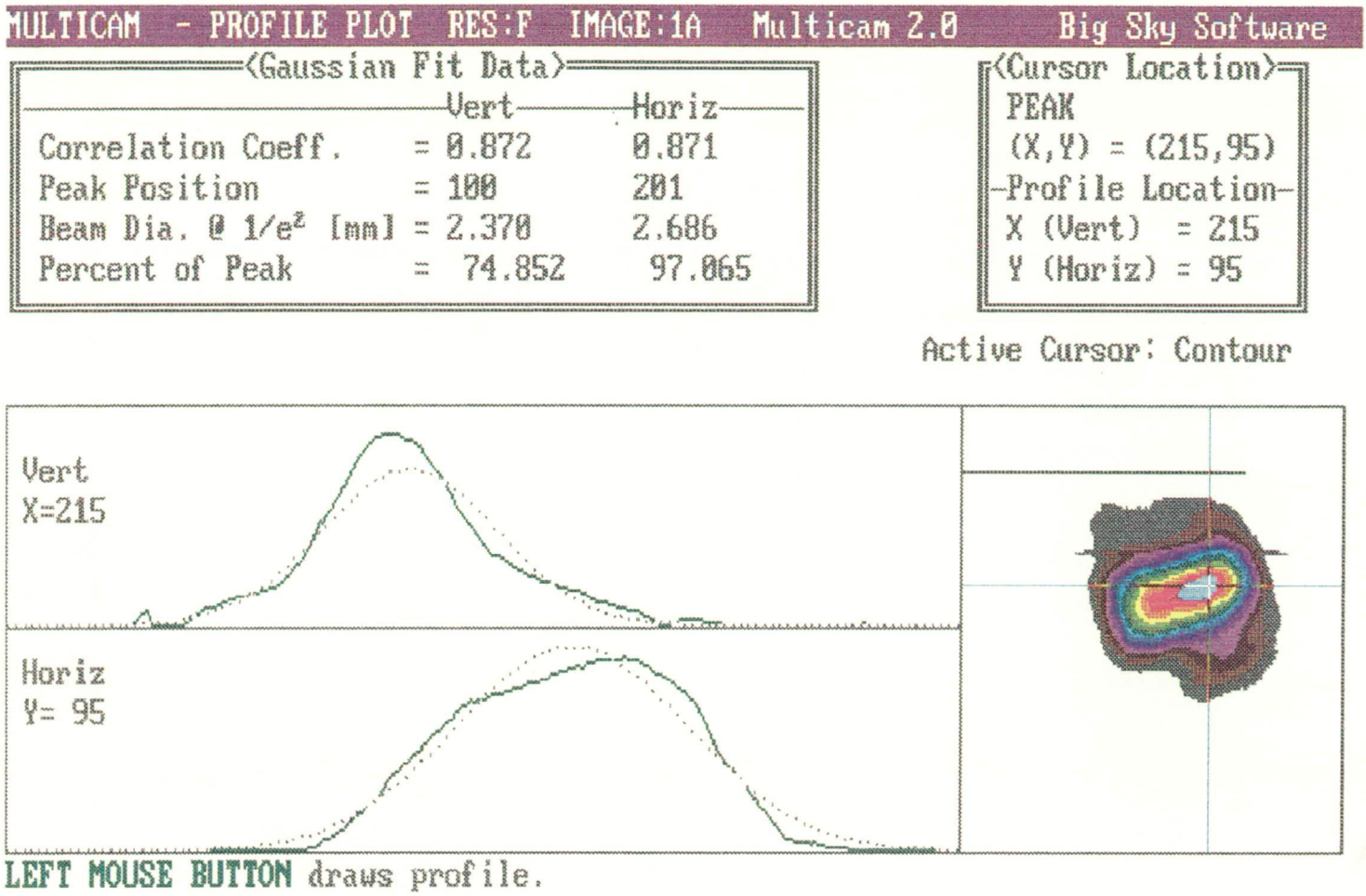

Figure 2.2.4 Fluorescence profile of the vertical Brewster-angled, D-shaped laser rod with the three-bar diode-laser array 0.5 mm from the rod.

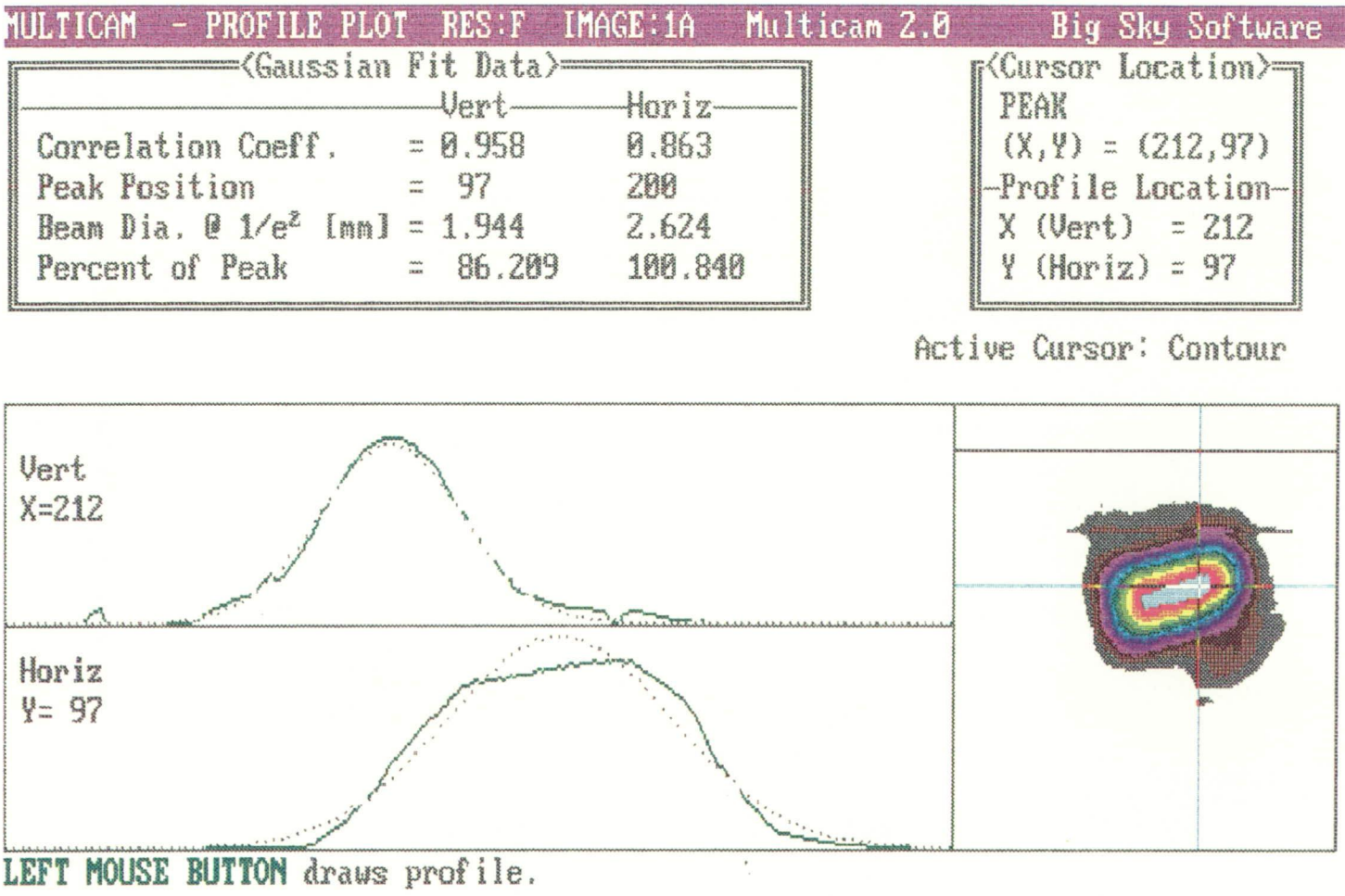

Figure 2.2.5 Fluorescence profile of the vertical Brewster-angled, D-shaped laser rod with the three-bar diode-laser array 1 mm from the rod.

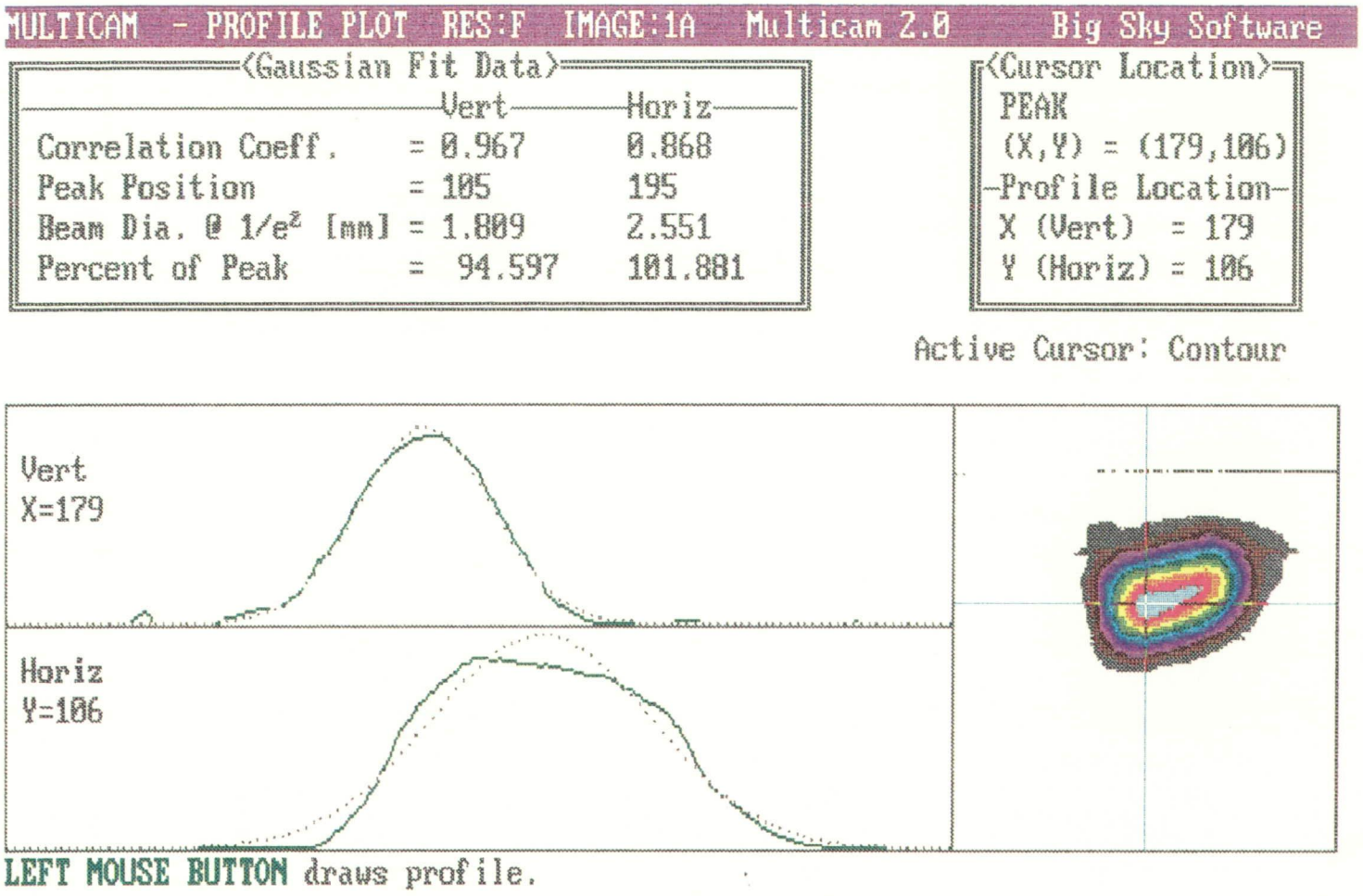

Figure 2.2.6 Fluorescence profile of the vertical Brewster-angled, D-shaped laser rod with the three-bar diode-laser array 1.5 mm from the rod.

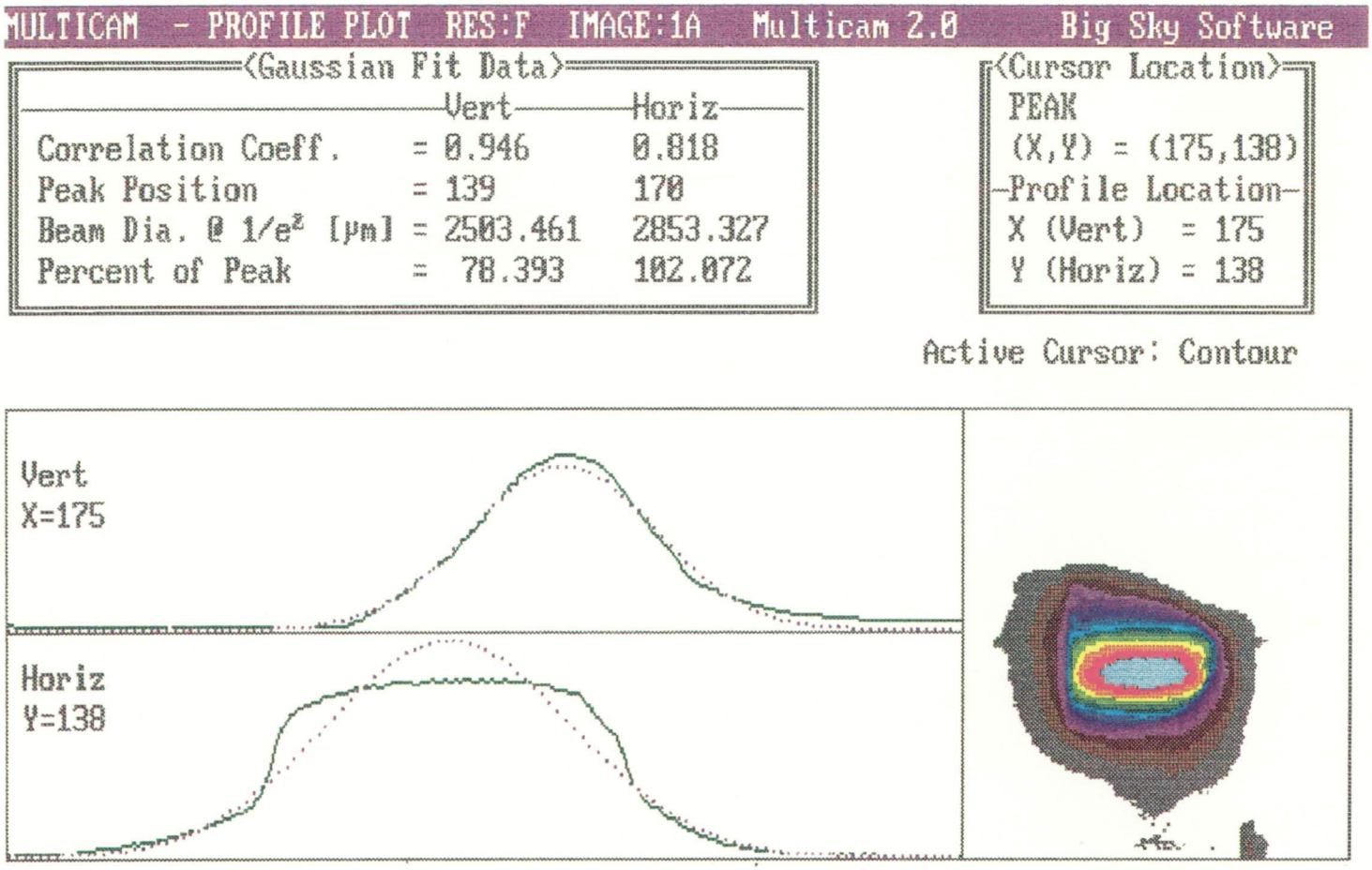

Figure 2.2.7 Fluorescence profile of the vertical Brewster-angled, D-shaped laser rod with the five-bar diode-laser array 0.5 mm from the rod.

In addition to the thermally induced lensing, significant angular deflection of the He-Ne laser probe beam was also observed. The magnitude of this beam deflection was as large as 0.3 mrad or approximately 0.1 mrad/W of incident pump power.

The thermal lens data represents the mean focal length, f, for the laser rod at each average pump power level, P, assuming ideal circular symmetry of the induced index profile. Even though the deposited energy profiles in the laser rod were not circularly symmetric the probe beam profiles showed no evidence of either strong asymmetry or the existence of separate beam waists (indicative of different lens focal lengths in the vertical and horizontal directions).

The work of Innocenzi et al. [3] treats thermal lensing in a laser rod with a Gaussian pump deposition profile and is similar to the more conventional radial diffusion analysis of uniformly pumped lamp-based systems [4], except that the rod area is replaced by the area of the pump deposition profile. This analysis [3] closely matches our pump geometry (but not our cooling geometry) and was used to generate the solid curve of figure 2.2.8 that is of the form $f = M/P$, where M is a constant equal to 1.96×10^3 W-cm. A least squares fit of the same functional form to the experimental data gave a value of 1.05×10^3 W-cm and is shown as the dashed line in figure 2.2.8.

The poor agreement of the analytical model [3] led us to numerically model the steady-state temperature distributions in the laser rod for different heat load distributions and boundary conditions. The modelling was performed using a finite-element software package (COSMOS/M, Structural Research and Analysis Corp.) designed for mechanical engineering and was therefore unable to directly predict the thermal lens parameters. However, we were able to interpret the temperature distributions obtained from the modelling with the aid of the analytical model.

Figures 2.2.9 and 2.2.10 show two temperature distributions for 20 °C isothermal boundary conditions and 0.6 W total heat loading. The first case, figure 2.2.9, has a uniform heat load distribution and is equivalent to conventional lamp pumped laser rods (except for the semicircular rod cross-section). The temperature distribution is almost elliptical in profile and could be optically described as a spherical lens with an additional cylindrical lens. This is in contrast to the circular symmetry obtained in lamp pumped rods. The second case, figure 2.2.10, has the near-Gaussian heat load distribution of the diode-laser pumped system. The heat load was derived from the fluorescence image data shown in figure 2.2.7. The near-Gaussian heat

load distribution generated a circularily symmetric temperature distribution with three times the peak temperature rise obtained with the uniform heat load distribution and hence the generation of a stronger thermal lens.

These two cases illustrate the effect of nonuniform pump deposition in the presence of isothermal boundary conditions. Yet, in our laser the curved surface of the rod was not isothermal since clear optical access must be maintained. Therefore, a third case was modelled, which simulated the laser rod boundary conditions more accurately with 30.5 °C isothermal heatsinking at the flat surface and convection cooling to ambient air at 23.8 °C over the curved surface. The resulting temperature distribution shown in figure 2.2.11 has a stronger thermal lens than for the isothermal boundary conditions (see figure 2.2.10) and is decentered by approximately 0.5 mm. This decentering of the thermally induced lens leads to a beam deflection that we estimate to be 0.16 mrad for the measured focal length of 3.2 m, while the measured beam deflection was 0.3 mrad.

The analytical result obtained earlier by applying equation (7) of [3] assumed isothermal boundary conditions, which in our numerical model underestimated the maximum temperature rise by a factor of two (2 °C in figure 2.2.10 instead of 4 °C in figure 2.2.11) compared to the real boundary conditions. Hence, the analytical estimate of the lens focal length is also underestimated by this factor of two. A suitable correction to the analytical model is to reduce the thermal lens coefficient from 1.96×10^3 W-cm to 0.98×10^3 W-cm, which is in close agreement with the value of 1.05×10^3 W-cm obtained from a least squares fit to the focal length data shown in figure 2.2.8.

The measured thermal-lens data was used in resonator calculations to determine the TEM_{00}-mode beam divergence. The beam divergence was estimated experimentally by focusing the beam with a 1-m-focal-length, plano-convex lens and by measuring the beam waist diameter (at $1/e^2$) with the Multicam System (described earlier). The calculated and measured beam-divergence data shown in figure 2.2.12 are in close agreement, thereby supporting the thermal lens data.

In addition, we also looked for evidence of thermal birefringence by adding an analyzing polarizer to our linearly polarized He-Ne laser-based probe arrangement. We saw no evidence of thermally or otherwise induced birefringence.

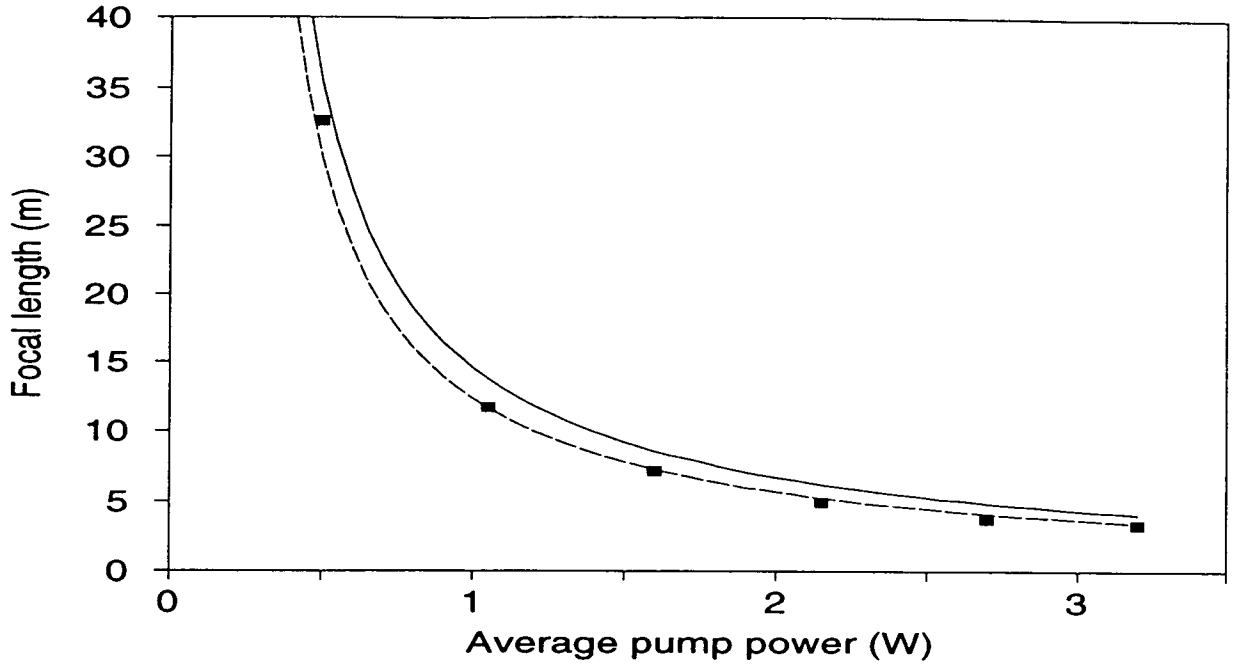

Figure 2.2.8 Thermally induced lensing as a function of the average incident pump power. Solid line is the calculated lensing using equation (7) of [3]. Dashed line is a least squares fit to the function f = M/P, where M = 1.05 x 10^3 Wcm.

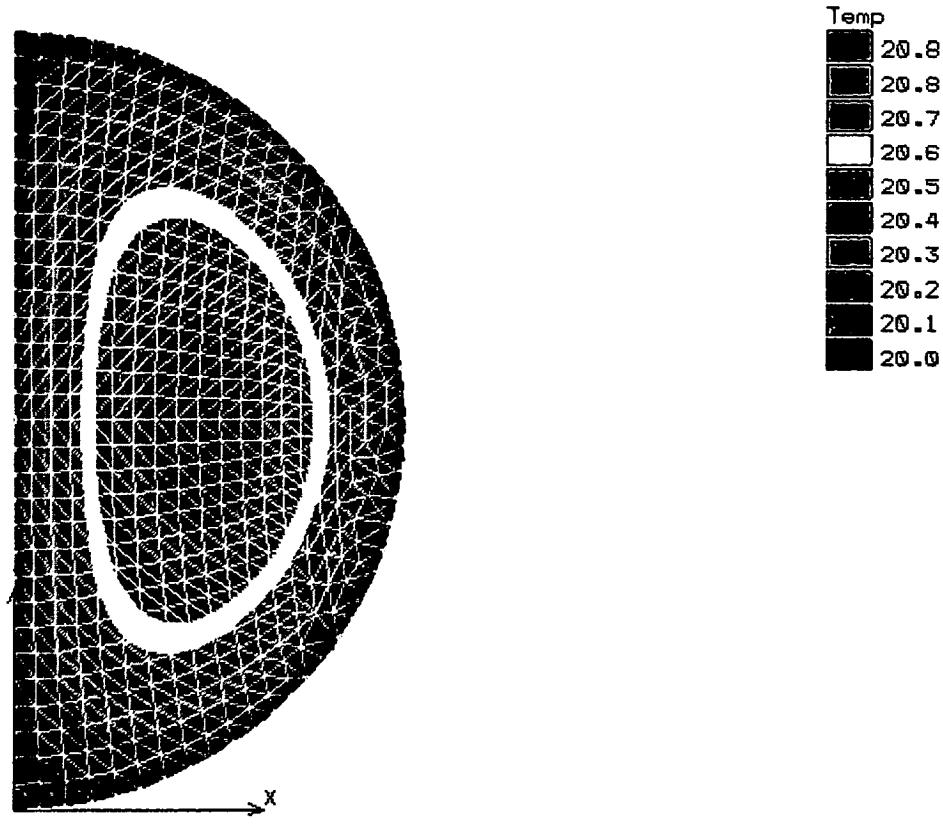

Figure 2.2.9 Temperature profile for a laser rod with 20 °C isothermal boundary conditions and 0.6 W heat load with uniform heat deposition.

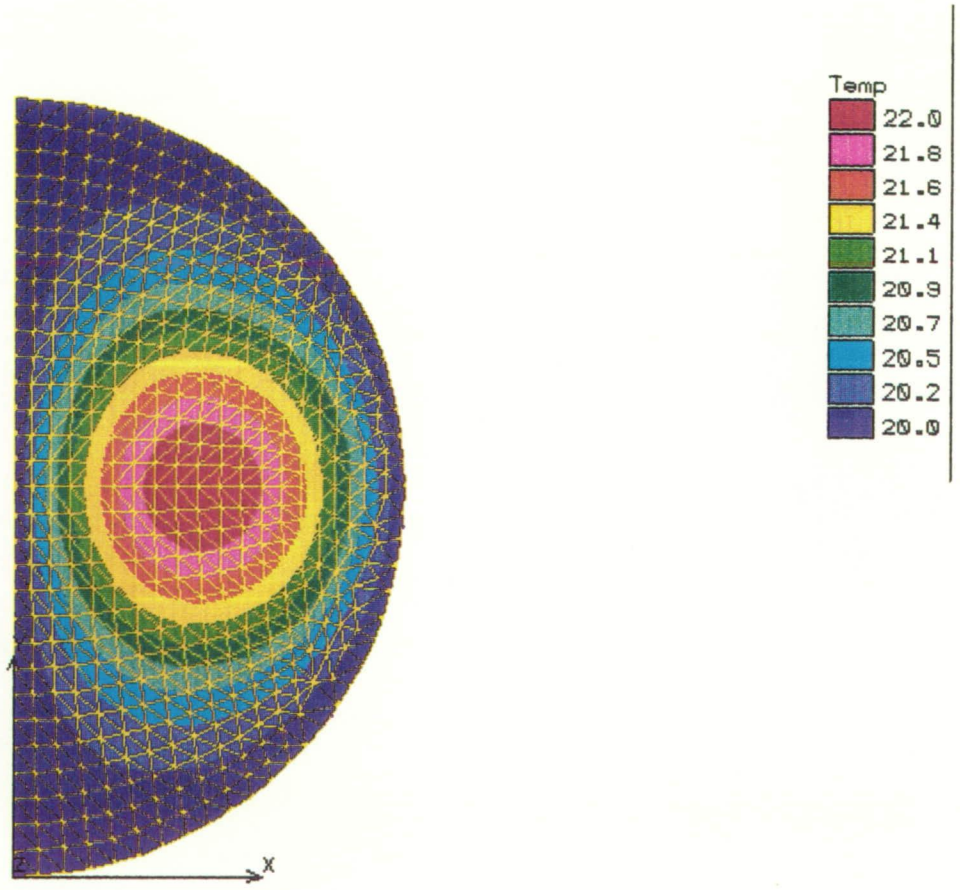

Figure 2.2.10 Temperature profile for a laser rod with 20 °C isothermal boundary conditions and 0.6 W heat load with the near-Gaussain heat deposition corresponding to the five-bar diode-laser array pumping geometry.

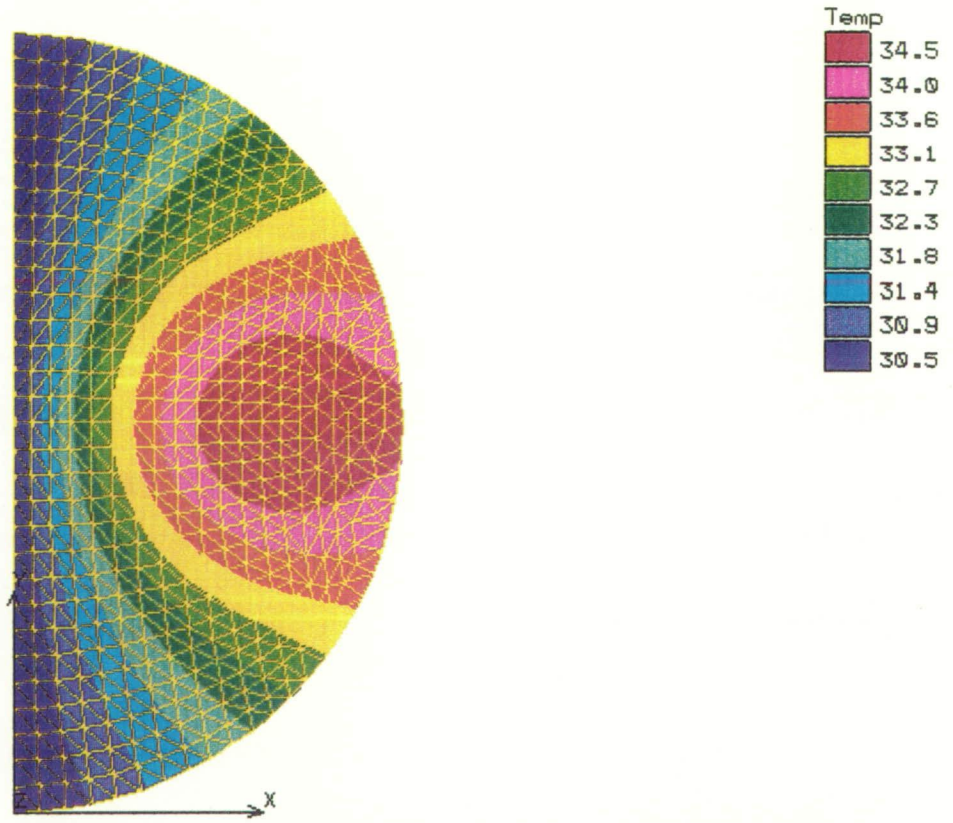

Figure 2.2.11 Temperature profile for a laser rod with the near-Gaussian deposition corresponding to the five-bar diode-laser array with a 0.6 W heat load. The boundary conditions of a 30.5 °C isothermal on the flat heatsink surface and convection cooling of the curved face at an ambient air temperature of 23.8 °C were measured.

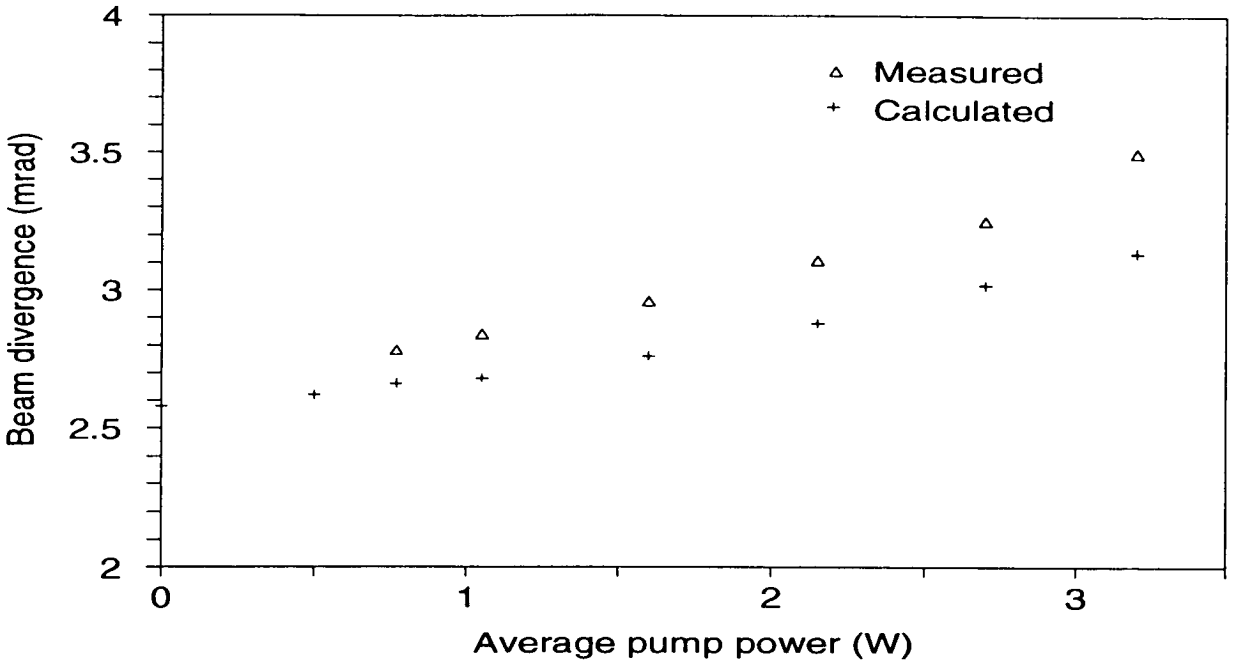

Figure 2.2.12 Comparison of measured and calculated resonator beam divergences as a function of the average incident pump power.

2.3 *Normal-Mode Laser Operation at 1.064 μm.*

Normal-mode laser operation was initally investigated with the SDL three-bar diode-laser array and both Brewtser-angled rod orientations. The laser resonator contained one laser rod pumped by a maximum of 36 mJ energy. A 35-cm long, linear resonator consisting of a flat output coupler and a concave, 50-cm radius, high-reflector was placed around the laser rod. The laser rod was positioned close to the flat mirror for multimode operation and was placed close to the concave mirror for TEM_{00}-mode operation. TEM_{00}-mode operation was optimized by monitoring the beam profile while adjusting the laser rod axial position in the resonator for maximum output.

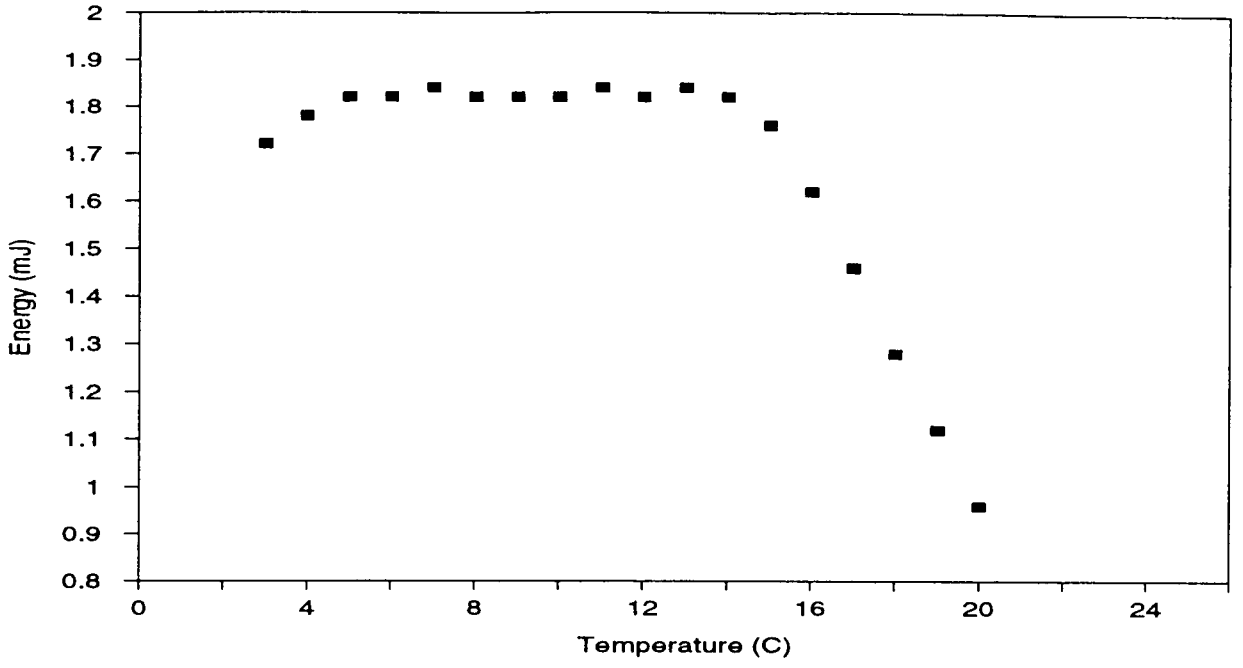

Figure 2.3.1 Laser output energy as a function of diode-laser array temperature.

Different output couplers were used to obtain estimates of intracavity loss from a Findlay-Clay analysis of the laser thresholds. In addition, the spacing between the diode-laser array and the laser rod was varied and the observation made that smaller spacings reduced threshold and increased slope efficiencies as a result of the reduced pumped volume (see fluorescence data in Section 2.2).

Absorption of the diode-laser energy was optimized by observing the TEM_{00} laser output energy as a function of heatsink temperature (see figure 2.3.1). There was no single optimum pump wavelength, but a region that extended from 805.5 nm to 808 nm. We chose to operate at 13°C (807.7 nm) to reduce the possibility of water vapor condensation on the laser heatsink.

For multimode laser operation the calculated TEM_{00}-mode radii ($1/e^2$) at the center of the laser rod were 326 μm along the x-axis and 179 μm along the y-axis. The laser rod was in the horizontal Brewster configuration and provided a clear aperture of approximately five-times the smaller mode-radius. Hence, apodization losses were negligble.

Figures 2.3.2 through 2.3.4 show the input/output data and Findlay-Clay analysis. The maximum pulse energy obtained was 9 mJ with a slope efficiency of 29% and internal loss was 3.7% per round trip. The output beam profile was highly multimode and approximately rectangular with the larger dimension parallel to the vertical y-axis.

For TEM_{00}-mode laser operation the calculated TEM_{00}-mode radii at the center of the laser rod were 517 μm along the x-axis and 933 μm along the y-axis. The laser rod was in the vertical Brewster configuration and provided a clear aperture of approximately 3 times the mode radius.

Figures 2.3.5 through 2.3.7 show the input/output data and Findlay-Clay analysis. The maximum pulse energy obtained was 2.8 mJ with a slope efficiency of 12.6% and internal loss was 28% per round trip. The intracavity loss expected from the truncation of a Gaussian beam with the appropriate circular aperture [5] would be approximately 3% per roundtrip. The cause of our estimated excess loss was never determined and was not present in later lasers. The TEM_{00} output beam profile is shown in figure 2.3.8.

The data shown in figure 2.3.9 was taken with a five-bar laser-diode array (SDL 3230) spaced 0.5 mm from a single, vertical-Brewster orientation, laser rod. This spacing gives the optimum energy conversion for TEM_{00}-mode laser operation as determined experimentally.

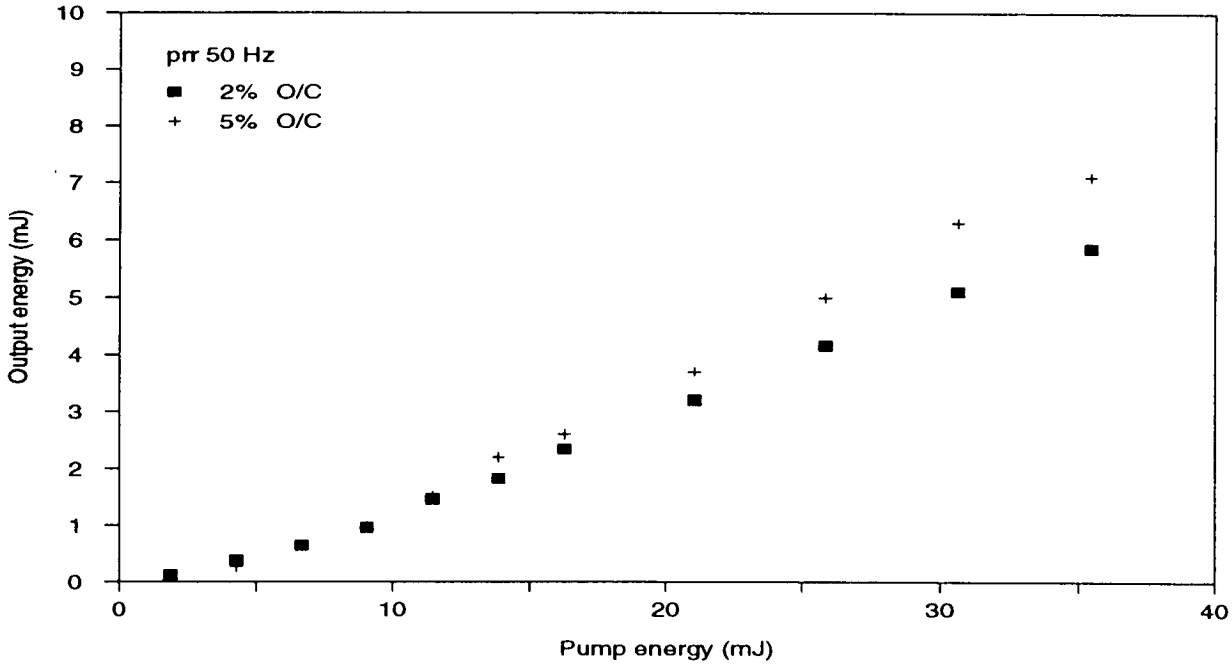

Figure 2.3.2 Multimode output characteristics as a function of output coupling.

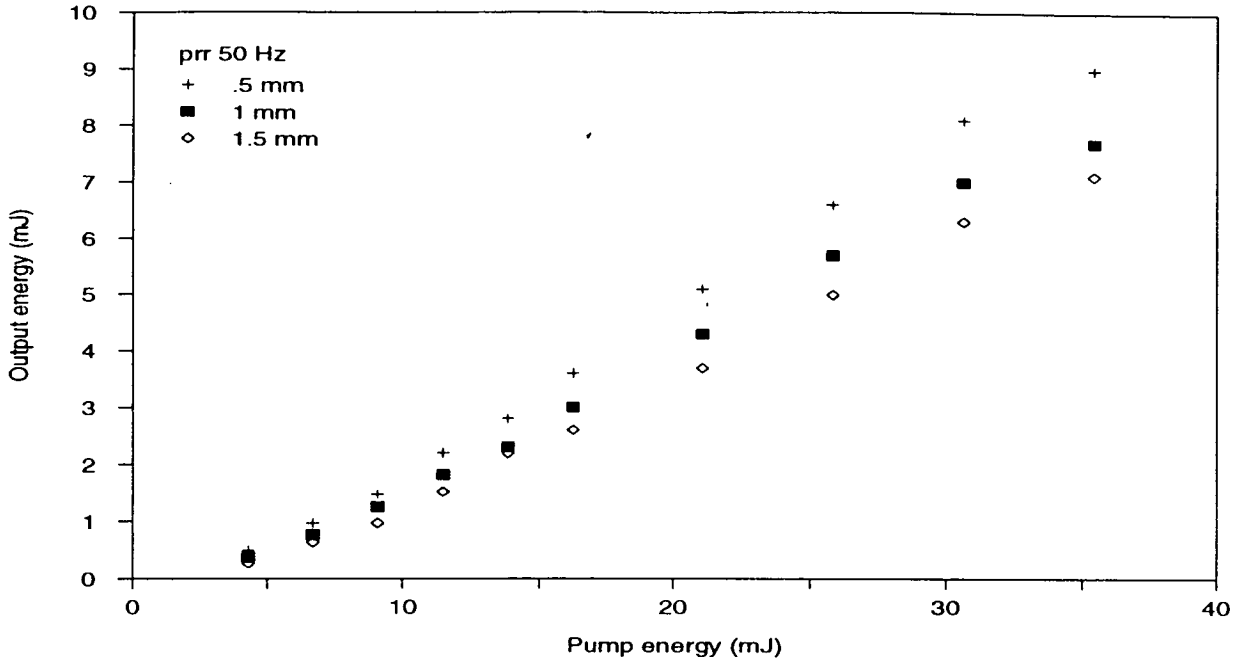

Figure 2.3.3 Multimode output characteristic as a function of diode-laser array-to-rod spacing.

We again used a plano-concave resonator with a flat high-reflector placed 3.6 cm from one Brewster end-face of the laser rod and a 50-cm-radius output-coupler placed 35 cm from the other Brewster end-face. The calculated TEM_{00}-mode diameter ($1/e^2$ diameter of the intensity profile) at the laser rod was approximately 1 mm (1 mm x 1.8 mm inside due the the Brewster orientation). This resonator design suffers less than 1% loss for the TEM_{00} mode while preventing laser oscillation of higher-order modes and it provides good overlap with the pump profile.

Long-pulse (200 μs at 50 Hz) laser operation was investigated with output-coupling-transmission in the range from 2% to 25%. Optimum energy conversion was obtained with a 20% output coupler with 11.8 mJ of output at 1064 nm for 64 mJ from the 808-nm pump laser (approximately 65% was absorbed in the laser rod). Total intracavity losses were estimated to be 1.2% from a Findlay-Clay analysis of the laser threshold as a function of output coupler transmission. Figure 2.3.9 shows the output energy as a function of the pump energy incident on the laser rod with a 20% transmission output coupler. The TEM_{00}-mode slope

efficiency of 23% is comparable to that obtained by the majority of side-pumped geometries operating multimode, using a single quasi-cw laser-diode array [6,7,8], and it far exceeds their potential TEM_{00}-mode performance.

We added a second laser rod, also pumped by a five-bar diode-laser array, 1-cm away from the first rod in the 50-cm mirror side of the resonator. We obtained 22.5 mJ output in TEM_{00}-mode operation (see figure 2.3.10). Output coupling was 20% and intracavity losses were estimated at approximately 2%. The slope efficiency of 23% was almost identical to the performance of the single rod laser. This laser was operated at 20 Hz to keep a similar total value of thermal lensing in the laser rods and equivalent TEM_{00}-mode size as in the single-rod laser.

The output beam profile (with 64 mJ pump energy) in figure 2.3.11 shows greater than a 0.96 correlation with a least squares fit to a Gaussian beam-profile and less than 3% deviation from circular symmetry. The mean beam diameter of 3.7 mm approximately 1 m from the output coupler was larger than expected from resonator calculations. This prompted us to investigate the thermo-optical properties of the pumped laser rod. The results of this investigation are described in Section 2.2.

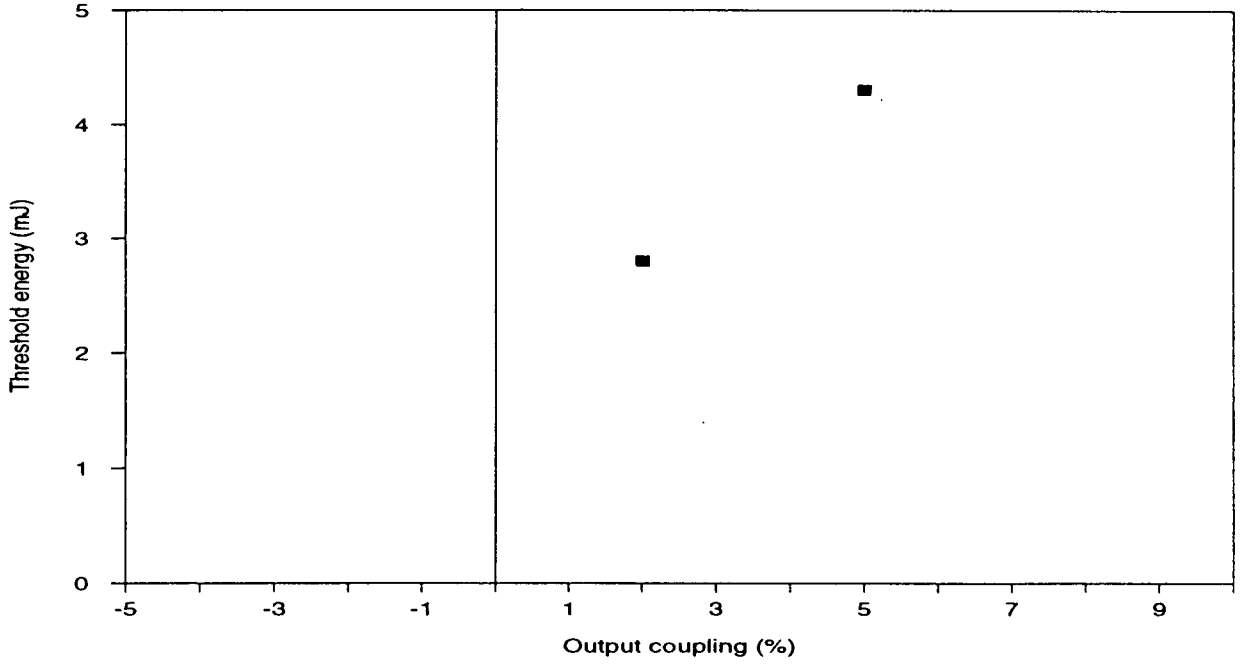

Figure 2.3.4 Findlay-Clay plot for the multimode resonator.

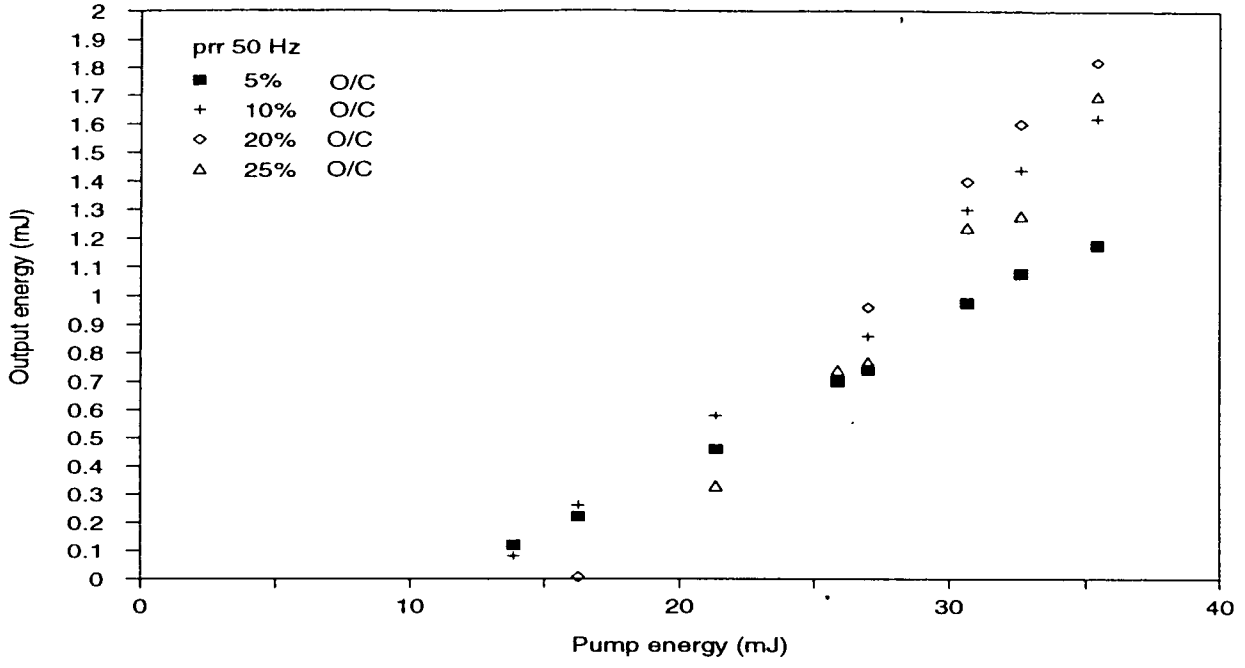

Figure 2.3.5 TEM_{00} output characteristics as a function of output coupling.

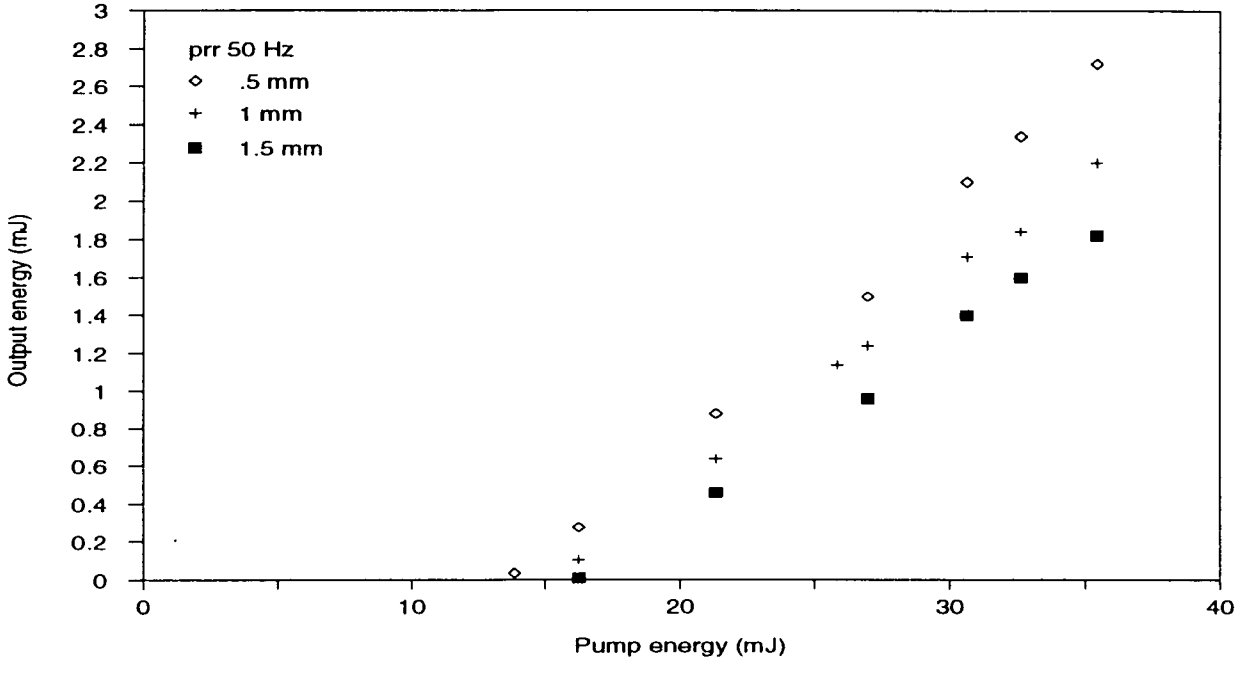

Figure 2.3.6 TEM_{00} output characteristic as a function of pump array-to-rod spacing.

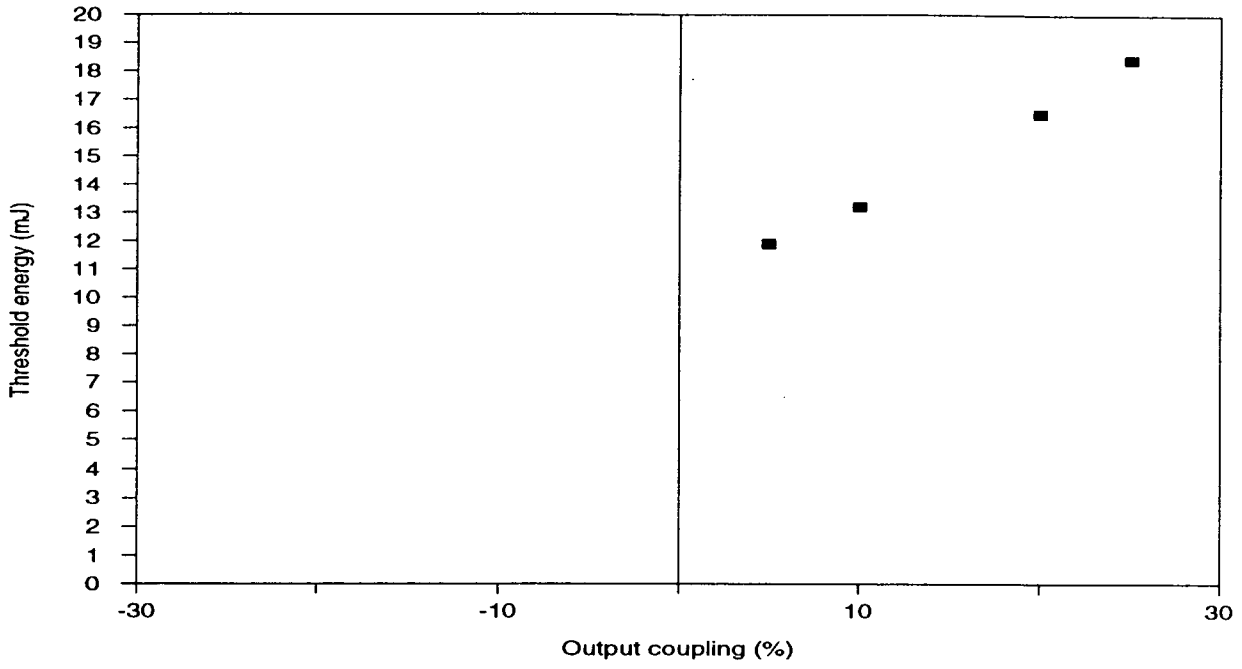

Figure 2.3.7 Findlay-Clay data for the TEM_{00} resonator.

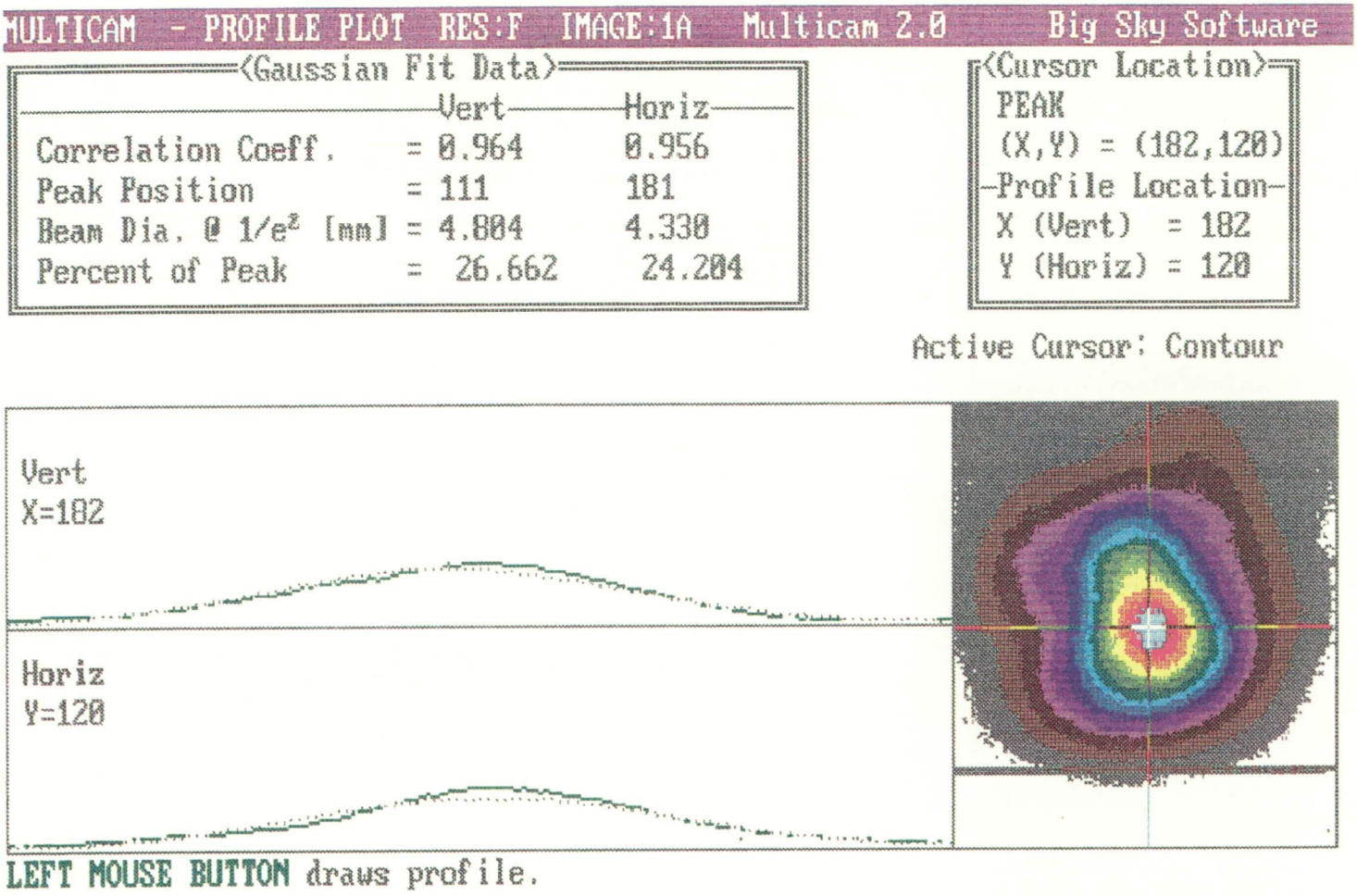

Figure 2.3.8 TEM_{00}-mode profile for a single-rod laser pumped with a three-bar diode-laser array.

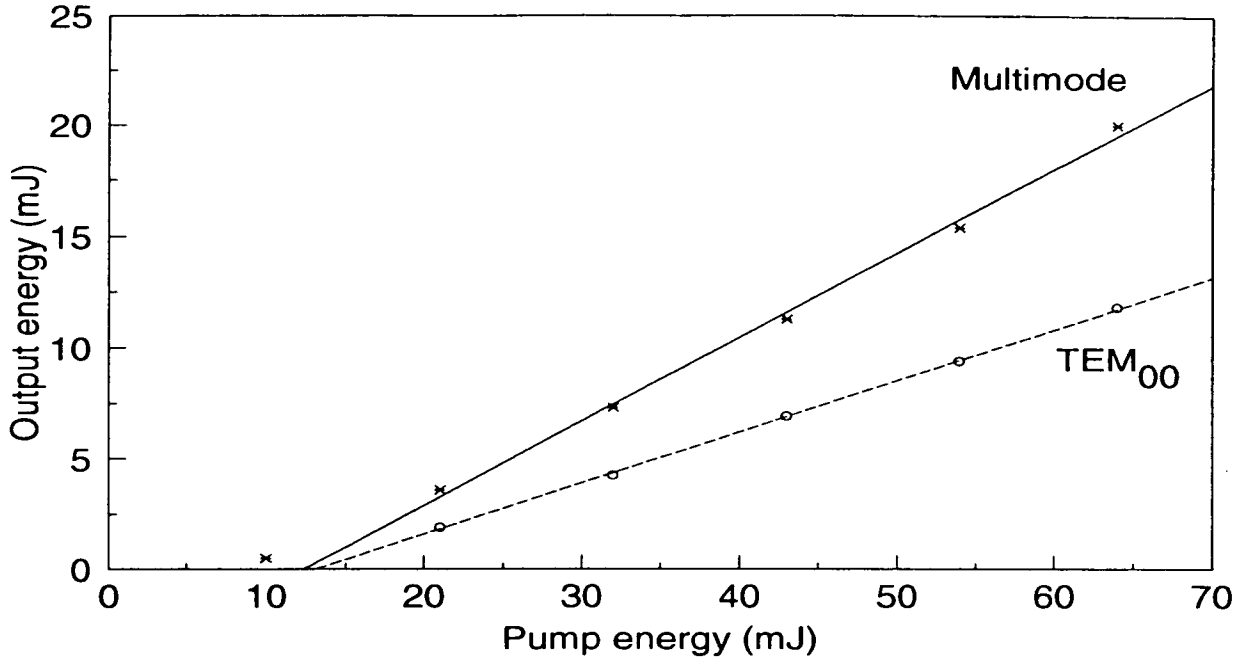

Figure 2.3.9 TEM_{00}-mode laser output characteristic at 50 Hz with a single laser rod pumped by a five-bar diode-laser array.

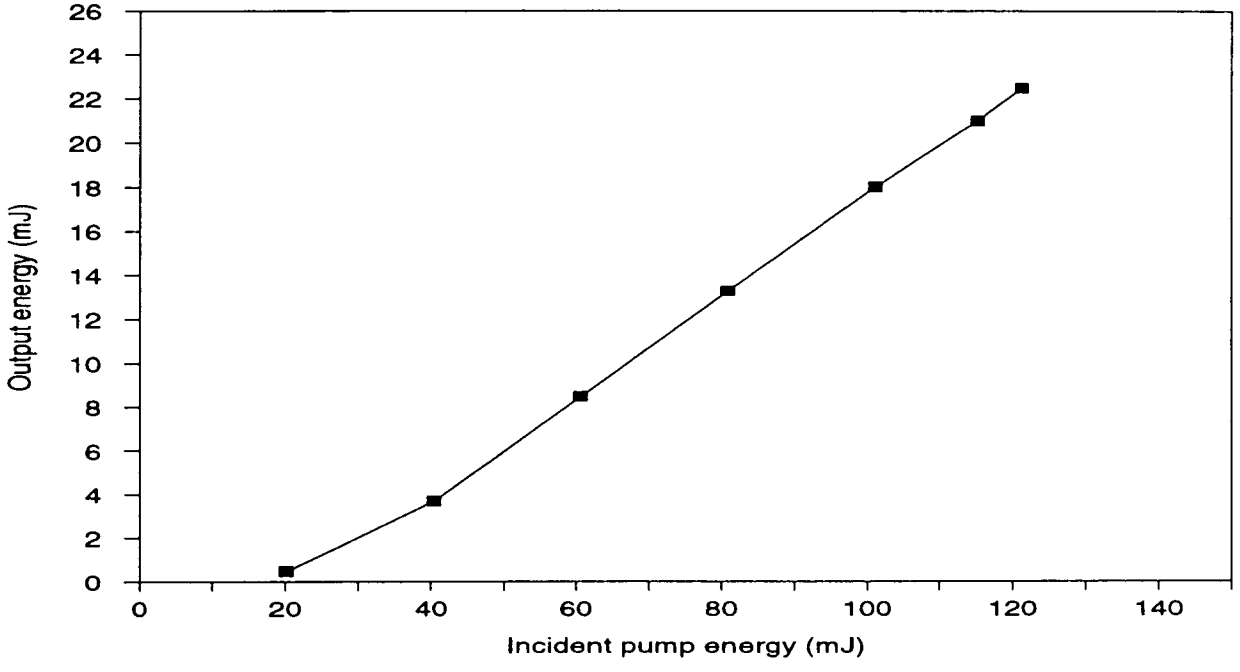

Figure 2.3.10 TEM_{00}-mode laser performance at 20 Hz with two D-shaped laser rods.

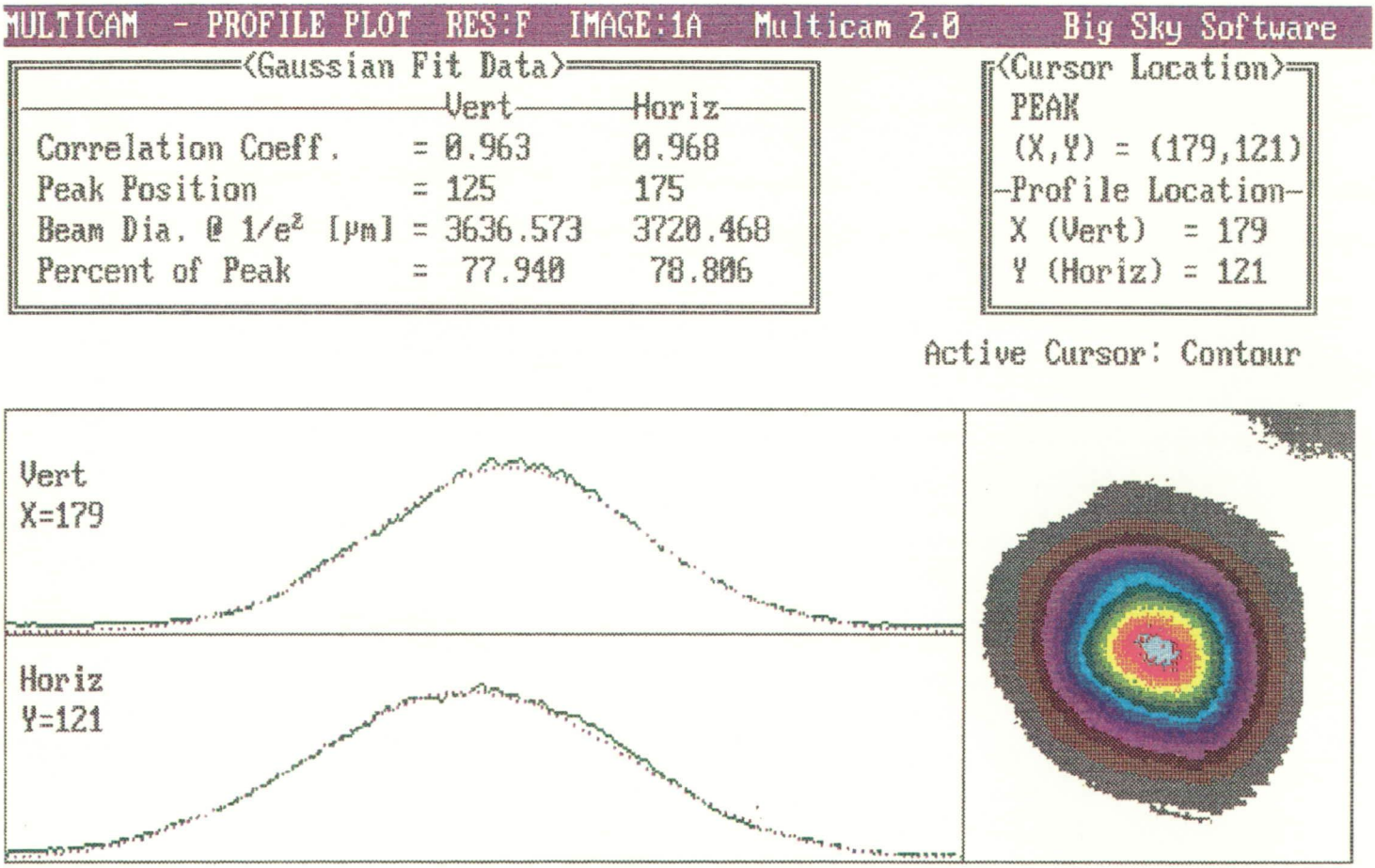

Figure 2.3.11 TEM_{00}-mode profile for a single-rod laser pumped with a five-bar diode-laser array.

2.4 *Normal-Mode Laser Operation at 1.32 μm.*

TEM_{oo} normal-mode operation at 1.32 μm was investigated in the same two-rod laser structure described in Section 2.3. The plano-concave resonator employed a 45-cm radius-of-curvature, high-reflector (instead of the 50-cm radius-of-curvature, high-reflector used in the 1.064 μm resonator) to compensate for the change in mode-size with wavelength. TEM_{00}-mode output energies up to 10.2 mJ and 15% slope efficiency were obtained as shown in figure 2.4.1. The transmission of the output coupler was 18% at 1.32 μm.

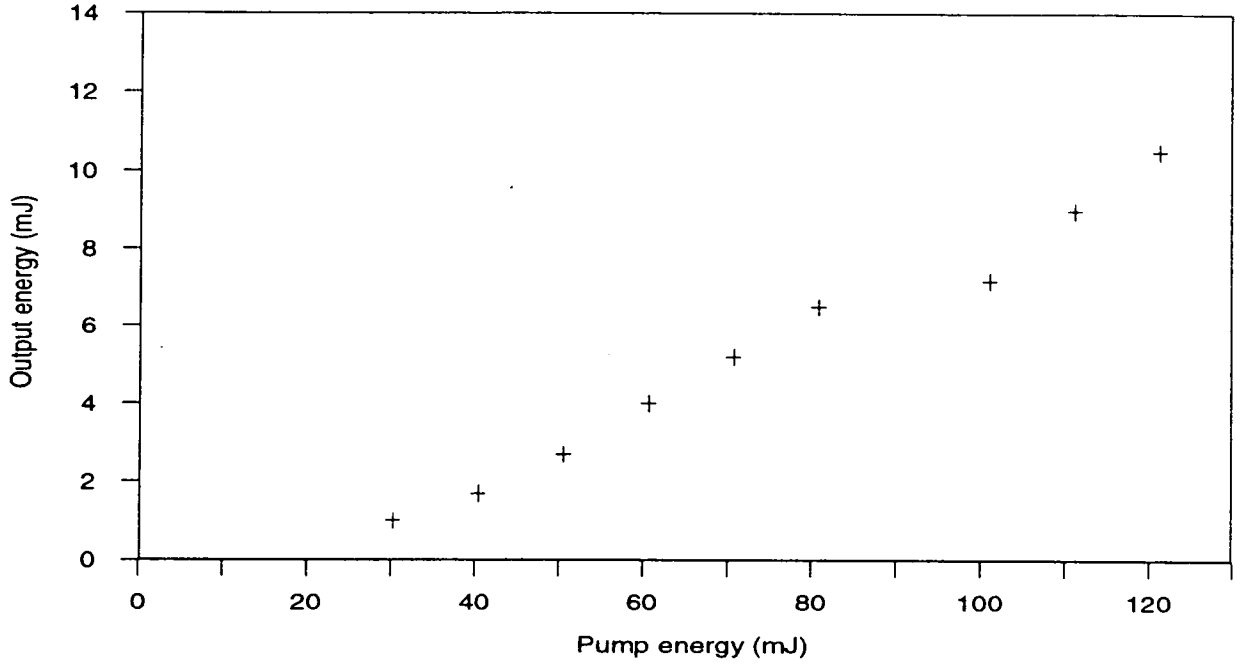

Figure 2.4.1 TEM_{00} Normal-mode output data for 1.32 μm.

3 Q-Switched Laser Development.

3.1 *$LiNbO_3$ Q-switch Development.*

$LiNbO_3$ is an excellent Q-switch material for applications with moderate power densities, when low-drive voltages are desired. There is, however, one potential drawback, piezoelectrically driven acoustics that unintentionally modulate via the photoelastic birefringence response [9]. This effect gives rise to a polarization modulation of the transmitted light after any rapid change in bias conditions. The unwanted modulation is normally in the form of a weakly damped sinusoid with periods of several micoseconds and decay time of 100 μs. Either an acoustically-damped Q-switch mount [10] or an electrical pre-bias [9] can be used to reduce this effect.

We chose to develop an acoustically-damped Q-switch mount (see figure 3.1.1) based on the work of Wang et al. [10], because our chosen high-speed driver was not compatible with pre-bias techniques. Wang et al. showed that piezoelectric ringing in $LiNbO_3$ is due to acoustic modes transverse to the applied electric-field direction. These modes are attenuated by coupling the acoustic energy from the $LiNbO_3$ into an aluminum block via a fused-silica, acoustic impedance matching element. The $LiNbO_3$, fused-silica, and aluminum were bonded together with epoxy bonds several microns thick. Electrical contacts to the chrome-gold coated faces of $LiNbO_3$ was provided by the aluminum block sits on and a beryllium-copper spring contact attached to the aluminum block that acts as the acoustic load.

The Q-switch transmission response to a voltage step derived from a krytron Q-switch driver was observed at 632.8 nm using a He-Ne laser and a pair of crossed-polarizers as shown in figure 3.1.2. The temporal response of the Q-switch to the applied drive waveform was monitored with a fast Si-PIN photodiode.

Figures 3.1.3 and 3.1.4 each show the optical transmission (upper trace) and electrical signal across (lower trace) the Q-switch for a 1.6 kV transition. At He-Ne wavelengths the 1.6 kV bias leads to approximately $3\lambda/4$ phase retardation. Hence, the observed 3/4 sinusoid in optical transmission (seen in figure 3.1.3) as the Q-switch driver charges up to 1.6 kV. The expanded data of figure 3.1.4 shows piezoelectric ringing on both the optical and electrical signals. The optical ringing decays within 10 μs and has a period of 1.5 μs, corresponding to the fundamental acoustic mode for the 3-mm transverse dimension of the Q-switch. The ringing seen in the voltage across the Q-switch is probably that in the applied field direction, which is undamped, and does not appear to significantly affect the optical transmission.

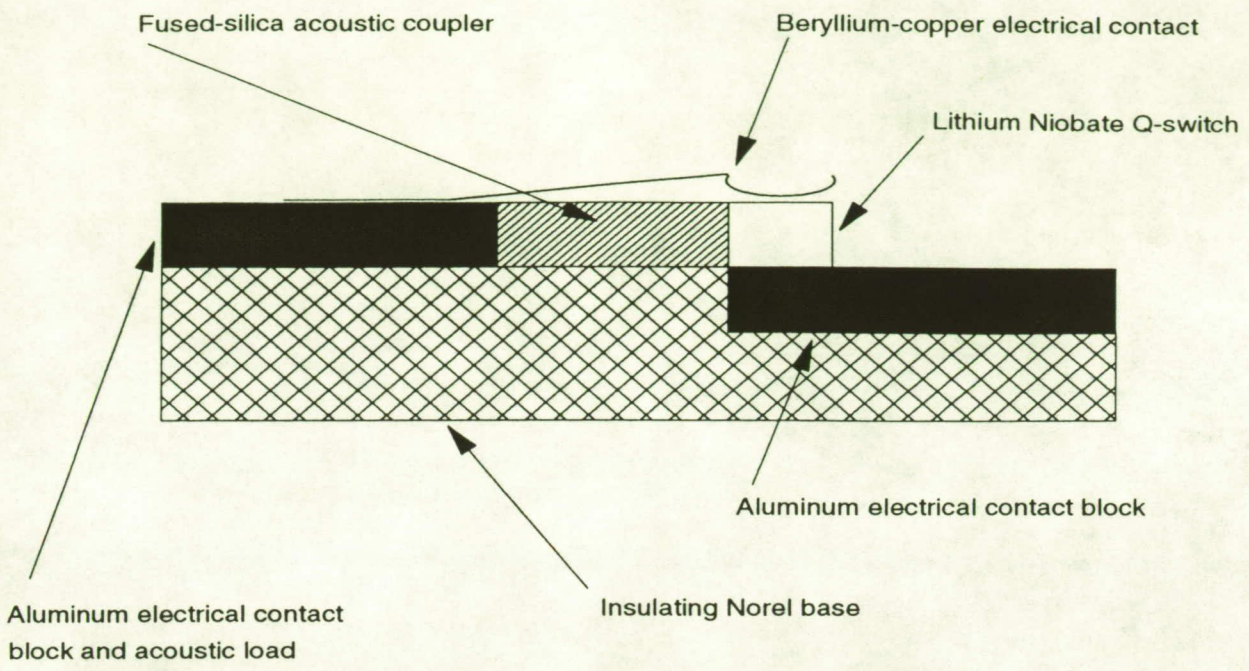

Figure 3.1.1 Acoustically-damped Q-switch mounting.

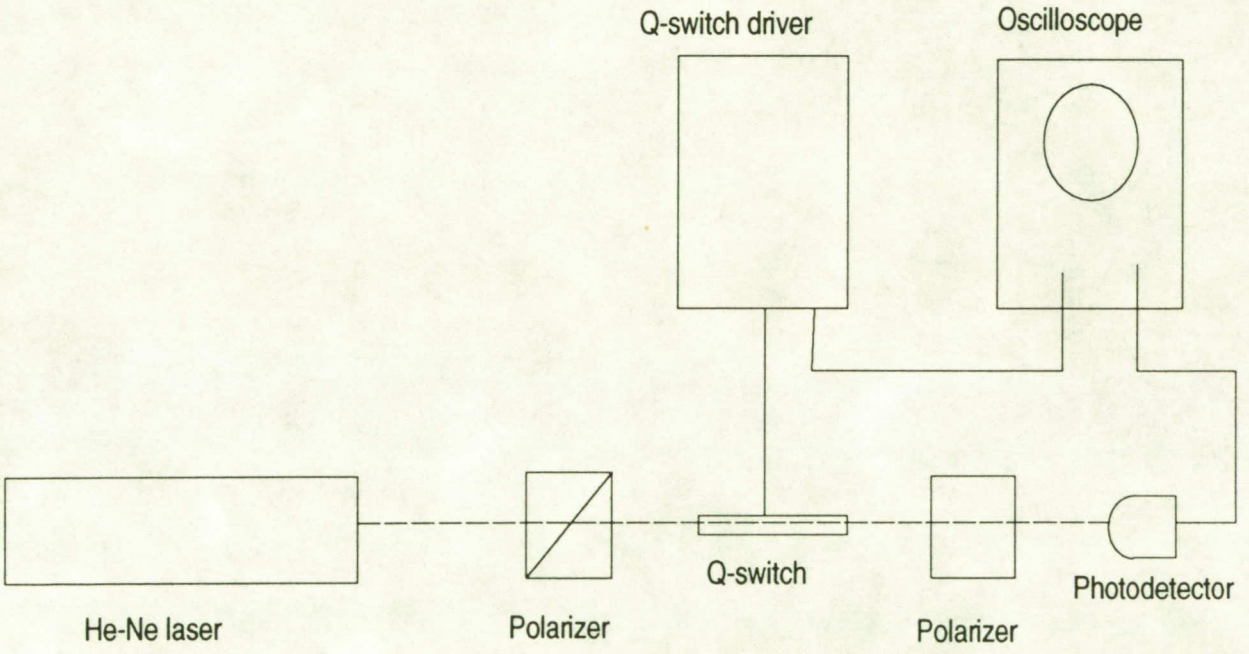

Figure 3.1.2 Schematic of the Q-switch test arrangment.

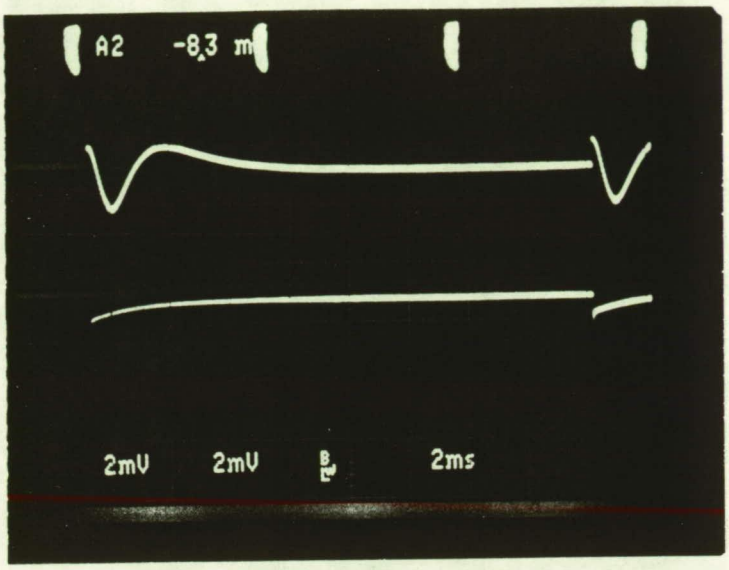

Figure 3.1.3 Optical response(upper trace) of the Q-switch to a 1.6 kV step. The lower trace is the voltage across the Q-switch.

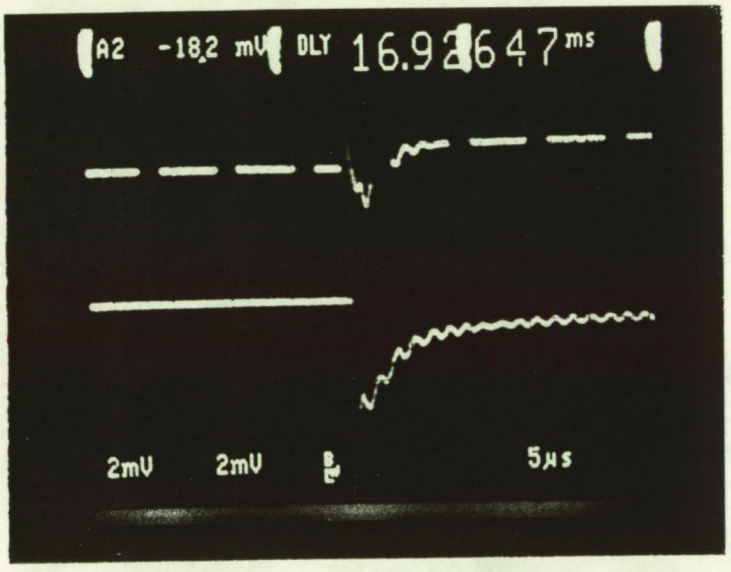

Figure 3.1.4 The 1.6 kV transition expanded to 5 µs/div.

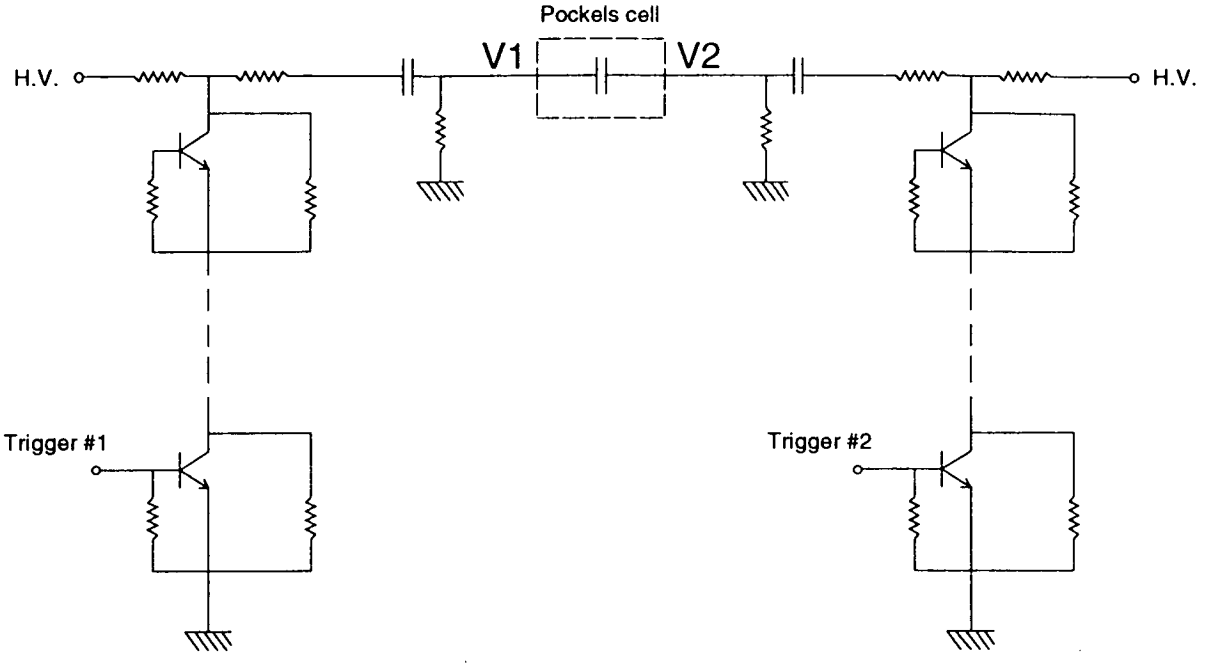

Figure 3.1.5. Q-switch driver schematic.

The Q-switch driver [11] was based on a differential avalanche stack design similar to that shown in figure 3.1.5. Both the turn-on and turn-off may be triggered independently to allow the intracavity fluence to saturate before dumping the cavity. The intracavity fluence build-up is expected to be on the order of tens of nanoseconds. An additional feature designed into the driver was an optical detector input to turn-off avalanche stack at a pre-set threshold corresponding to the intracavity fluence saturation level [12].

This Q-switch driver is suitable for both pulse reflection mode (PRM) and pulse transmission mode (PTM) Q-switched modes of operation. In a PRM Q-switched laser the laser cavity is held in a low-Q state until the end of the pump pulse and is then switched to the high-Q state until the stored energy emerges through the output coupler as a Q-switched pulse. In a PTM Q-switched laser there is no output coupler and the intracavity fluence builds up after the Q-switch changes to the high-Q state and remains circulating until cavity dumped (off a polarizer) when the Q-switch is returned to the low-Q state again. The timing and voltages applied to the Pockels cell are more critical to sucessful PTM Q-switched operation than for PRM Q-switched operation.

Prior to assembling the Q-switched laser, we placed the Q-switch assembly between a pair of crossed polarizers and performed transmission measurements with a 1.064 μm probe beam (derived from the normal-mode laser of Section 2.3). Initial DC biasing demonstrated a half-wave voltage of 1.15 kV and the unbiased device exhibited an extinction ratio of approximately 2900-to-1 (the polarizers alone gave 16,000:1). These two data points are indicative of typical $LiNbO_3$ with a low-strain mounting system.

However, when the Q-switch was driven in the pulsed-mode with a 100-ns-duration, 1.6 kV drive pulse (the calculated dynamic half-wave voltage is 1.6 kV) the observed transmission between the polarizers was only 34%. We investigated the effect of different drive voltages and used a high-voltage probe to observe the electrical waveform at the Q-switch mounting. The 1.6 kV was present at the Q-switch mounting implying a dynamic problem with the mounting structure and/or the $LiNbO_3$, which reduces the effective internal field and polarization rotation of the $LiNbO_3$ crystal.

We improved the contact resistance of the connections to the $LiNbO_3$ by bonding copper leads to the gold coated faces of the crystal with a conductive silver epoxy (Master Bond #EP21TDCS). The measured DC half-wave voltage was 1.05 kV for a 1.064 μm probe beam with the Pockels cell placed between a pair of crossed polarizers. This value was 100 V less than that previously measured with only spring loaded beryllium-copper contacts and is a strong indicator of greatly reduced contact resistance.

However, when the Q-switch was driven in the pulsed-mode with a 100-ns-duration, nominally 1.6 kV drive pulse (the calculated dynamic half-wave voltage is 1.6 kV) the observed transmission between the polarizers was still only 27%. We used a high-voltage probe to observe the electrical waveforms at the Q-switch mounting and discovered the effective drive voltage to be only 1.25 kV over most of the 100 nS with a 400 V overshoot on both leading and trailing edges. Figure 3.1.6 shows oscilloscope photographs of the measured waveforms and the optical probe beam intensity. The voltage applied to the Pockels cell is the diffference between the two voltage waveforms. The overshoot on the measured voltages was partially due to the response of the high-voltage probe and was not seen in the probe beam.

Waveform @ V1

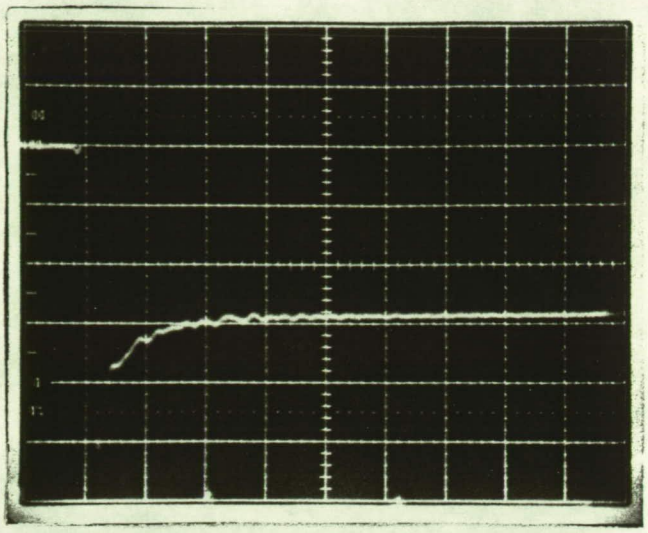

Waveform @ V2

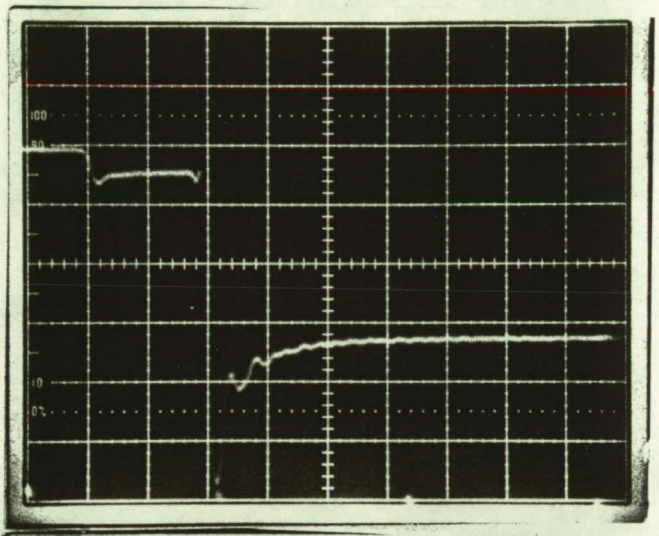

Probe beam intensity

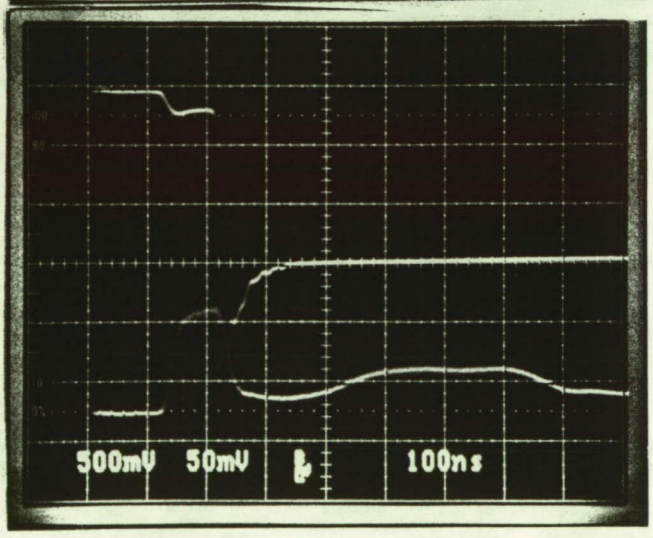

Figure 3.1.6 Pockels cell voltages and optical probe beam.

We adjusted the Pockels cell drive voltage, but were still unable to obtain high optical transmission. We then changed our probe beam from the 200 μS long normal-mode 1.064 μm laser to a 30 nS Q-switched pulse, that was obtained by intoducing a passive saturable absorber into the normal-mode laser resonator (see Section 3.4). The optical transmission of the Pockels cell was now measured as high as 80% to 90%, but fluctuated from shot-to-shot.

Relative timing jitter between the Q-switched probe pulses and the Pockels cell driver made measurements difficult. Our solution to this problem was to use a KDP Pockels cell to switch out the last 10 μS of the normal-mode laser output as the probe beam. Once again this shorter duration probe pulse indicated higher optical transmission through our $LiNbO_3$ Pockels cell. An explanation for the observed behaviour is that during the long (200 μS) probe pulse charge carriers are generated and trapped via the photorefractive effect and distort the dynamic electro-optic interaction. The timescale for this charge build-up is longer than the shorter (30 nS or 10 μs) probe pulses and the probe signal distortion is not observed under these conditions.

After implementing the 10 μS probe pulses we have been able to adjust the Pockels cell driver to obtain approximately 95% optical transmission. Further improvement was not possible within the constraint of the Phase II effort. The Q-switch performance is more than adequate for PRM Q-switching, while PTM Q-switching losses will be significant because of the Q-switch transmission loss.

3.2 *PRM Q-Switched Laser Operation at 1.064 μm.*

All the Q-switched lasers described in this section used the same two-rod gain-module described in Section 2.2. Both the PRM and PTM Q-switched lasers used the same basic resonator shown in figure 3.2.1. An intracavity-telescope was added to expand the mode-size in the Q-switch, thereby reducing the intracavity power-density to minimize the possibility of optical damage to the $LiNbO_3$. In addition, the mode-size in the laser rods were optimized for efficient TEM_{00}-mode operation.

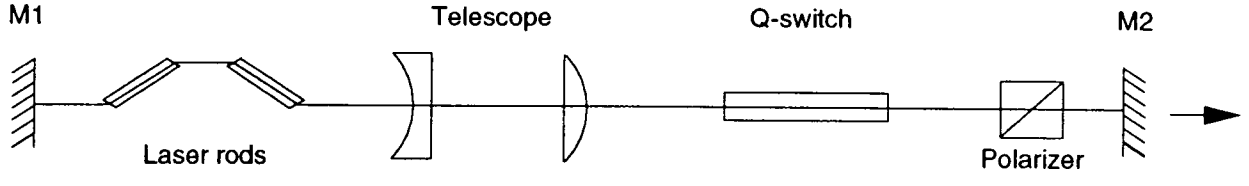

Figure 3.2.1 Schematic representation of the PRM Q-switched laser resonator.

The TEM_{00}-mode energy extraction was experimentally optimized in the two-rod normal-mode laser and the resulting mode-radius (in the horizontal direction) was approximately 600 μm. The Q-switch had a 3x3 mm clear aperture and can support a mode-radius up to 950 μm for 1% insertion loss [5]. In order to reduce intracavity losses and optimize TEM_{00}-mode performance we chose 600 μm and 850 μm as goals for the mode-radii in the laser rods and the Q-switch, respectively.

Tables 3.2.1 and 3.2.2 list the (horizontal) mode radii for the laser rods and Q-switch in the resonator (shown schematically in figure 3.2.1) as a function of the mirror radii of curvature and include the effects of thermal lensing in the laser rods. The resonator designs we consider to be optimum are highlighted in bold text.

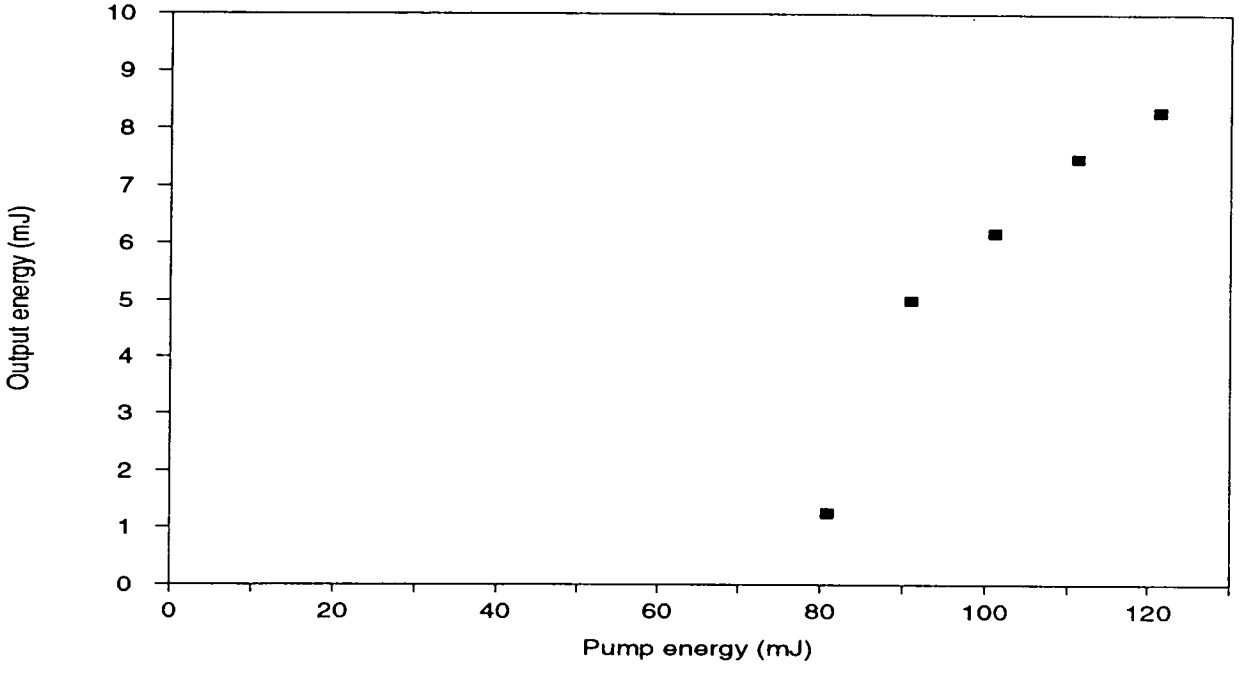

Figure 3.2.2 PRM Q-switched, 1.064-μm laser output data.

Table 3.2.1 Q-switched laser resonator parameters for operation at 20 Hz.

M1 radius (cm)	M2 radius (cm)	Telescope mag'	Laser rod mode radius (μm)	Q-switch mode radius (μm)
flat	flat	1.5	564	832
flat	flat	1.76	553	959
flat	flat	2.0	546	1078
-500	flat	1.5	890	1334
-1000	flat	1.5	645	959
-1500	flat	1.5	611	907
-2000	**flat**	**1.5**	**596**	**885**

Table 3.2.2 Q-switched laser resonator parameters for operation at 50 Hz.

M1 radius (cm)	M2 radius (cm)	Telescope mag'	Laser rod mode radius (μm)	Q-switch mode radius (μm)
flat	flat	1.5	453	652
flat	flat	1.76	444	753
flat	flat	2.0	438	847
-200	flat	1.5	700	1047
-300	flat	1.5	550	813
-400	flat	1.5	515	756
-200	flat	1.76	687	1205
-500	flat	1.76	489	841
-1000	flat	1.76	463	792
-2000	-500	1.5	677	943
-2000	-600	1.5	606	849
-300	-2000	1.5	633	927
-400	-2000	1.5	569	827
-400	**-1500**	**1.5**	**594**	**861**
flat	-500	1.5	621	862

The TEM_{00}-mode-energy extraction was experimentally optimized by fine tuning the telescope magnification in normal-mode operation at 20 Hz. The maximum output energy obtained was 16.5 mJ with approximately 120 mJ of incident pump energy. This was 73% of the normal-mode output obtained previously with the same output coupling (T=20%) in a simple two mirror resonator. The extraction efficiency was limited due to increased resonator losses from the extra components. In addition, a reduction in the overlap of the TEM_{00} mode and the absorbed pump energy profile in the laser rods in the Q-switched resonator design also decreases extracted energy.

Conventional PRM Q-switched operation yielded 10-ns to 20-ns pulses with energies as high as 8.3 mJ, while using 50% transmission output coupling. No attempt was made to optimize the pulse duration or energy by varying the output coupling.

3.3 *PTM Q-Switched Laser Operation at 1.064 μm.*

The PTM Q-switched laser was identical to the PRM resonator, except for the replacement of output coupler, M2, with a high-reflector. When operating in the PTM Q-switched mode, the output was "cavity-dumped" via the intracavity polarizer. The precise timing of the rising and falling edges of the Q-switch waveform was critical for efficient energy extraction within a single, short-duration pulse. The rising-edge timing was adjusted to optimize intracavity energy by monitoring fluorescence leakage from the resonator with a Si-PIN photodiode, while driving the Q-switch with a relatively long step waveform (several hundred microsoeconds in duration). Then the falling-edge timing was adjusted to optimize the pulse energy in a single output pulse.

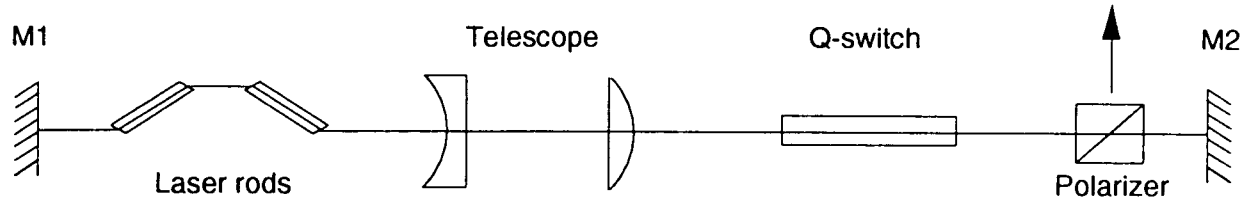

Figure 3.3.1 Schematic representation of the PTM Q-switched laser resonator.

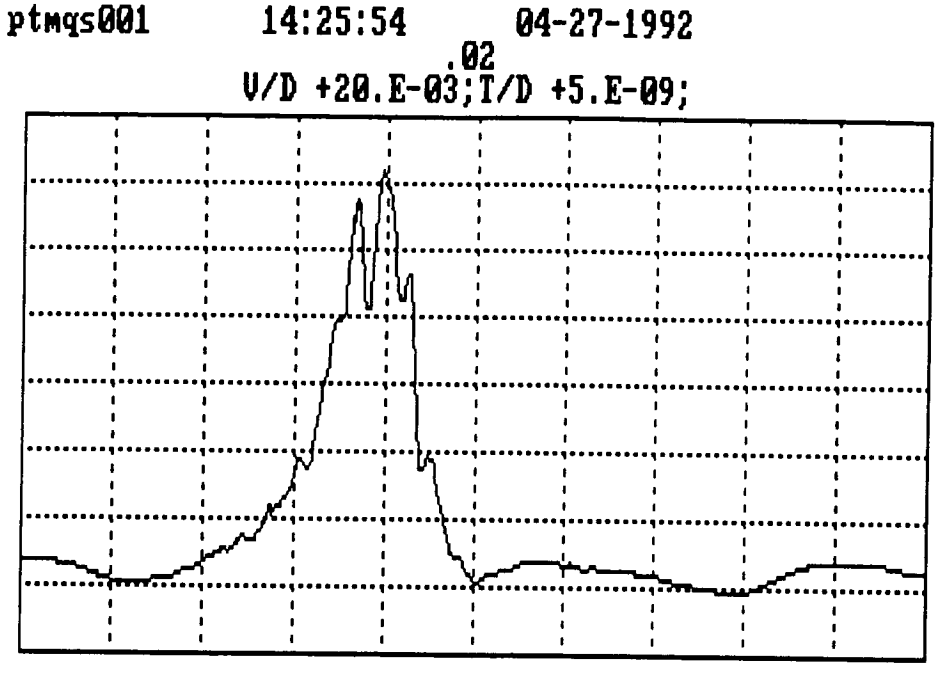

Figure 3.3.2 An optimally timed, 2-mJ PTM Q-switched pulse. (5 ns/div).

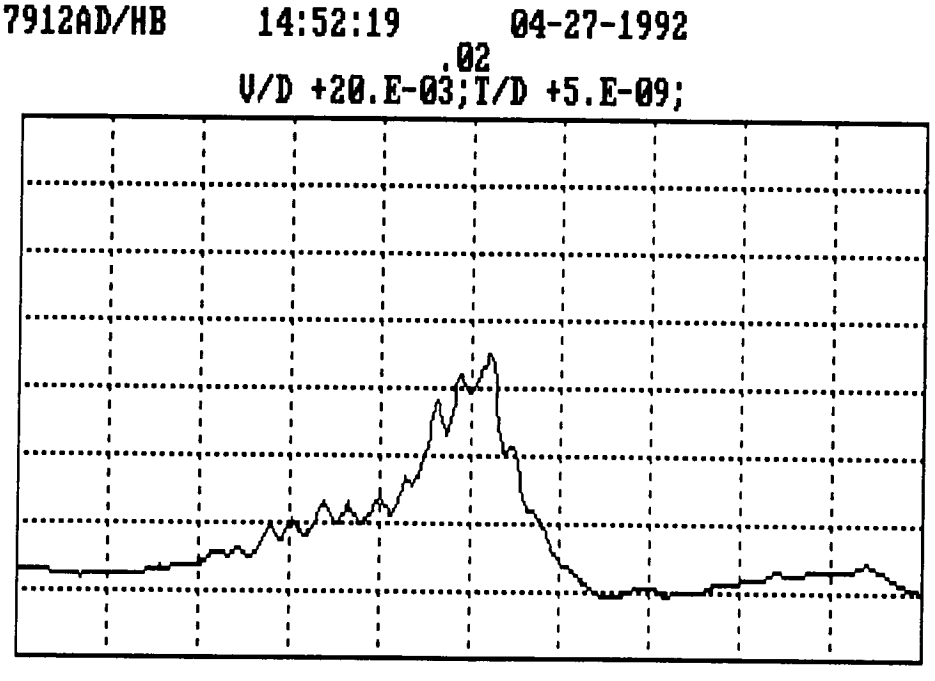

Figure 3.3.3 PTM Q-switched pulse with 10-ns Q-switch delay. (5 ns/div).

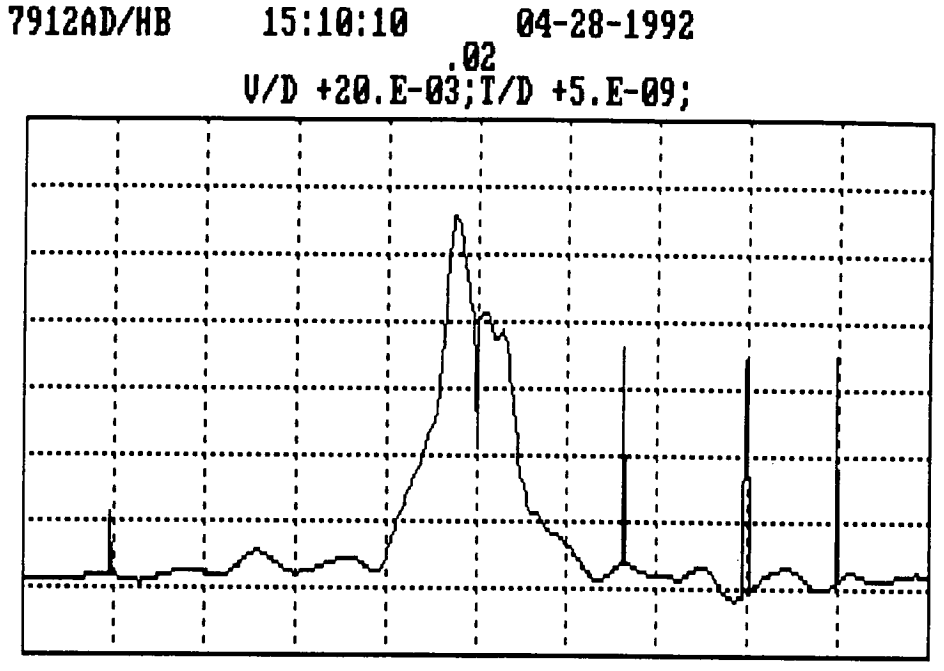

Figure 3.3.4 A 4.5-mJ PTM Q-switched laser pulse.

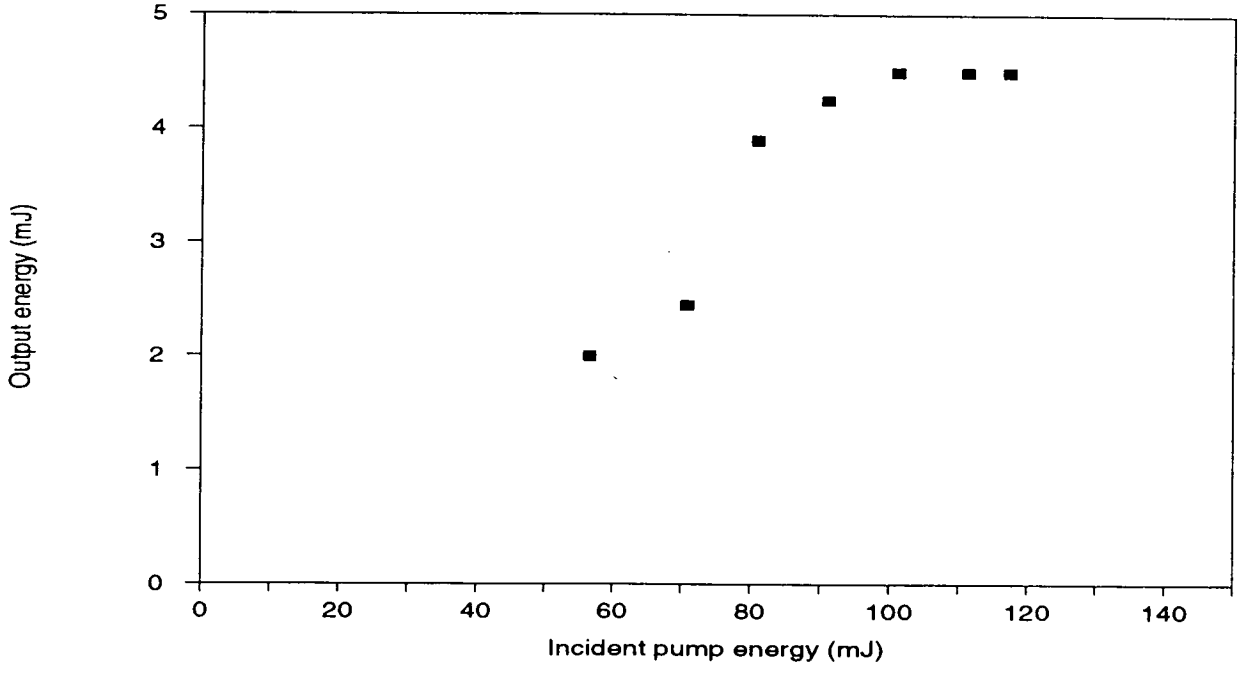

Figure 3.3.5 PTM Q-switched pulse energy as a function of pump energy.

Figure 3.3.2 shows the temporal output for optimum falling-edge timing. Figure 3.3.3 shows the result of a 10-ns delay beyond this optimum. The optimized output pulsewidth was 5 ns, with 30% intensity modulation due to longitudinal mode-beating. Both figures 3.3.2 and 3.3.4 show 5-ns pulses with pulse energies of 2 mJ and 4.5 mJ, respectively. These data clearly demonstrate the relative insensitivity of the PTM Q-switched laser pulse duration to incident pump energy.

Figure 3.3.5 shows the output pulse energy as a function of incident pump energy. The pulse energies were limited to 4.6 mJ by optical damage to the laser rods. The fluence at the onset of damage was estimated to be approximately 0.5 Jcm^{-2}. However, with a replacement set of laser rods in the resonator, reliable operation at 4.5 mJ was been obtained for several days.

3.4 *Passively Q-switched Laser Operation at 1.064 μm.*

The compact laser-diode pumping scheme developed in this work is ideally suited to the use of a short resonator for short pulse generation in Q-switched operation, while maintaining efficient TEM_{00} conversion. In order to simplify the resonator design and eliminate Q-switch material damage and drive requirements, we have used F_2^- color centers in LiF as a saturable absorber Q-switch [13, 14, and 15]. Appendix 3, publications, contains additional information on the passivley Q-switched laser.

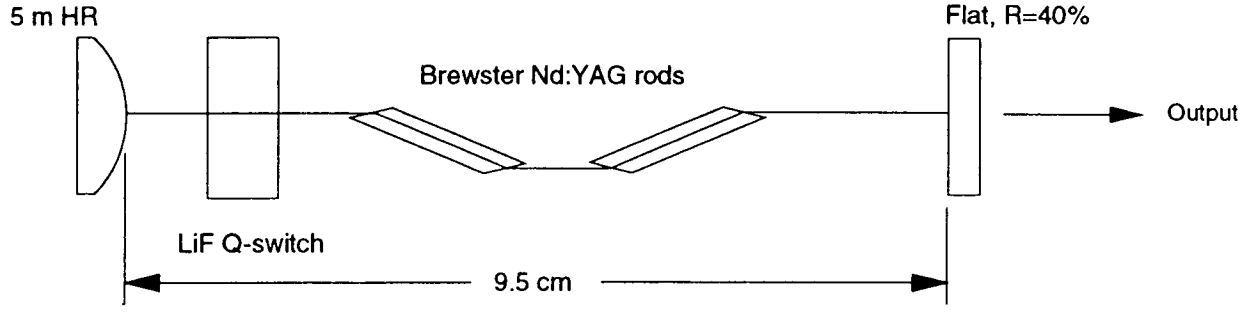

Figure 3.4.1 Passively Q-switched laser resonator.

The passively Q-switched resonator is shown in figure 3.4.1. The laser rods and pump coupling are the same as described in Section 2.3. The resonator length was as short as possible using available optics, while consistent with optimized TEM_{00}-mode efficiency. The TEM_{00}, normal-mode pulse energies (no absorber) were 19.5 mJ at 20 Hz pulse-repetition-rate for 120 mJ pump pulse energies. The conversion efficiency and slope efficiency were 16% and 22.6%,

respectively. To obtain passive Q-switching a window-like piece of AR-coated LiF crystal containing absorbing F_2^- centers was inserted into the resonator next to the high-reflector. The F_2^- centers were created by gamma-irradiation (5.5×10^8 rads total dose).

Table 3.4.1 summarizes the Q-switched performance obtained with different length F_2^-:LiF crystals, which are characterized by their unsaturated single-pass transmission T_0. The laser-diode-pump energy was equal to the threshold energy for mono-pulse generation in each case. Further increasing the pump energy leads to multiple-pulse generation with the same energy in each pulse. Note, the data for the 12%-transmission showed improved pulse durations of 2 ns. However, the pulse energies were reduced to 4 mJ by the onset of damage to one of the Nd:YAG laser rods. Once again the fluence at the onset of damage was approximately 0.5 Jcm^{-2} (see Section 3.3). Prior to this, the laser had generated 2.4 ns duration, 5 mJ pulses for a period of tens of minutes. After replacement of the damaged laser rod we have been able to operate at the 4 mJ level for over 10^7 shots with no system degradation.

Table 3.4.1 Passively Q-switched laser performance.

T_0 (%)	E_{pump} (mJ)	E_{out} (mJ)	τ (ns)
55	58	1.3	5.9
46	73	2.5	3.6
35	83	3.8	2.8
27	97	5.0	2.4
12	121	4.0	2.0

Figure 3.4.2 shows a typical 2.4 ns pulse with no evidence of longitudinal mode beating. This is indicative of single-frequency operation. Normally, one or more intracavity-etalons are required for single-frequency operation. However, in the passively Q-switched laser the slowly-opening Q-switch combined with the short resonator length, which gives rise to a longitudinal mode spacing that leads to significant differential gain between adjacent modes, ensures single-frequency operation.

The major disadvantages of the passive Q-switching technique are pulse timing jitter on the order of ± 1 μs and its restriction to the 1-μm wavelength region. Other solid-state saturable absorbers have yet to be developed for other wavelengths. The pulse amplitude stability is on the order of $\pm 3\%$ and the pulse shape and duration are equally stable from pulse-to-pulse.

Table 3.4.2 Passively Q-switched laser efficiency characteristics.

T_0 (%)	E_{pump} (mJ)	τ_{pump} (us)	Normal-mode E_{out}(mJ)	Q-switched E_{out}(mJ)	Efficiency (%)
35	83	200	8.2	3.8	46
35	60	100	6.5	3.8	58
27	97	200	10.2	5.0	49
27	87	116	8.3	5.0	60

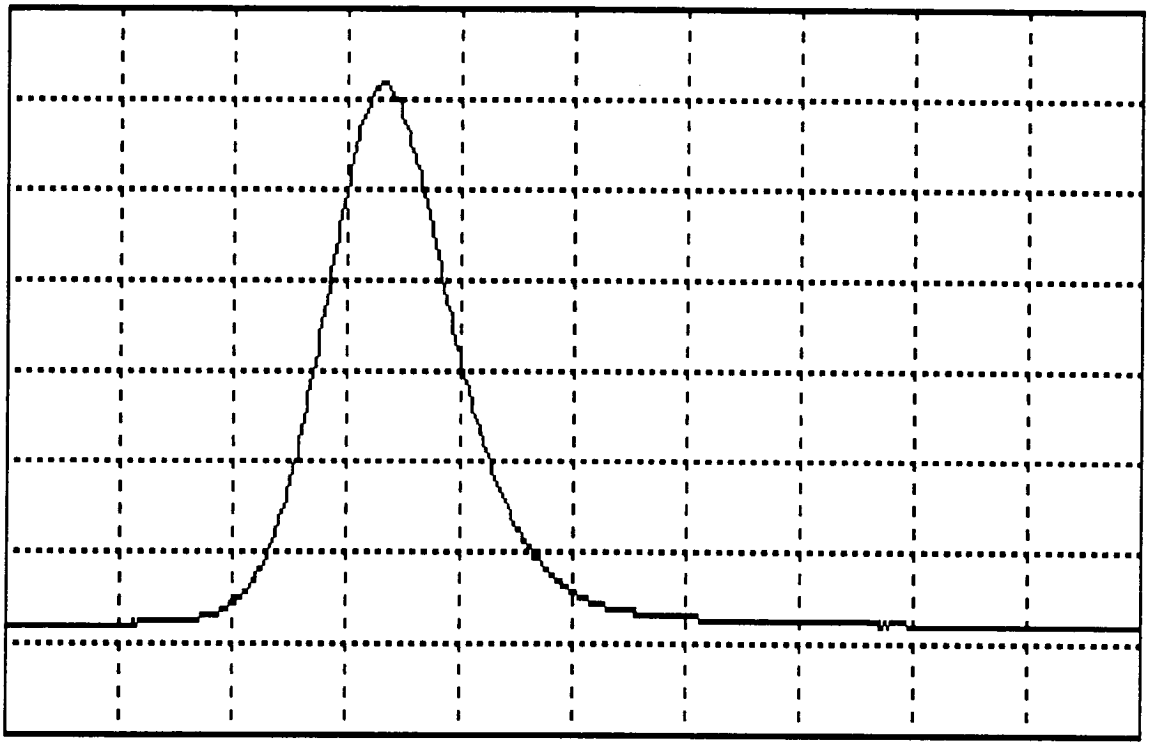

Figure 3.4.2 2.4-ns duration passively Q-switched laser pulse. (2 ns/div).

It can be seen from Table 3.4.2 that shorter pumping pulses improve the conversion efficiency of Q-switched operation. This is due to the reduction of spontaneous emission losses from the excited level of the laser medium during the pumping pulse and prior to energy extraction in the Q-switched pulse. Up to approximately 60% of the normal-mode energy was extracted in a Q-switched pulse using an absorber with 27% unsaturated transmission. Further

improvement in conversion efficiency requires optimization of the output coupler reflectivity and unsaturated Q-switch transmission. The residual losses of the passive Q-switch in the saturated state must also be taken into account.

The transmission properties of a F_2^-:LiF sample versus incident flux-density are shown in figure 3.4.3. The probe beam was from the passively Q-switched laser using the 35% unsaturated transmission, passive Q-switch material. The residual absorption of sample in the saturated state is defined by $1 - T_f$, where $T_f = \exp(-\rho l)$. Using this expression and the experimental data we estimate the residual absorption and the saturated absorption coefficient, ρ, to be 12% and 0.05 cm^{-1}, respectively. The recovery time of the F_2^--centers is approximately 100 ns, which places an upper-limit on the p.r.r. of several MHz, suitable for cw-pumped, Q-switched lasers.

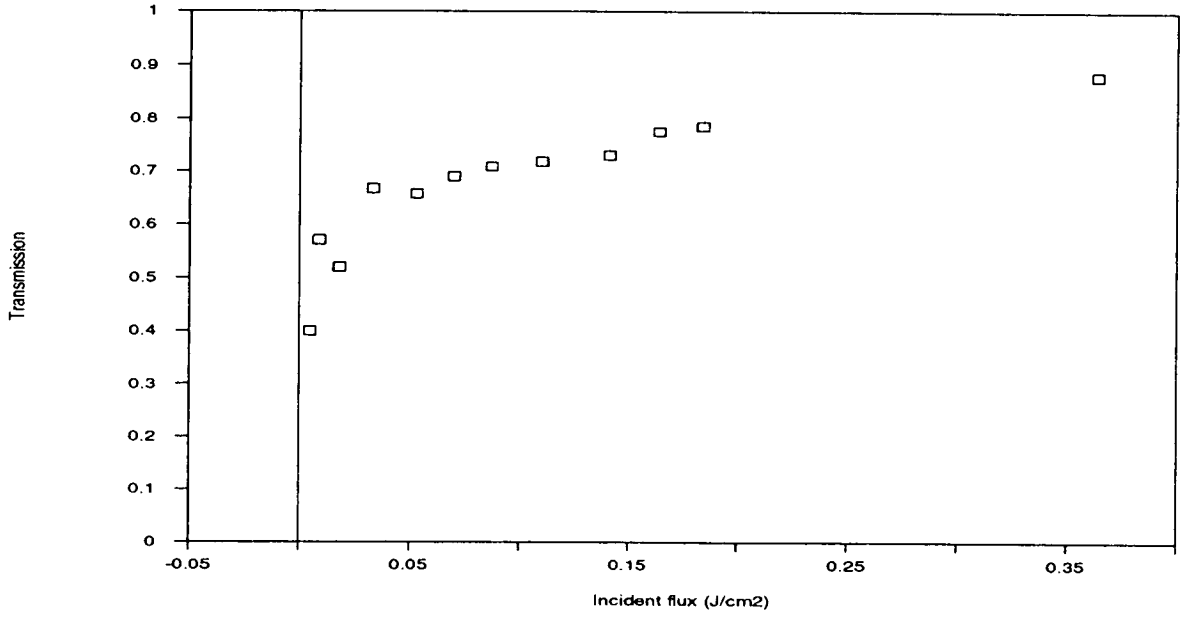

Figure 3.4.3 Saturation data for F_2^-:LiF with an unsaturated transmission of 27%.

3.5 *PRM Q-switched Operation at 1.32 μm.*

PTM Q-switching at 1.32 μm was performed with the basic normal-mode resonator described in Section 2.4. The only changes to the resonator were to add the $LiNbO_3$ Q-switch (see Section 3.1) as close to the 45-cm radius-of-curvature, high-reflector as was possible and to add a 45° turning-mirror between the laser rods and the output coupler. The resonator schematic

is shown in figure 4.4.1. The Q-switch position was at the lowest fluence point of the resonator to reduce the probability of optical damage. The 45°-mirror was highly-reflecting at 1.32 μm and highly-transmitting at 1.064 μm in preparation for the intracavity sum-frequency generation described in Section 4.3. The only polarization control elements required were the Brewster-faces of the laser rods, because the 1.32 μm transition in Nd:YAG has relatively low-gain.

Figures 3.5.1 through 3.5.3 show lower pulse energies and longer pulse durations than for the 1.064 μm laser transition, as expected for the reduced gain cross-section. The shortest duration pulses were slightly below 30 ns and had energies of approxiamtely 5 mJ.

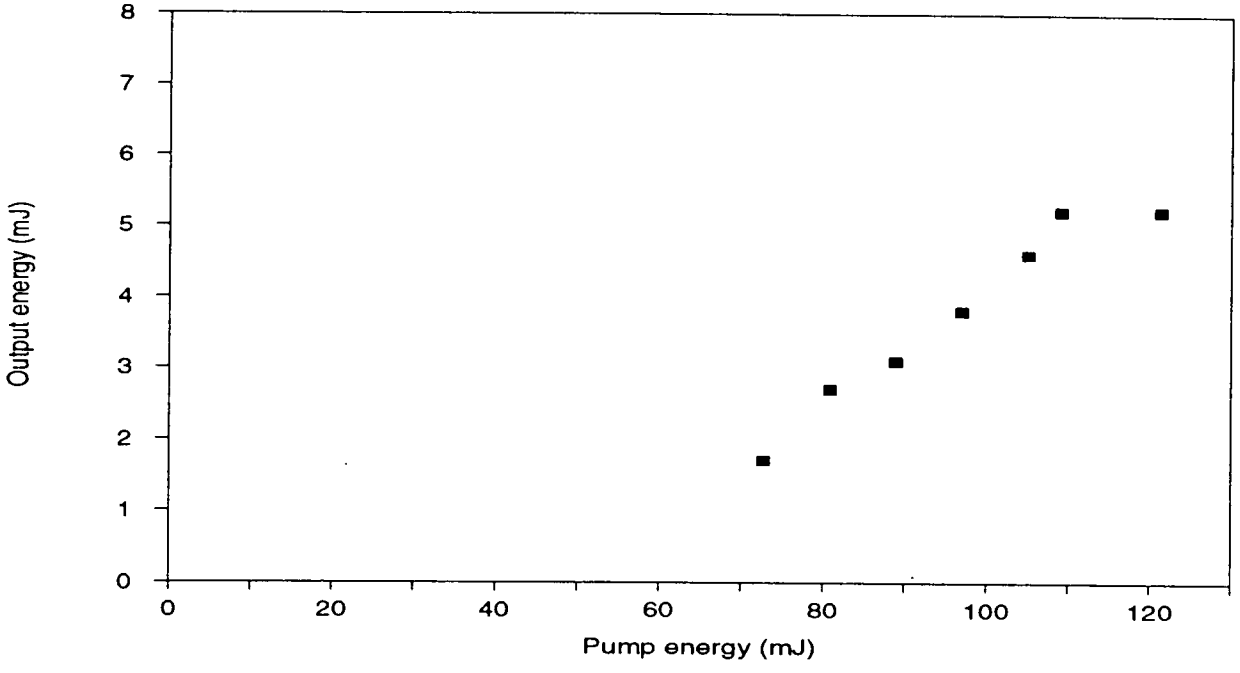

Figure 3.5.1 PRM Q-switched, 1.32-μm laser output data.

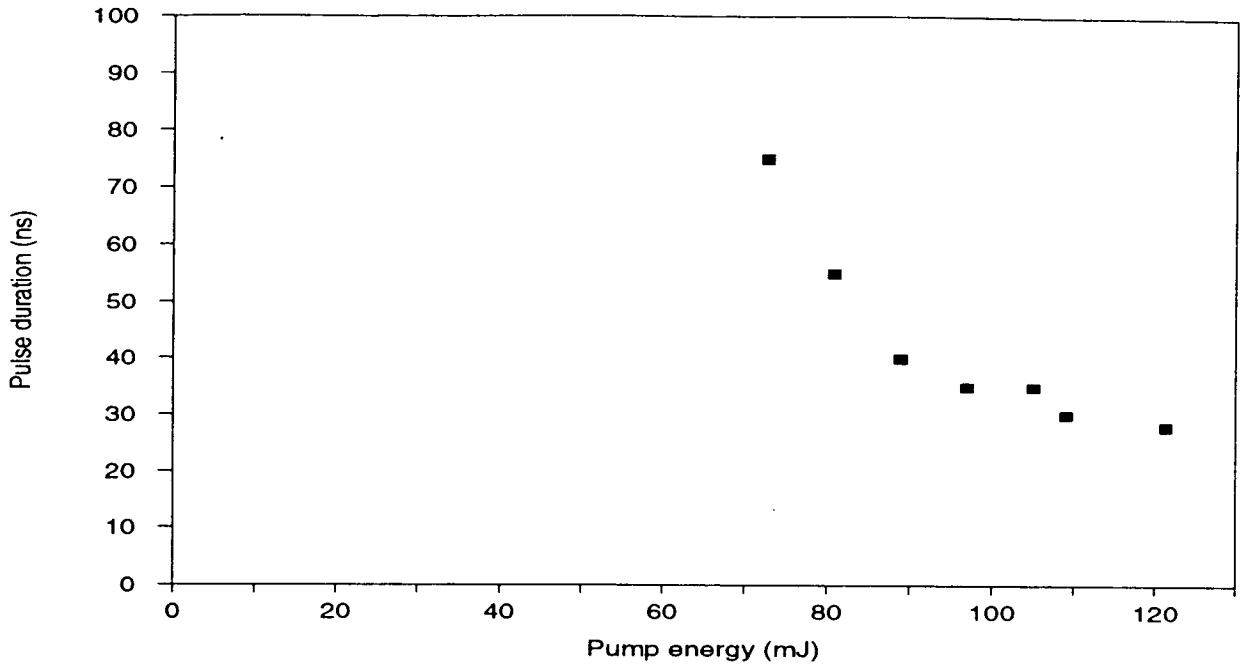

Figure 3.5.2 PRM Q-switched, 1.32-μm laser pulse duration data.

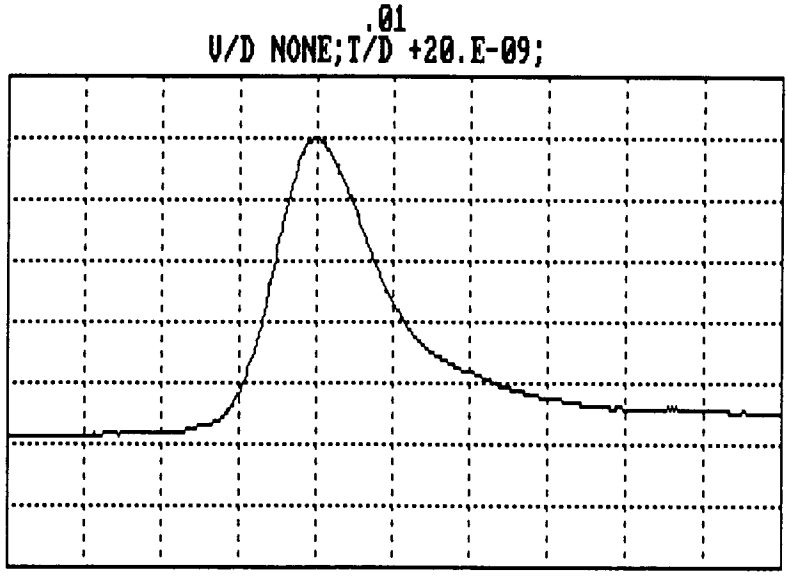

Figure 3.5.3 Typical PRM Q-switched, 1.32-μm laser pulse. (20 ns/div).

4 Second Harmonic and Sum-Frequency Generation.

Nonlinear frequency conversion has always been an attractive technique to extend the wavelength coverage of laser sources. Relatively new nonlinear crystals for the near-infrared and visible, such as lithium triborate (LBO), β-barium borate (BBO), rubidium titanyl arsenate (RTA), potassium titanyl arsenate (KTA), and potassium titanyl-phosphate (KTP) generally have larger nonlinear coefficients, lower absorption losses, and higher damage thresholds, when compared to lithium iodate ($LiIO_3$), lithium niobate ($LiNbO_3$), and potasssium dihydrogen phosphide (KDP) and its' isomorphs.

One of the most widely used, of these newer materials, is KTP. Although specific characteristics of other materials are often better, KTP has a combination of properties that make it unique for second-order nonlinear-optical applications. In the case of sum-frequency generation its large nonlinear coefficients, wide acceptance angle and unusually large temperature bandwidth are particularly advantageous.

In the Phase II proposal KTP was identified as our material of choice for both frequency doubling and summing of 1.064-μm and 1.32-μm radiations. However, a more recent review of the literature has indicated that BBO and LBO may be better suited to doubling 1.064 μm. Given this information and the emergence of RTA and KTA, our experimental investigation concentrated on KTP, but also included other materials whenever they were available.

4.1 *Phase Matching Calculations*

We calculated phase matching angles and other parameters for the nonlinear processes using the equations found in references [16 and 17] and the data given in references [19 through 22]. Tables 4.1.1 through 4.1.3 list the relevent parameters for doubling of 1.064 μm, doubling of 1.32 μm, and summing of 1.064 μm with 1.32 μm, respectively. Tables 4.1.1 and 4.1.2 contain parameters for all the materials investigated, including KTP. Table 4.1.3 only considers KTP and gives information for different orientations.

When doubling 1.064-μm radiation, both LBO and KTP have large angular acceptances and figures-of-merit. In addition LBO can be noncritically phase-matching (at 152°C) with a large walk-off angle, that allows efficient conversion with tightly focussed beams.

The optimum orientation for sum generation of 0.589-μm radiation in KTP is Type II phase matching with $\theta=77°$. The acceptance angle and figure-of-merit for this orientation is larger and the walkoff-angle is smaller than for the other orientations.

Table 4.1.1 Nonlinear crystal parameters for doubling of 1.064-μm radiation.

Crystal	Orientation	φ (degrees)	θ (degrees)	δθ (mrad-cm)	FOM($x10^{24}$) (pm^2V^{-2})
KTP [18]	Type II	0	63	8.5	1.8
$LiIO_3$ [19]	Type I	45	30	0.67	4.7
LBO [20]	Type II	0	90 @152°C	8.5	0.4
CD*A [21]	Type I	45	82	3.4	0.1

Table 4.1.2 Nonlinear crystal parameters for doubling of 1.32-μm radiation.

Crystal	Orientation	φ (degrees)	θ (degrees)	δθ (mrad-cm)	FOM($x10^{24}$) (pm^2V^{-2})
KTP	Type II	0	58	1.5	7.5
RTA [22]	Type II	0	64		
KTA [22]	Type II	0	63	0.4	12.0

Table 4.1.3 KTP parameters for summing of 1.064-μm and 1.32-μm radiation.

Orientation	θ (degrees)	Walkoff-angle (mrad)	δθ (mrad-cm)	FOM ($x10^{24}$) (pm^2V^{-2})
Type I φ=45°	39	46	0.6	0.1
Type II φ=0°	77	23	2.8	9.7
Type II φ=90°	64	64	1.8	5.4

4.2 *Second Harmonic Conversion of 1.064 μm to 0.532 μm.*

Work [20], based on an ideal laser and optimized nonlinear crystal lengths, has compared the conversion of 1.064 μm to 0.532 μm in several crystals. The laser was assumed to be diffraction-limited with a peak power of 5 MW (100 mJ in a 20 ns pulse) and fluence of 10 Jcm^{-2}. The calculated conversion efficiencies were 91% for 44-mm of CD*A (Type I), 96% for 28-mm of KTP (Type II), and 88% for 29-mm of LBO (Type II).

The highest doubling efficiency reported to date, using a single crystal geometry, for a 1.064-μm Nd:YAG laser was 80% [23]. This was achieved with a 7-mm long KTP crystal at an incident fluence of 2.5 Jcm^{-2} from a Q-switched laser. We have demonstrated doubling efficiencies of 56% for LBO (15 mm) and 42% for CD*A (25 mm) at incident fluences of 0.56 Jcm^{-2}.

The PTM Q-switched Nd:YAG laser described in Section 3.3 was used for the doubling experiments. At the time of this work, optical damage to the laser rods limited the pulse energy to 2.5 mJ. Typical pulse durations were 5 ns. Tight focussing was used to increase the incident fluence, whenever the angular acceptance of the nonlinear crystal allowed. The experimental arrangement is shown in figure 4.2.1.

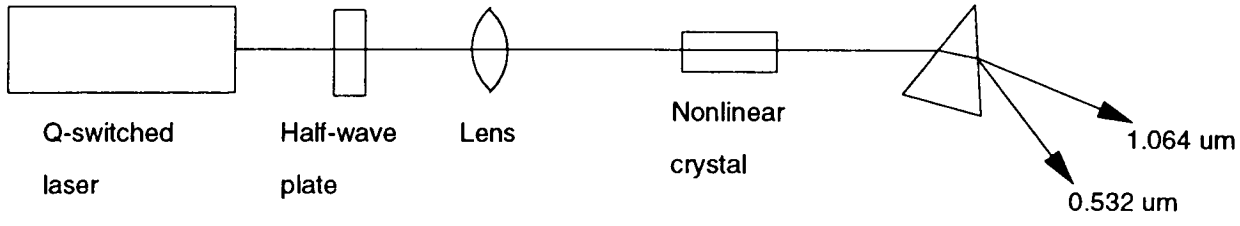

Figure 4.2.1. Experimental arrangement for extracavity frequency doubling.

In general, for efficient freuquency doubling the divergence of the focussed beam incident on the nonlinear crystal must be less than the angular phase-matching bandwidth. One can show, using the ABCD matrix formalism, that the focussed beam divergence in the near field is equal to ω_o/f, where ω_o is the radius at the TEM_{00} beam waist in the resonator and f is the lens focal length. The refractive index, n, of the nonlinear crystal reduces the effective beam divergence by a factor of n.

In order to maximize the doubling efficiency, we adjusted the distance between the lens and the nonlinear crystal, thereby varying the incident fluence. Figure 4.2.2 shows the second-harmonic pulse energy as a function of incident fluence. The maximum doubling

efficiencies achieved in LBO and CD*A were 56% and 42%, respectively. Saturation of the second-harmonic pulse energy indicates the onset of significant pump depletion. No data were available for KTP as our crystal was cut for 1.32 μm and had insufficient clear aperture to allow angle tuning for 1.064 μm. Properly-cut KTP would be expected to double with an efficiency greater than 50% [20 and 23].

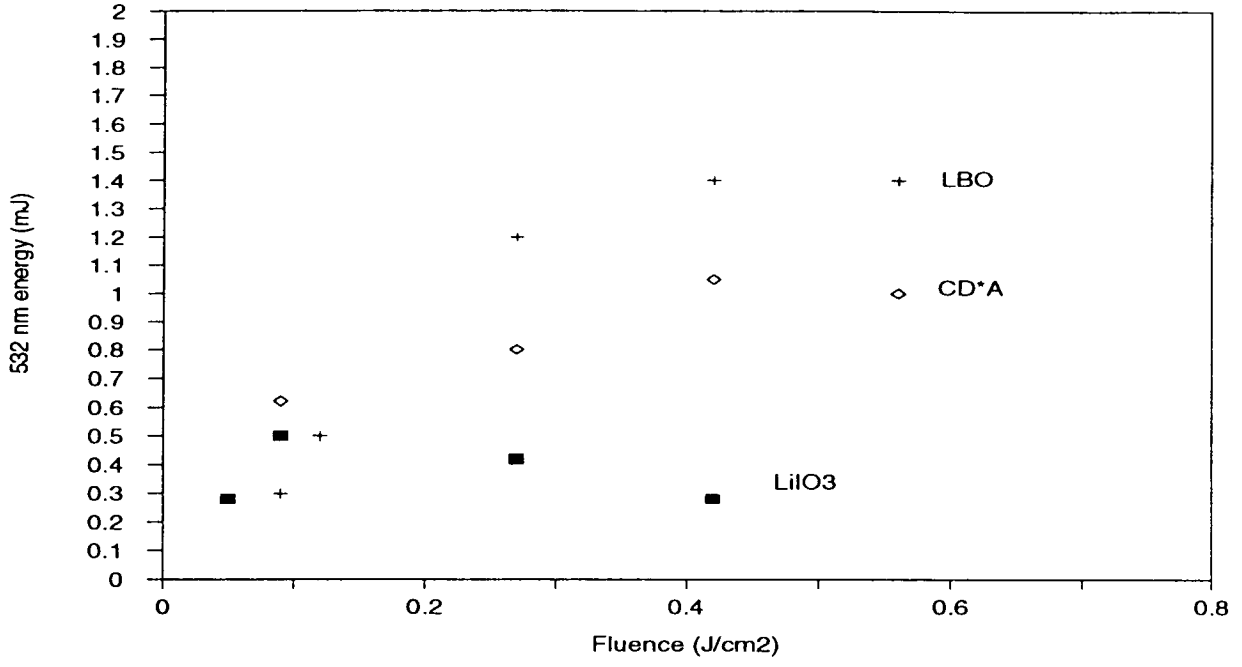

Figure 4.2.2 Second harmonic generation data for 1.064 μm.

4.3 *Second Harmonic Conversion of 1.32 μm to 0.660 μm.*

We investigated second harmonic generation in KTP, RTA, and KTA using the PRM Q-switched, 1.32 μm Nd:YAG laser described in Section 3.5. An experimental geometry similar to that decribed in Section 4.2 was employed. We used a 3x3x5 mm KTP crystal and 4.5x4.0x7.25 mm RTA and KTA crystals, all cut for Type II phase matching. The crystal orienations were $\theta = 60°$, 64° and 63° for KTP, RTA, and KTA, respectively. Only the KTP crystal was anti-reflection coated.

The small beam waist (350-um radius) of the TEM_{00}-mode located at output mirror provided sufficient fluence (1.3 Jcm^{-2}) without the use of a focussing lens. The crystals were located 2-cm from the output mirror. This allowed us to compare materials without being limited by their angular acceptances.

Figure 4.3.1 shows the second harmonic pulse energy as a function of the incident 1.32 μm fluence for RTA. The highest conversion efficiency of 10% (0.5 mJ output) was received with the RTA crystal, but required significant (18.5°) angle-tuning. Both the KTP and KTA crystals were cut correctly, but their conversion efficiencies were only 3%. The short crystal lengths and low incident fluences are responsible for the low conversion efficiencies. However, given the lack of antireflection coatings and short crystal length, 10% conversion for RTA demonstrates the potential of this new material.

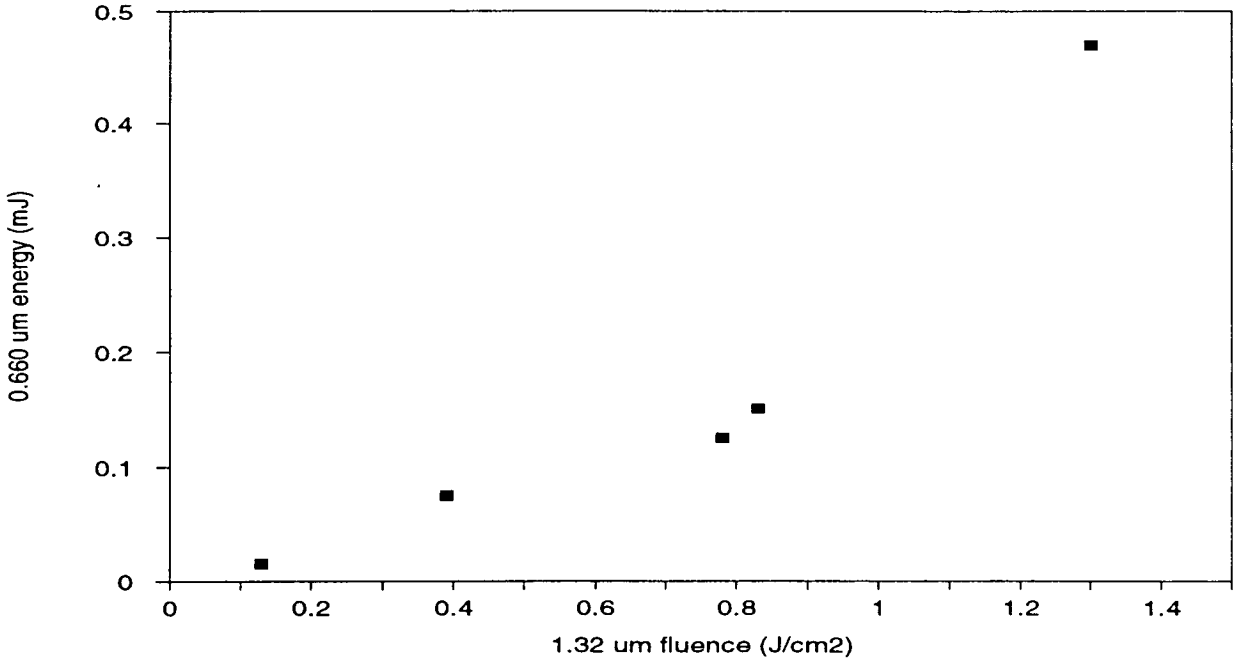

Figure 4.3.1 0.66 μm pulse energies as a function of incident 1.32 μm fluence for RTA.

4.4 *Sum-Frequency Generation of 1.064 μm and 1.32 μm to 0.589 μm.*

The Phase II proposal described an intracavity sum-frequency generation technique using a 1.32 μm ring laser containing a KTP crystal with 1.064 μm radiation injected from a PTM Q-switched laser. This concept was proposed to eliminate the timing jitter, that is present in extracavity sum-frequency generation using separate lasers.

Our attempt to implement this technique was abandoned after we damaged the KTP crystal during the fluence build-up stage, in the 1.32 μm laser, after the Q-switch opens and prior to sum-frequency generation with the injected 1.064 μm radiation. The ring resonator reflectors were all highly reflecting at 1.32 μm, which allowed the 1.32 μm fluence to exceed the damage

threshold of the KTP. In retrospect, we should have included a small out-coupling to control the fluence. It was our initial assumption that the optical components would survive long enough for the fluence to be reduced by the sum-frequency generation process and that high fluences would be benficial. At the time, we did not have sufficient funding or time left to purchase replacement optics to continue with the ring laser.

We eventually generated approximately 1.1 mJ of 0.589 μm radiation in a 10 to 15 ns pulse at 20 Hz with 11.5% conversion efficiency. This was achieved with the extracavity arrangement shown in figure 4.1.1. A pair of PRM Q-switched lasers the same as those described in Sections 3.2 and 3.2 were configured so the 1.064 μm radiation was injected into one arm of the 1.32 μm resonator. This arrangement allowed us to place the KTP crystal inside the resonator or outside.

Intracavity sum-frequency generation produced only several hundred microwatts of 0.589 μm radiation. The low gain of the 1.32 μm laser led to longer and lower energy pulses with the KTP crystal in the resonator and a reduction in the sum-frequency output.

The major limiting factors in extracavity conversion efficiency were the difference in the pulse durations of the two lasers and their relative timing jitter. Both Q-switches were triggered from the same clock, but with a relative time delay for synchronization. However, the build-up time jitter (estimated at 10 ns) made the sum-frequency output sufficiently unstable on a shot-to-shot basis as to lower our estimate of the pulse energies, because we were estimating the pulse energy from time-averaged power measurements with a thermo-pile power meter. In addition, the sum-frequency generation could only take place over the 10 to 15 ns duration of the 1.064 μm pulses and not fully utilize all the energy in the 25 ns 1.32 μm pulses. Given these limitations, the 1.1 mJ of 0.589 μm radiation generated with 11.5% conversion efficiency was a remarkable acheivement.

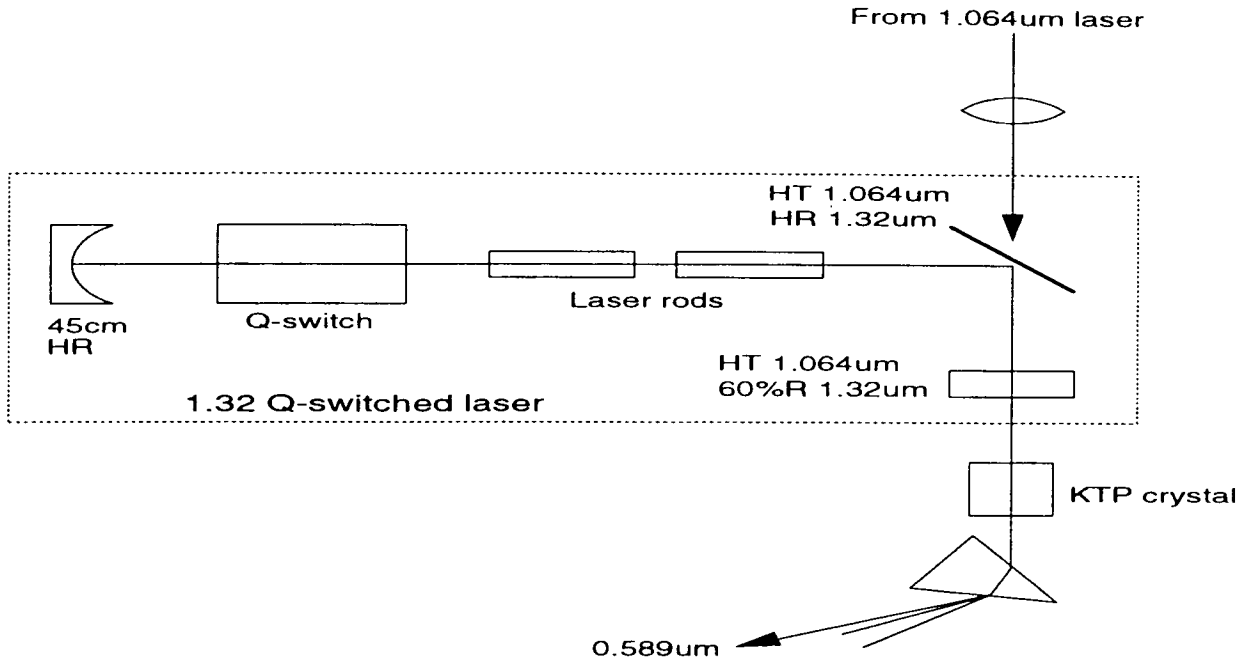

Figure 4.4.1 Experimental arrangement for sum-frequency generation.

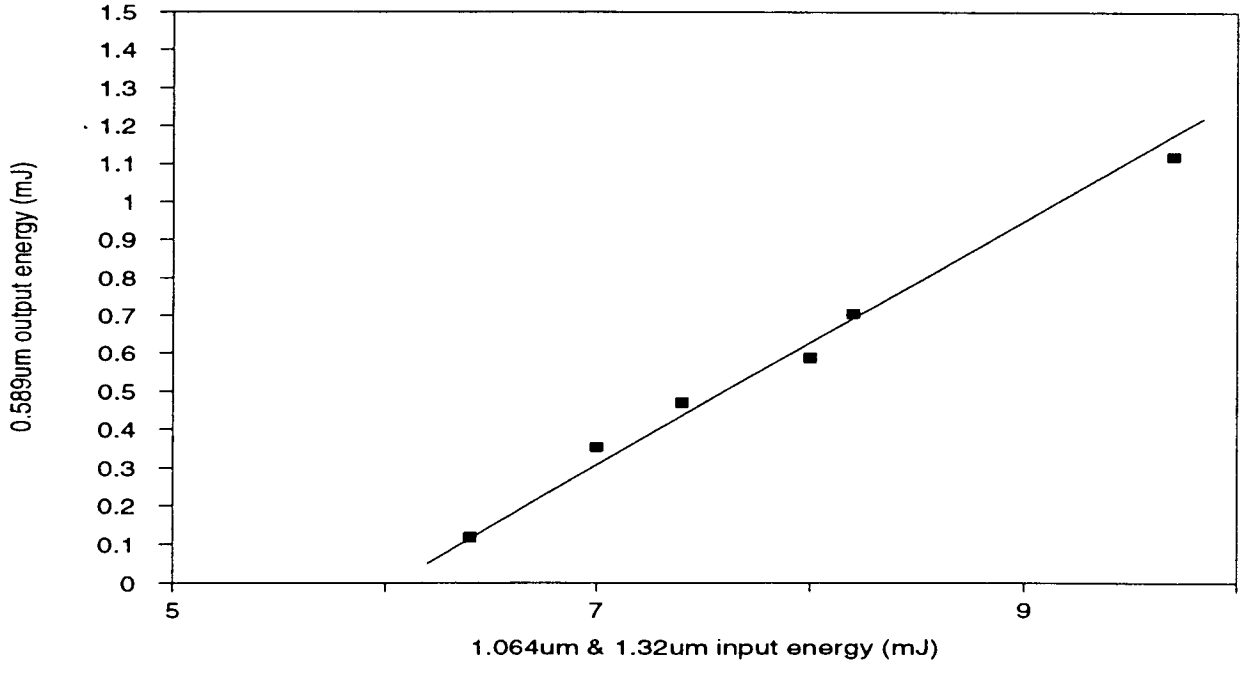

Figure 4.4.2 0.589-μm pulse energy as a function of the total 1.064-μm and 1.32-μm energy.

5 **Appendix 1:** *Amplifier Performance*

This appendix contains a summary of the performance of an amplifier experiment conducted at SEO, by Mr. D.B. Coyle of NASA GSFC, using a prototype amplifier of Mr Coyle's design with the PTM Q-switched laser described in Section 3.3 as the oscillator.

Report on the APS Amplifier Results from June 2 - 4, 1992

D. Barry Coyle
NASA-GSFC
Code 715, Photonics Branch
Greenbelt, MD 20771

The Alternating Precessive Slab (APS) Amplifier was shipped to Schwarz Electro-Optics where it arrived Monday, June 1. Work was begun Tuesday morning for its use with the Diode-Pumped Laser Altimeter being constructed on SBIR contract NAS5-30882. The laser altimeter, a Q-switched cavity-dumped oscillator, was operated at a 20 Hz repetition rate. The diode arrays were driven with 200 μs wide pulses at 51 Amps which yielded a maximum 1064 nm output of 1.7 mJ / 5 ns pulses.

Figure 1 shows the 32 cm long optical path within the APS crystal, 1.2 cm x 1.3 cm x 0.21 cm in dimension. The injected pulse uses 34 internal reflections and enters and exits the crystal at normal incidence. The amplifier is pumped with four 2-bar diode arrays from SDL. Each of the four arrays can emit up to 120 Watts of 810 nm pump light when driven at a peak current of 80 A. The complete amplifier mount was held to 27°C with water cooling.

The first area of concern was optical damage to the amplifier crystal due to thermal lensing, so the altimeter output pulse energy was lowered with various ND filters. The amplifier was placed as close to the output as possible to account for the divergent nature of the pulse. The injected beam diameter was measured to be about 1.5 mm near the amplifier crystal placement. This was less than the 2.1 mm thickness of the APS slab, so it seemed that diffractive losses could be avoided.

Figures 2 and 3 show the output profiles of the amplifier when the injected beam was centered on the APS input face. The square nature is probably due to diffractive effects within the slab. A single lobe could be achieved on the ouput by adjusting the input angle but it was not as energetic and only occurred when the injected beam was "walked" toward one of the corners of the APS input face. The best optical coupling, or insertion efficiency, that could be achieved without any beam forming optics was about 60%. This high passive loss was probably a combination of diffractive effects from the large beam width and the high number of internal reflections involved with the APS crystal design. The loss could be reduced by not using any index matching "glue" applied to the corner of the crystal opposite the entry face. Previous experiments showed that this method hindered some parasitic internal oscillations. The substance used for this purpose was a small drop of collodion.

Figure 4 and 5 shows a beam profile that was taken under different conditions. A 1 m focal length lens was placed in the injection beam. This produced a beam diameter of about 1.4 mm, which focused about 30 cm after the APS output face. The insertion efficiency was increased to about 73%. This was about the best that could be achieved

with index matching substance on the first corner of the APS crystal. There was not enough time to remove the collodion for tests with the positive lens.

The single-pass and double-pass gains peaked at only 1.45 and 1.54, respectively. If the insertion losses are ignored, these gains are 2.1 and 4.1. But for any practical application, the insertion loss subrtracts from the "real" performance of an amplifier. There was another factor, previously unknown, where the amplification peaked at around 70 A of diode array drive current. This was due to either/both the parasitic oscillations present in the slab, and the diode array temperature fluctuation during the pump pulse.

In conclusion, the overall performance of the APS amplifier was dissapointing in that there was an excessive amount of optical loss and parasitic oscillations. I would have liked to remove the collodian from the slab corner and repeat the amplification studies with the 1 m focal length lens, but time would not allow it. Apparently the application of the index matching substance was not having the desired effect in parasitic reduction, and in fact may have hindered the operation of the amplifier since much of the insertion loss of the injected beam was occuring at that very corner. Only after reviewing the data taken at SEO and that taken at NASA-Goddard, the APS design may be much better suited as a compact, diode pumped, solid state laser altimeter source than an amplifier. Further studies on this approach is planned sometime in the near future, as time allows. I will report on any results that look promising.

I would like to thank David Welford and Peter Moulton of Schwarz Electro-Optics for giving me the opportunity and the use of their equipment and lab space to study this amplifier in full, since I had been too busy with other projects prior to June.

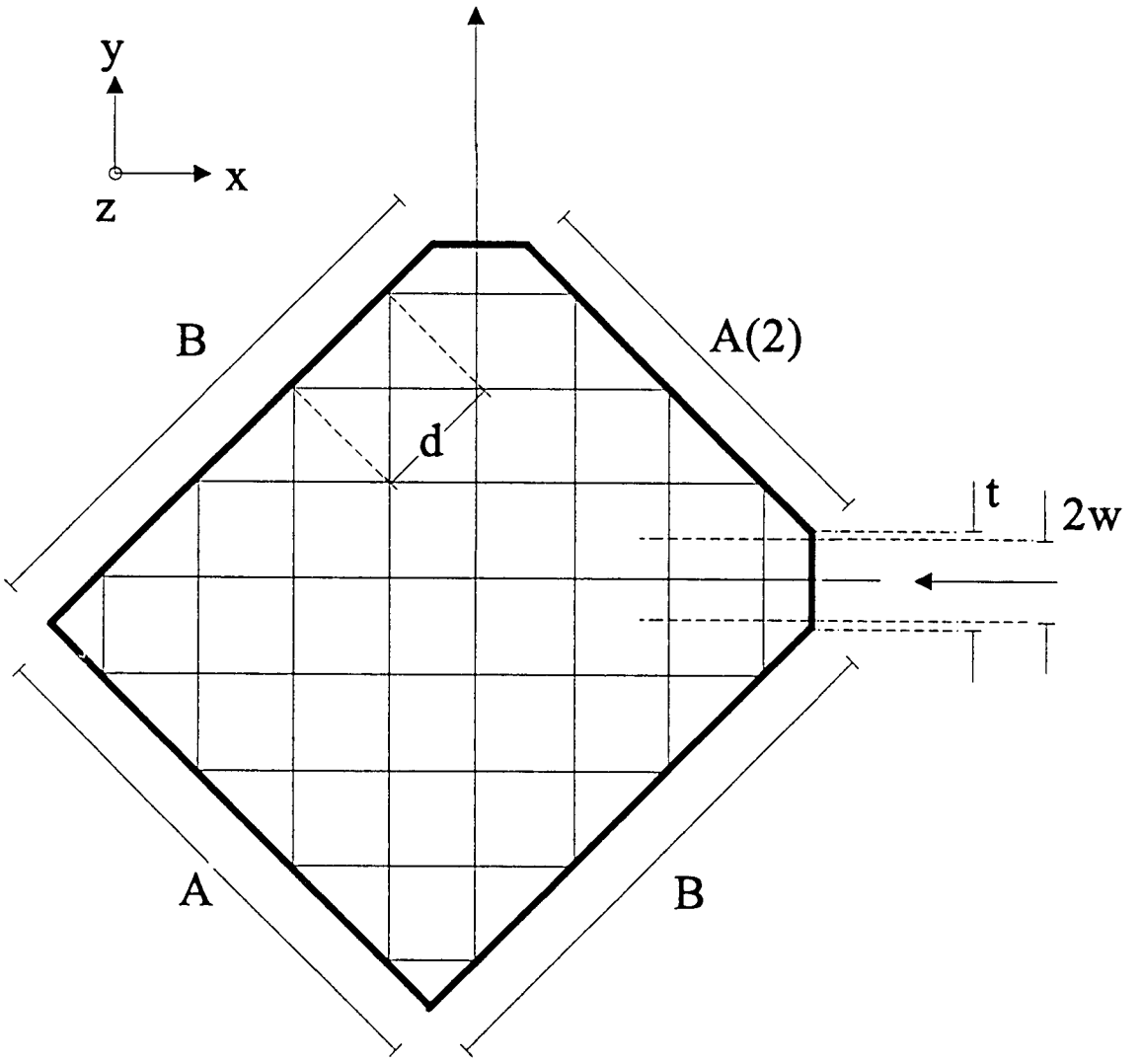

FIGURE 1. Optical path and design parameters for an N=8 APS amplifier.

1/e² of Energy Diameter Level

Total	86.47%	2681932
Peak		241
Peak Location	(104.00,	126.00)μm
Centroid	(117.46,	123.34)μm
Diameter		245.77μm

Frame number 1
6/ 4/92
56:08:96.11

Spiricon
LBA-100A V3.01

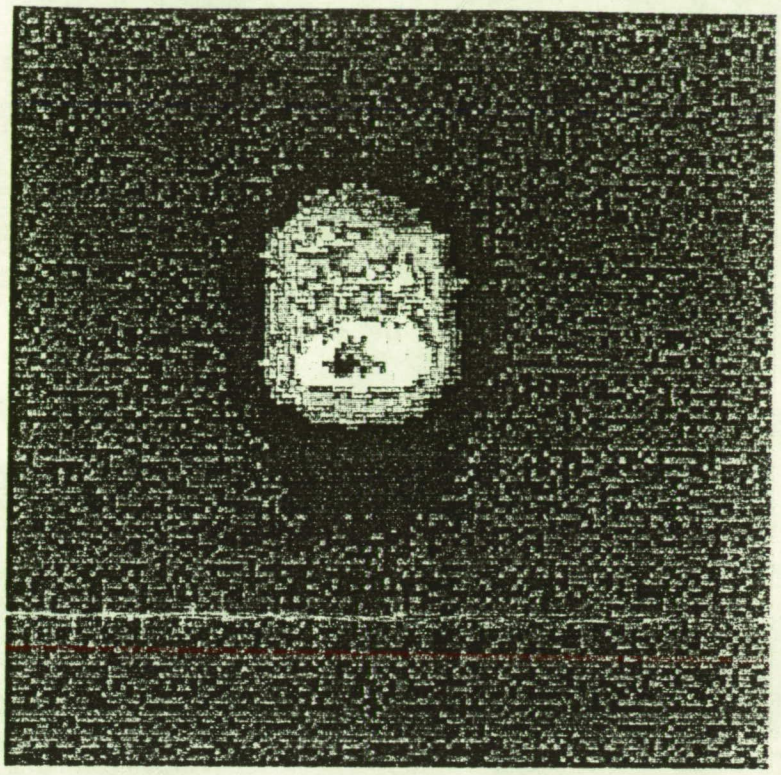

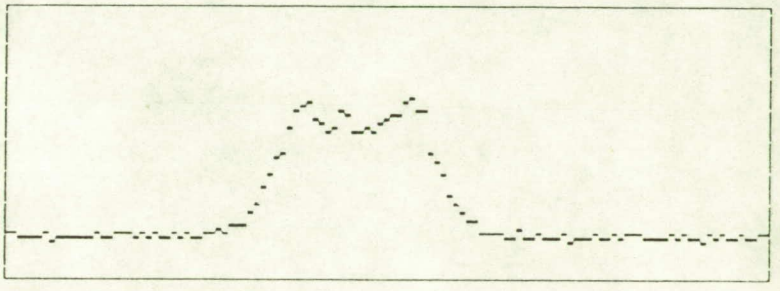

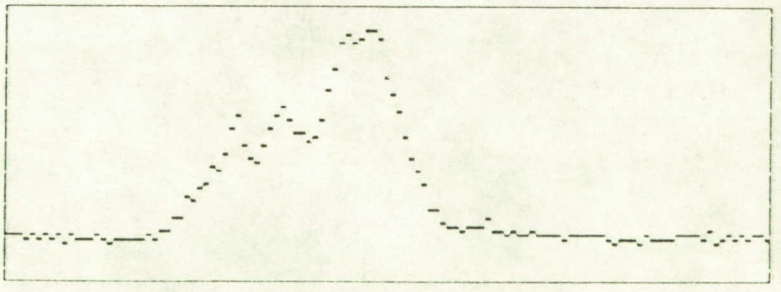

Figure 2. Contour plot of aperture-filled beam.

Frame number 1
6/ 4/92
56:08:96.11

Spiricon
LBA-100A V3.01

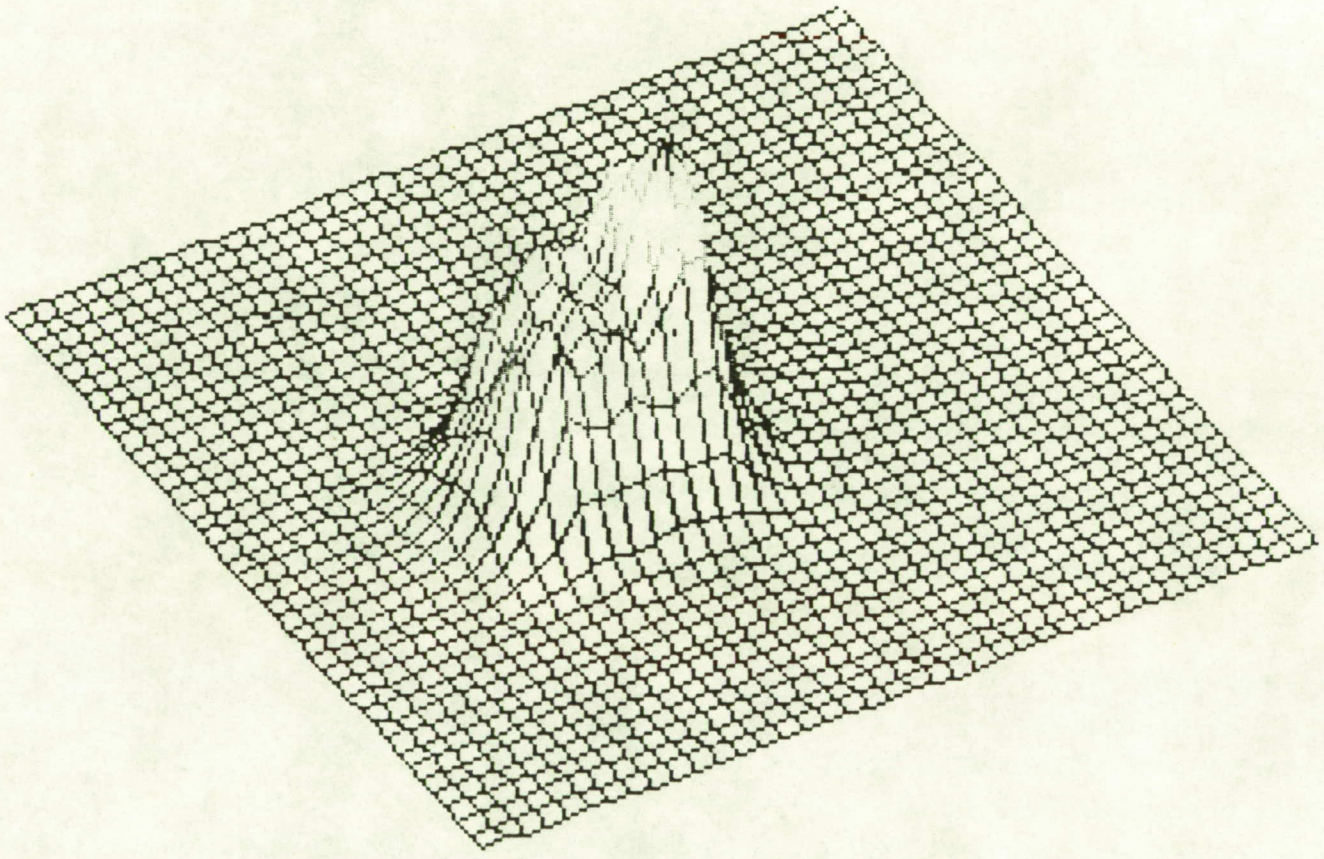

Figure 3. 3-D plot of aperture-filled beam.

1/e² of Energy Diameter Level
Total 86.47% 1393776
Peak 225
Peak Location (116.00, 120.00)μm
Centroid (119.98, 121.51)μm
Diameter 238.00μm

Frame number 1
6/ 4/92
7:30:49.10

Spiricon
LBA-100A V3.01

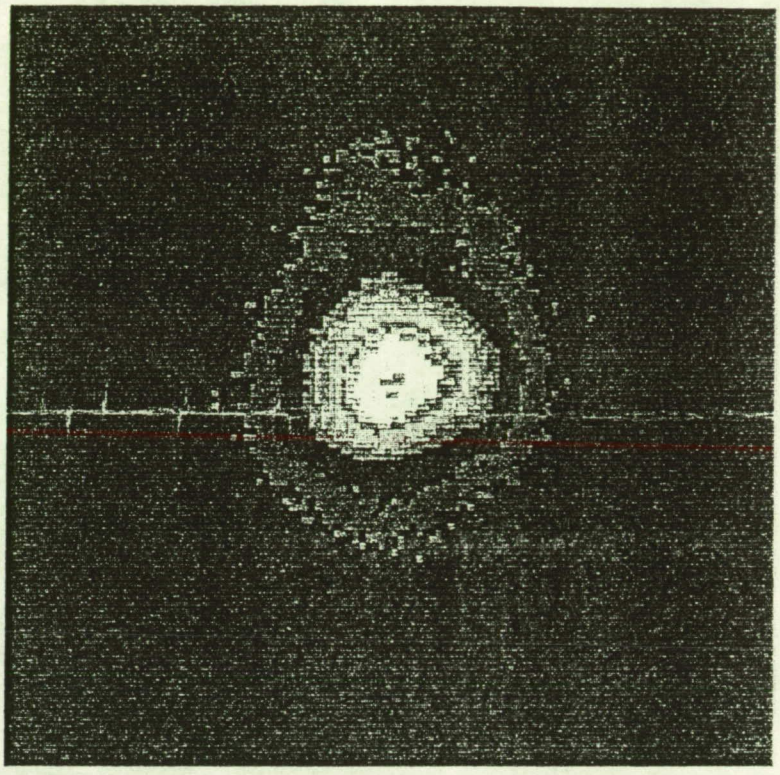

Horizontal Cursor Profile

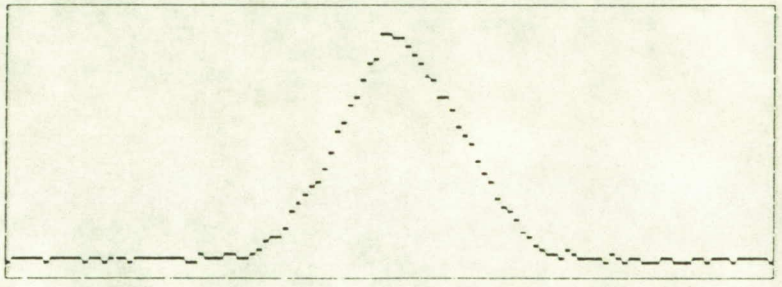

Vertical Cursor Profile

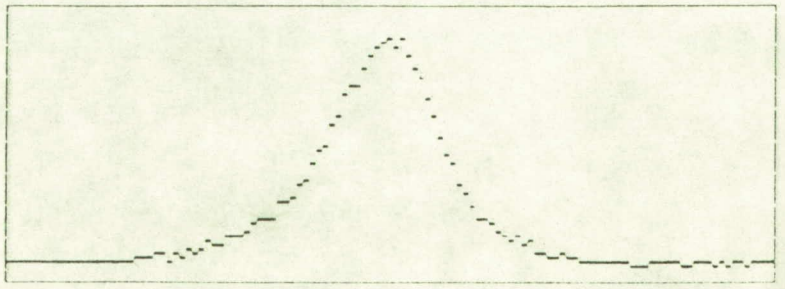

Figure 4. Contour plot of reduced beam.

6 **Appendix 2:** *Optical Damage Studies of Nd:YAG Laser Rods and Li:NbO_3 Q-switch Material.*

During Q-switched laser operation optical damage was observed on the surfaces of both Nd:YAG laser rods and the $LiNbO_3$ Q-switch. The damage was limited to the surfaces, with no bulk material damage occuring. As we were unable always quantify the damage thresholds during laser operation, we conducted a series of optical damage experiments.

The laser was arranged as a conventional PRM Q-switched laser generating 10-ns duration, 8.25 mJ pulses at a 50 Hz pulse-repetition-rate. The laser output was focused onto the material surface and the laser spot size estimated from the resonator beam parameters and the focussing geometry. Note, such estimation is accurate because the laser is operating in the TEM_{00}-mode.

The damage thresholds obtained are listed in Table A.2.1. Our definition of the optical damage threshold was the observation of permanent surface damage visible with the unaided eye. In these cases the damage threshold was also determined for exposure to multiple laser shots over periods of several seconds.

The damage thresholds obtained are within the range of values considered typical for these materials [24]. Yet, they are nearly an order-of-magnitude larger than the fluences at which the same components damaged in the Q-switched lasers. The reason for these differences remain unresolved given the time constraints of the Phase II effort.

Table A.2.1 Optical damage thresholds for Nd:YAG and $LiNbO_3$.

Material	Surface coating	Damage threshold (Jcm^{-2})
Nd:YAG	Low R	2.7
Nd:YAG	Low R	4.6
$LiNbO_3$	Uncoated	0.7
$LiNbO_3$	AR	3.3

7 **Appendix 3:** *Publications.*

Efficient TEM_{00}-mode operation of a laser-diode side-pumped Nd:YAG laser

D. Welford, D. M. Rines, and B. J. Dinerman

Schwartz Electro-Optics, Inc., 45 Winthrop Street, Concord, Massachusetts 01742

Received June 28, 1991

We report operation of a laser-diode side-pumped Nd:YAG laser with a novel pumping geometry that ensures efficient conversion of pump energy into the TEM_{00} mode. Of the 1064-nm output, 11.8 mJ of energy was obtained in a 200-μs pulse with 64 mJ of pump energy at 808 nm. The overall conversion and slope efficiencies were 18% and 23%, respectively.

Laser-diode-pumped, solid-state lasers with high TEM_{00}-mode conversion efficiencies have been demonstrated using both end-pumped[1-3] and side-pumped[4-7] geometries. However, these systems are not suitable for all applications. The end-pumped lasers typically operate at low average power because of the limited pump power that can be focused onto the end of the laser rod. The side-pumped systems, on the other hand, have no difficulty generating high powers using cw[6,7] or quasi-cw[4,5] pump sources. Their shortcoming is that the TEM_{00}-mode quality is obtained with pumping geometries optimized for high-average-power operation and that they require the use of either expensive, high-power cw[6,7] or several quasi-cw[4,5] laser-diode arrays (see below for a definition of what constitutes a laser-diode array). This renders these geometries difficult to implement as cost-effective, low-average-power systems.

Before proceeding, we define the differences between laser-diode bars and laser-diode arrays in the context of our pumping geometry and the previous research of others. A laser-diode bar is a single-device structure with laser emission over a rectangular area with a large aspect ratio. The emitting-region fill factor and sizes vary among device types, but the standard length is usually 1 cm and the height approximately 1 μm. These bars often have individual emitting regions that form a linear array. Yet, when we use the term laser-diode array, we are not referring to this microscopic structure but to a single, macroscopic, device package that consists of two or more of these 1 cm × 1 μm laser-diode bars stacked vertically on top of one another. Hence a five-bar stack of quasi-cw laser-diode bars is a five-bar, quasi-cw, laser-diode array. This type of device is considered to be a single laser-diode array irrespective of the number of bars in the stack.

In the case of pulsed systems, given the high cost of quasi-cw laser-diode arrays, side-pumped lasers operating at the energy level of tens of millijoules are cost effective only when pumped by as small a laser-diode array as possible. Previous research[8-11] with single laser-diode array pump sources (as much as five bars per array) in side-pumped geometries has been unable to demonstrate efficient operation in the TEM_{00} mode. We will describe a novel side-pumped geometry with efficient TEM_{00}-mode conversion using a single, five-bar, quasi-cw, laser-diode array as the pump source.

The major difference between our pumping geometry and that of previous side-pumped schemes is the achievement of a near-Gaussian pump deposition profile while using only a single laser-diode array as the pump source. Earlier side-pumping geometries fall into two broad categories. In the first category are those schemes that employ quasi-end-pumped geometries[7] or radially pumped geometries with spatial overlap/averaging of multiple pump sources[6] to achieve high TEM_{00}-mode conversion efficiency. The second category includes those schemes that employ a single laser-diode-array pump source and operate multimode.[8-11] Our research utilizes a pumping geometry whose geometry falls in the second category while achieving TEM_{00}-mode conversion efficiencies more typical of the first category.

Our laser rod is a 12-mm-long, semicircular-cross-section (D-shaped) piece of 1% Nd-doped YAG. The curved surface is antireflection coated at the pump wavelength and has a 1.5-mm radius of curvature. This surface of the rod acts as a cylindrical lens to focus the highly divergent output from the diode array, which is placed parallel to the rod axis facing the curved surface. Unabsorbed pump light is reflected from the highly reflecting, flat, rear surface. The path length of this double pass is approximately one absorption length of the material and leads to 65% absorption of the incident pump energy. The rod also has Brewster-angled end faces oriented such that the electric field axis is parallel to the flat, rear surface.

This rod is designed to perform the following specific functions: (1) The cylindrical lens action transforms the highly divergent diode array output into a Gaussian absorbed energy profile in the vertical direction. (2) The double pass of the pump beam over a total path equal to one absorption length provides a uniform absorbed energy profile in

0146-9592/91/231850-03$5.00/0

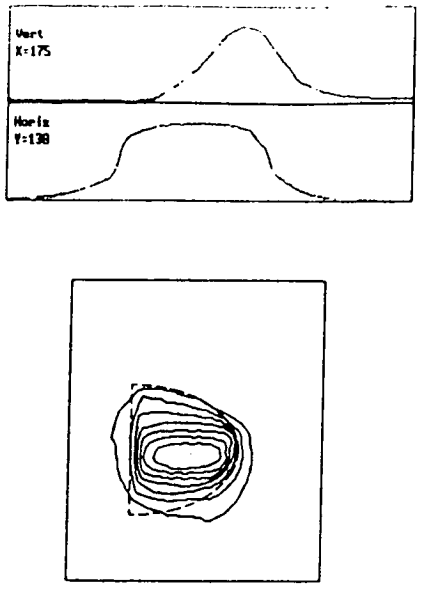

Fig. 1. Fluorescence image of the laser rod with absorbed energy profiles parallel (horizontal) and perpendicular (vertical) to the flat rear surface of the rod. The rod cross section is shown as the dotted curve that forms a semiellipse.

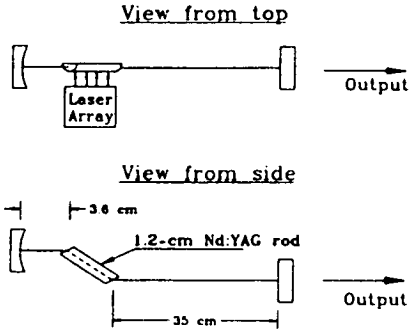

Fig. 2. Schematic layout of the laser resonator.

the horizontal direction. A shorter path would significantly reduce the total absorbed energy, and a longer path would significantly reduce the mean inverted population density. (3) The use of Brewster end faces on the rod expands the TEM_{00} cavity mode in the vertical direction to match the pumped volume in the rod. (4) The rod acts as the TEM_{00}-mode aperture for the resonator. (5) The flat rear face provides a mounting and heat-sinking surface.

Before conducting laser experiments, we evaluated the absorbed energy profile in the laser rod by imaging the fluorescence from the center of the array-pumped rod onto a CCD detector array interfaced to a frame grabber and computer (Montana Laser Corporation Multicam System). The fluorescence image was observed from a point beyond the Brewster end faces and represents the excited-state density as seen by the resonator outside the laser rod. The fluorescence image intensity is directly proportional to the excited-state density of Nd ions, and hence absorbed energy, in the laser rod.

The data shown in Fig. 1 were taken with the five-bar laser-diode array spaced 0.5 mm from the nearest point on the curved surface of the rod. This spacing gives the optimum energy conversion for TEM_{00}-mode laser operation as determined experimentally. Data taken for array-to-rod spacings of as much as 2 mm show that the pumped volume becomes more diffuse as the spacing increases. The laser-diode array used was a Spectra Diode Laboratories SDL3230 quasi-cw device composed of five 1-cm-long laser-diode bars stacked vertically with a 0.3-mm center-to-center spacing.

The fluorescence image shows that the excited-state density in the horizontal direction is almost uniform over most of the rod aperture, while in the vertical direction a close approximation to a Gaussian is obtained. A suitable resonator design for efficient energy conversion to the TEM_{00} mode must maximize the overlap integral of the resonator TEM_{00} mode and the pump profile while simultaneously utilizing the rod to apodize higher-order spatial modes.

We chose to use a plano-concave resonator (see Fig. 2) with a flat high reflector placed 3.6 cm from one Brewster end face of the laser rod and a 50-cm-radius output coupler placed 35 cm from the other Brewster end face. The calculated TEM_{00}-mode diameter ($1/e^2$ diameter of the intensity profile) at the laser rod was approximately 1 mm (1 mm × 1.8 mm inside owing the Brewster orientation). This resonator design suffers less than 1% loss for the TEM_{00} mode while preventing laser oscillation of higher-order modes, and it provides good overlap with the pump profile.

Long-pulse (200 μs at 50 Hz) laser operation was investigated with output-coupling transmission in the range of 2% to 25%. Optimum energy conversion was obtained with a 20% output coupler with 11.8 mJ of output at 1064 nm for 64 mJ from the 808-nm pump laser (approximately 65% was absorbed in the laser rod). Total intracavity losses were estimated to be 1.2% from a Findlay–Clay analysis of the laser threshold as a function of output coupler transmission. Figure 3 shows the output energy as a function of the pump energy incident upon the laser rod with a 20% transmission output coupler. The TEM_{00}-mode slope efficiency of 23% is comparable with that obtained by the majority of side-pumped geometries operating multimode, using a single quasi-cw laser-diode array,[7-9] and it far exceeds their potential TEM_{00}-mode performance.

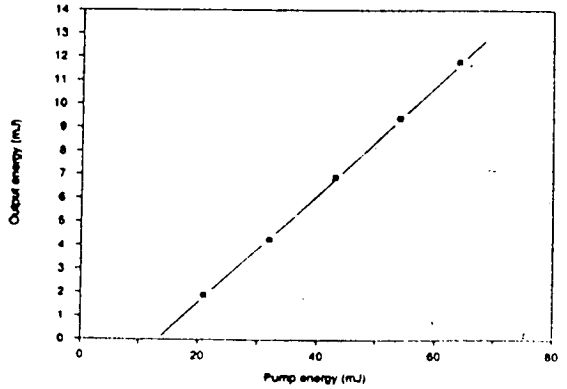

Fig. 3. TEM_{00}-mode energy as a function of the incident pump energy.

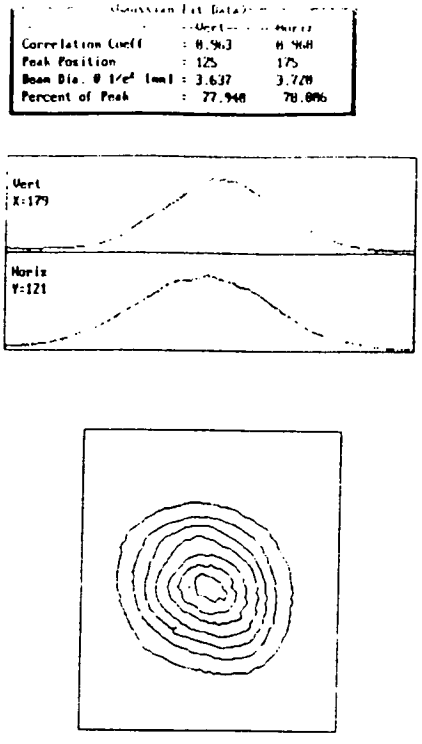

Fig. 4. Contour plot and beam profiles for the TEM_{00}-mode output beam.

The output-beam profile (with 64-mJ pump energy) in Fig. 4 shows a greater than 0.96 correlation with a least-squares fit to a Gaussian beam profile and less than 3% deviation from circular symmetry. The mean beam diameter of 3.7 mm approximately 1 m from the output coupler was larger than expected from resonator calculations. We therefore measured the beam divergence with the aid of a 1-m focal-length lens and obtained a 3.4-mrad divergence. We then probed the pumped laser rod with a He–Ne laser (632.8 nm) and determined the presence of a thermally induced lens of 3.4-m focal length. Inclusion of such a lens in our resonator calculations yielded a 3.1-mrad beam divergence. This is in good agreement with the experimental value of 3.4 mrad. Given that the heat load (0.6 W) on the laser rod is concentrated in a small volume of material with a near-radial deposition profile, a significant, thermally induced lensing effect is not unexpected, as shown by Innocenzi *et al.*[12]

In summary, we have demonstrated a 23% slope efficiency and 11.8 mJ of energy for a TEM_{00}-mode, Nd:YAG laser side pumped by a 64-mJ, five-bar, quasi-cw, laser-diode array using a novel pumping geometry. Higher output energies may be obtained by scaling the axial length of the system and adjusting the resonator mode size accordingly. This approach should allow efficient generation of TEM_{00}-mode-quality beams at energies of as much as several tens of millijoules.

This research was supported by the NASA Goddard Space Flight Center under Small Business Innovative Research program contract NAS5-30882.

References

1. T. Y. Fan, A. Sanchez, and W. E. DeFeo, Opt. Lett. **14**, 1057 (1989).
2. D. C. Shannon and R. W. Wallace, Opt. Lett. **16**, 318 (1991).
3. S. C. Tidwell, J. F. Seamans, C. E. Hamilton, C. H. Muller, and D. D. Lowenthal, Opt. Lett. **16**, 584 (1991).
4. R. L. Burnham, in *Digest of Conference on Lasers and Electro-Optics* (Optical Society of America, Washington, D.C., 1990), paper CMF3.
5. R. L. Burnham, Opt. Photon. News **1**(8), 5 (1990).
6. R. L. Burnham and A. D. Hays, Opt. Lett. **14**, 27 (1989).
7. T. M. Baer, D. F. Head, and P. Gooding, in *Advanced Solid-State Lasers*, Vol. 6 of OSA Proceedings Series, H. P. Jenssen and G. Dubé, eds. (Optical Society of America, Washington, D.C., 1991), p. 2.
8. F. Hanson and D. Haddock, Appl. Opt. **27**, 80 (1988).
9. F. Hanson, Opt. Lett. **14**, 674 (1989).
10. D. C. Gerstenberger, A. Drobshoft, and R. W. Wallace, Opt. Lett. **15**, 124 (1990).
11. T. H. Allik, W. W. Hovis, D. P. Caffey, and V. King, Opt. Lett. **14**, 116 (1989).
12. M. E. Innocenzi, H. T. Yura, C. L. Fincher, and R. A. Fields, Appl. Phys. Lett. **56**, 1831 (1990).

Observation of Enhanced Thermal Lensing Due to Near-Gaussian Pump Energy Deposition in a Laser-Diode Side-Pumped Nd:YAG Laser

David Welford, *Member, IEEE*, David M. Rines, *Member, IEEE*, Bradley J. Dinerman, and Robert Martinsen

Abstract—**We report operation of a laser-diode side-pumped Nd:YAG laser with a novel pumping geometry that ensures efficient conversion of pump energy into the TEM_{00} mode. Significant enhancement of thermally induced lensing due to the near-Gaussian energy deposition profile of the pump radiation was observed and is reported for the first time. An induced lens of approximately 3.2 m focal length was measured at average incident pump powers of only 3.2 W (corresponding to a 0.6 W heat load).**

Introduction

LASER-DIODE-PUMPED solid-state lasers with high TEM_{00}-mode conversion efficiencies have been demonstrated using both end-pumped [1]–[3] and side-pumped [4]–[7] geometries. However, these systems are not suitable for all applications. The end-pumped lasers typically operate at low average power because of the limited pump power that can be focused onto the end of the laser rod. The side-pumped systems, on the other hand, have no difficulty generating high powers using CW [6], [7] or quasi-CW [4], [5] pump sources. Their shortcoming is that the TEM_{00}-mode quality is obtained with pumping geometries optimized for high-average power operation and require the use of either expensive, high-power CW [6], [7] or several quasi-CW [4], [5] laser-diode arrays. This renders these geometries difficult to implement as cost effective low-average power systems.

In the case of pulsed systems, given the high cost of quasi-CW laser-diode arrays, side-pumped lasers operating at the tens of millijoule level are cost effective only when pumped by as small a laser-diode array as possible. Previous work [8]–[11] with single laser-diode array pump sources (up to 5 bars per array) in side-pumped geometries has been unable to demonstrate efficient operation in the TEM_{00}-mode.

The subject of this paper is a novel side-pumped geometry [12] with efficient TEM_{00}-mode conversion using a single 5-bar quasi-CW laser-diode array pump source and the thermal lens properties resulting from this geometry. The noteworthy feature of our present paper is the intentional use of near-Gaussian pump energy deposition profile to efficiently extract energy in the TEM_{00} mode of operation even in the presence of the associated thermal lens, because the spherical nature of the lens does not degrade the TEM_{00}-mode profile other than to change its diameter. It should also be noted that the nonuniform pump deposition profile provides the dominant driving term for the thermal diffusion process and thereby enhances the thermally induced lens.

Manuscript received July 22, 1991; revised October 14, 1991. This work was supported by the NASA Goddard Space Flight Center under the Small Business Innovative Research program under Contract NAS5-30882.

D. Welford, D. M. Rines, and B. J. Dinerman are with Schwartz Electro-Optics Inc., Concord, MA 01742.

R. Martinsen is with Lightwave Atmospherics, Marblehead, MA 01945.

IEEE Log Number 9106678.

TEM_{00} Laser Performance

In this paper, the laser rod was a 12 mm long, semicircular cross section (*D*-shaped) crystal of 1% Nd-doped YAG. The curved face was antireflection coated at the pump wavelength and had a 3 mm radius of curvature. This face of the rod acted as a cylindrical lens to focus the highly divergent output from the diode array, which was placed parallel to the rod axis facing the curved surface. Unabsorbed pump light was reflected from the highly reflecting, flat, rear surface. The path length of this double pass was approximately one absorption length of the material that leads to 65% absorption of the incident pump energy. The rod also had Brewster-angled end-faces oriented such that the electric field axis was parallel to the flat, rear surface. The flat, rear surface of the laser rod was mounted on a convection-cooled heatsink.

The laser-diode array used was a Spectra Diode Laboratories SDL3230 quasi-CW device composed of five 1 cm long laser-diode bars stacked vertically with 0.3 mm center-to-center spacing. The laser array was temperature tuned to operate at 808 nm center wavelength with a spectral width (FWHM) of approximately 3 nm.

Prior to conducting laser experiments, we evaluated the absorbed-energy profile (which corresponds to the deposited heat load) in the laser rod by imaging the fluorescence from the center of the array-pumped rod onto a CCD detector array, which was interfaced with a frame grabber

0018-9197/92$03.00

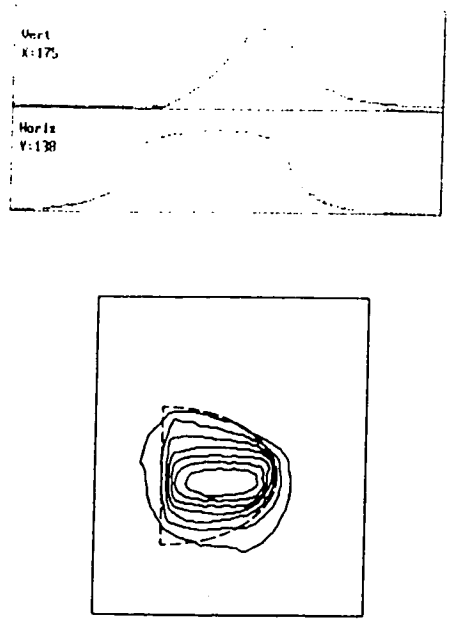

Fig. 1. Fluorescence image of the laser rod with absorbed energy profiles parallel (horizontal) and perpendicular (vertical) to the flat rear surface of the rod. The rod cross-section is shown as a dashed line forming a semi-ellipse.

and computer (Montana Laser Corp, Multicam System). As shown in Fig. 1, the excited-state density in the horizontal direction was nearly uniform over most of the rod aperture, while in the vertical direction a close approximation to a Gaussian distribution was obtained.

We chose to use a planoconcave resonator (Fig. 2) with a 50 cm radius-of-curvature, high-reflector placed 3.6 cm from one Brewster face of the laser rod and a flat, output coupler placed 35 cm from the other Brewster face. The calculated TEM_{00} mode diameter at the laser rod was approximately 1 mm (1 mm × 1.8 mm inside due to the Brewster orientation). This resonator design results in less than 1% loss for the TEM_{00} mode while preventing laser oscillation of higher-order modes and provides good overlap with the pump profile.

Long-pulse laser operation (200 μs at 50 Hz) was investigated with a 20% output coupler (eq. (3.59) of [13] predicts 19% as the optimum output-coupling). 11.8 mJ of 1064 nm output was obtained with 64 mJ from the pump laser. Fig. 3 shows the output energy as a function of the pump energy incident on the laser rod (approximately 65% of the pump energy was absorbed). The 23% slope efficiency was comparable to that obtained in multimode operation with earlier pump geometries [4], [5], and also far exceeds their potential TEM_{00} mode performance. Using the multimode resonator shown in Fig. 4 we obtained output energies of 20 mJ with a slope efficiency of 33%, which corresponds to 50% slope efficiency relative to the absorbed pump energy.

The output beam profile (at 64 mJ pump energy) shown in Fig. 5 shows greater than a 0.96 correlation with a least-

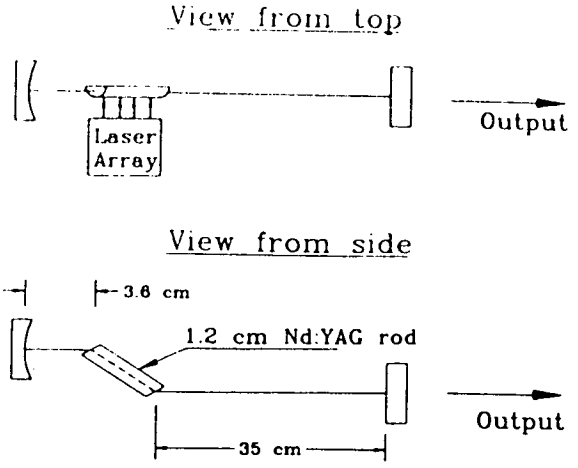

Fig. 2. Schematic layout to the TEM_{00} laser resonator.

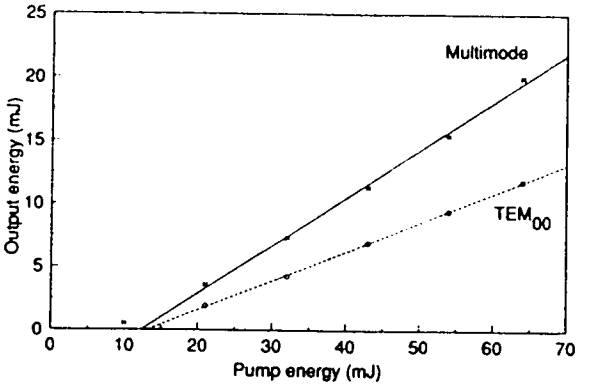

Fig. 3. Multimode and TEM_{00}-mode energies as a function of incident pump energy.

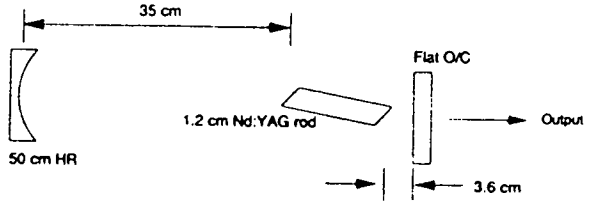

Fig. 4. Multimode laser resonator.

squares fit to a Gaussian beam profile and less than 3% deviation from circular symmetry. The mean beam diameter of 3.7 mm, approximately 1 m from the output coupler, was larger than expected from calculation of the "cold" resonator beam divergence. The presence of thermal lensing in the laser rod provides an explanation for the increased beam divergence.

Thermally Induced Lensing of the Laser Rod

We investigated the presence of thermally induced lensing in the laser rod using the optical probe technique shown in Fig. 6. A He-Ne laser operating at 632.8 nm probed the laser rod after passing through a 54.7 cm

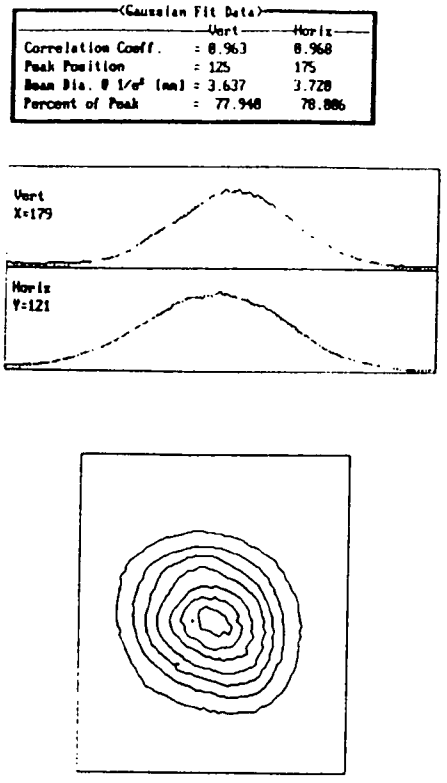

Fig. 5. Contour plot and beam profiles for the TEM_{00}-mode output beam.

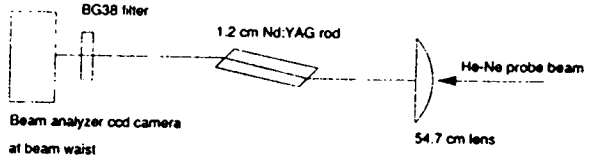

Fig. 6. Experimental arrangement for the thermally induced lens measurements.

planoconvex lens. The measurement technique was based on analyzing changes to the Gaussian beam waist as a result of the thermally induced lens in the pumped laser rod. The thermal lens focal length can be determined from eq. (67) of [14]. We used a beam profile analyzer (Spiricon Model LBA-100) to determine the position and diameter of the initial beam waist from the center of the unpumped laser rod and the diameters of the beam waists obtained at different pump-laser energies.

Fig. 7 shows the focal lengths of the thermally induced lens as a function of average pump power incident on the laser rod. The functional form was similar to the inverse-power dependence commonly seen in lamp-pumped, circular cross section rods in which a radial refractive index distribution (i.e., lens) is the result of a radial heat flow in the rod cooling system. Yet, the present system has a more complex heatflow pattern that is strongly influenced by both the nonuniform pump deposition and the asymmetric cooling geometry.

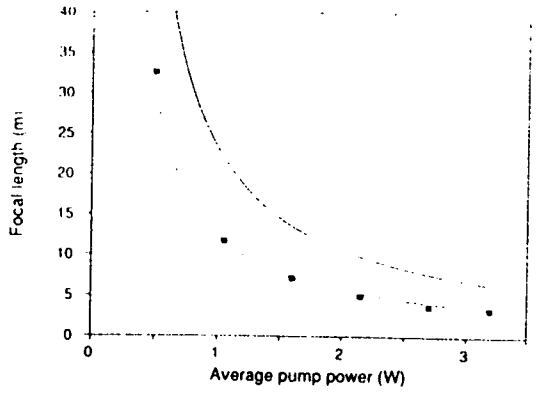

Fig. 7. Thermally induced lensing as a function of the average incident pump power. Solid line is the calculated lensing using eq. 13 of [7]. Dashed line is a least squares fit to the function $f = M/P$, where $M = 1.05 \times 10^3$ Wcm.

In addition to the thermally induced lensing, significant angular deflection of He-Ne laser probe beam was also observed. The magnitude of this beam deflection was as large as 0.3 mrad or approximately 0.1 mrad/W of incident pump power.

The thermal lens data represents the mean focal length, f, for the laser rod at each average pump power level P assuming ideal circular symmetry of the induced index profile. This assumption allowed us to operate the beam profile analyzer in a "real-time" mode and determine the beam waist position by observing the digital readout of the beam diameter ($1/e^2$ diameter of the peak). Even though the deposited energy profiles in the laser rod were not circularly symmetric the probe beam profiles showed no evidence of either strong asymmetry or the existence of separate beam waists (indicative of different lens focal lengths in the vertical and horizontal directions).

The work of Innocenzi *et al.* [15] treats thermal lensing in a laser rod with a Gaussian pump deposition profile and is similar to the more conventional radial diffusion analysis of uniformly pumped lamp-based systems [13], except that the rod area is replaced by the area of the pump deposition profile. This analysis [15] closely matches our pump geometry (but not our cooling geometry) and was used to generate the solid curve of Fig. 7 that is of the form $f = M/P$, where M is a constant equal to 1.96×10^3 W-cm. A least squares fit of the same functional form to the experimental data gave a value of 1.05×10^3 W-cm and is shown as the dashed line in Fig. 7.

The poor agreement of the analytical model [15] led us to numerically model the steady-state temperature distributions in the laser rod for different heat load distributions and boundary conditions. The modeling was performed using a finite-element software package (COSMOS/M, Structural Research and Analysis Corp.) designed for mechanical engineering and was therefore unable to directly predict the thermal lens parameters. However, we were able to interpret the temperature distributions obtained

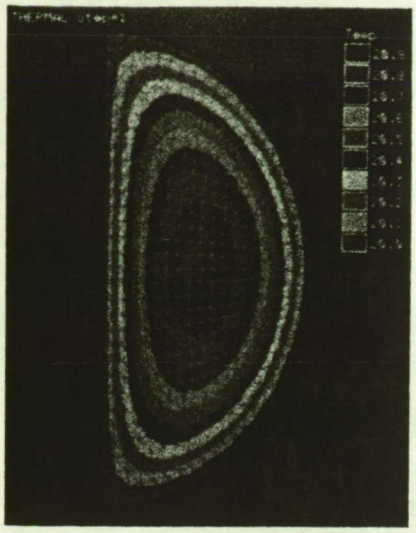

(a)

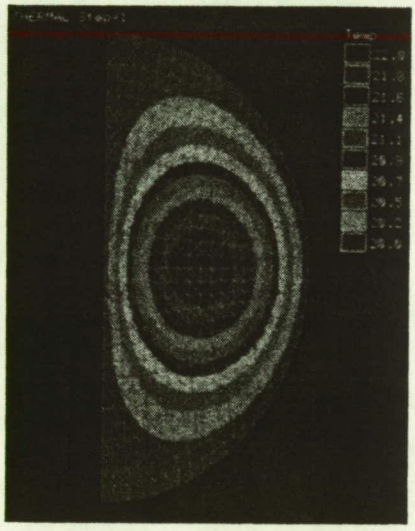

(b)

Fig. 8. Temperature profiles for laser rods with 20°C isothermal boundary conditions and 0.6 W heat load with (a) uniform heat deposition and (b) the near-Gaussian heat deposition corresponding to the actual pumping geometry.

from the modeling with the aid of the analytical model [15].

Fig. 8 shows two temperature distributions for 20°C isothermal boundary conditions and 0.6 W total heat loading. The first case, Fig. 8(a), has a uniform heat load distribution and is equivalent to conventional lamp pumped laser rods (except for the semicircular rod cross-section). The temperature distribution is almost elliptical in profile and could be optically described as a spherical lens with an additional cylindrical lens. This is in contrast to the circular symmetry obtained in lamp pumped rods. The second case, Fig. 8(b), has the near-Gaussian heat load distribution of the diode-laser pumped system. The heat load was derived from the fluorescence image data shown in Fig. 1. The near-Gaussian heat load distribution generated a circularly symmetric temperature distribution with three times the peak temperature rise obtained with the uniform heat load distribution and hence the generation of a stronger thermal lens.

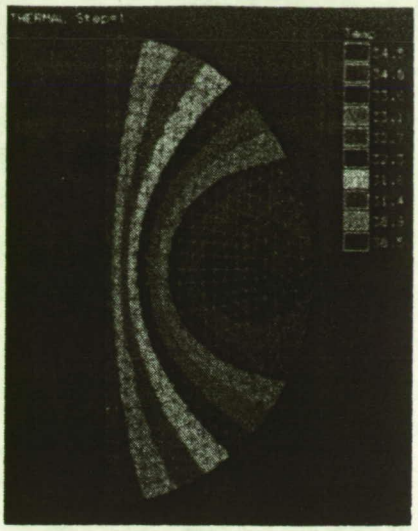

Fig. 9. Temperature profile for a laser rod with near-Gaussian deposition of 0.6 W heat load and experimentally measured boundary conditions of a 30.5°C isothermal on the flat heatsink surface and convection cooling of the curved face at an ambient air temperature of 23.8°C.

These two cases illustrate the effect of nonuniform pump deposition in the presence of isothermal boundary conditions. Yet, in our laser the curved surface of the rod was not isothermal since clear optical access must be maintained. Therefore, a third case was modeled, which simulated the laser rod boundary conditions more accurately with 30.5°C isothermal heatsinking at the flat surface and convection cooling to ambient air at 23.8° C over the curved surface. The resulting temperature distribution shown in Fig. 9 has a stronger thermal lens than for the isothermal boundary conditions [see Fig. 8(b)] and is decentered by approximately 0.5 mm. This decentering of the thermally induced lens leads to a beam deflection that we estimate to be 0.16 mrad for the measured focal length of 3.2 m, while the measured beam deflection was 0.3 mrad.

The analytical result obtained earlier by applying eq. (7) of [15] assumed isothermal boundary conditions, which in our numerical model underestimated the maximum temperature rise by a factor of two (2°C in Fig. 8(b) instead of 4°C in Fig. 9) compared to the real boundary conditions. Hence, the analytical estimate of the lens focal length is also underestimated by this factor of two. A suitable correction to the analytical model is to reduce the thermal lens coefficient from 1.96×10^3 W-cm to 0.98×10^3 W-cm, which is in close agreement with the value of 1.05×10^3 W-cm obtained from a least squares fit to the focal length data shown in Fig. 7.

The measured thermal-lens data was used in resonator calculations to determine the TEM_{00} mode beam diver-

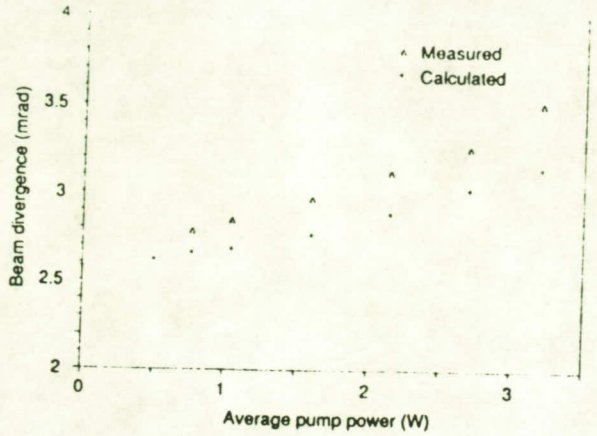

Fig. 10. Comparison of measured and calculated resonator beam divergences as a function of the average incident pump power.

gence. The beam divergence was estimated experimentally by focusing the beam with a 1 m focal length, plano-convex lens and by measuring the beam waist diameter (at $1/e^2$) with the Multicam System (described earlier). The calculated and measured beam-divergence data shown in Fig. 10 are in close agreement, thereby supporting the thermal lens data.

In addition, we also looked for evidence of thermal birefringence by adding an analyzing polarizer to our linearly polarized He–Ne laser-based probe arrangement. We saw no evidence of thermally or otherwise induced birefringence.

Summary

In summary, we have demonstrated 23% slope efficiency and 11.8 mJ output energy for a TEM_{00} mode, 1064 nm Nd:YAG laser side pumped by a 64 mJ, 5 bar stack of quasi-CW laser diode arrays using a novel pumping geometry. We have observed a 3.2 m thermally induced lens in the laser rod at 3.2 W of average pump power (0.6 W heat load). Computer modeling of the thermal diffusion process confirms that the thermally induced lensing is significantly enhanced due to the near-Gaussian pump deposition profile. This effect is somewhat unique to laser pumped solid state media and must be carefully considered when designing these lasers to operate efficiently in the TEM_{00} mode.

References

[1] T. Y. Fan, A. Sanchez, and W. E. DeFeo, "Scalable, end-pumped, diode-laser-pumped laser," *Opt. Lett*, vol. 14, pp. 1057–1059, 1989.

[2] D. C. Shannon and R. W. Wallace, "High-power Nd:YAG laser end pumped by a cw, 10 mm × 1 μm aperture, 10-W laser-diode bar," *Opt. Lett.*, vol. 16, pp. 318–320, 1991.

[3] S. C. Tidwell, J. F. Seamans, C. E. Hamilton, C. H. Muller, and D. D. Lowenthal, "Efficient, 15-W output power, diode-end-pumped Nd:YAG laser," *Opt. Lett.*, vol. 16, pp. 584–586, 1991.

[4] R. L. Burnham, "Recent advances in high power diode pumped solid state lasers," presented at CLEO '90, Anahiem, CA, 1990, paper CMF3.

[5] ——, "High-power transverse diode-pumped solid-state lasers," *Opt. and Photon. News*, vol. 1, pp. 4–8, 1990.

[6] R. L. Burnham and A. D. Hays, "High-power diode-pumped frequency-doubled cw Nd:YAG laser," *Opt. Lett.*, vol. 14, pp. 27–29, 1989.

[7] T. M. Baer, D. F. Head, and P. Gooding, "High-efficiency diode pumping of Nd:YLF and Nd:YAG using a laser-diode," in *OSA Proceedings on Advanced Solid-State Lasers*, H. P. Jensen and G. Dubé, Eds. Salt Lake City, UT: OSA, 1990, pp. 2–4.

[8] F. Hanson and D. Haddock, "Laser diode side pumping of neodymium laser rods," *Appl. Opt.*, vol. 27, pp. 80–83, 1988.

[9] F. Hanson, "Laser-diode side-pumped Nd:$YAlO_3$ laser at 1.08 and 1.34 μm," *Opt. Lett.*, vol. 14, pp. 674–676, 1989.

[10] D. C. Gerstenberger, A. Drobshoft, and R. W. Wallace, "High-peak-power operation of a diode-pumped Q-switched Nd:YAG laser," *Opt. Lett.*, vol. 15, pp. 124–126, 1990.

[11] T. H. Allik, W. W. Hovis, D. P. Caffey, and V. King, "Efficient-diode-array-pumped Nd:YAG and Nd:Lu:YAG lasers," *Opt. Lett.*, vol. 14, p. 116, 1989.

[12] D. Welford, D. M. Rines, and B. J. Dinerman, "Efficient TEM_{00}-mode operation of a laser-diode side-pumped Nd:YAG laser," *Opt. Lett.*, to be published.

[13] W. Koechner, *Solid-State Laser Engineering* New York: Springer-Verlag, 1976.

[14] H. Kogelnik and T. Li, "Laser beams and resonators," *Appl. Opt.*, vol. 5, pp. 1550–1567, 1966.

[15] M. E. Innocenzi, H. T. Yura, C. L. Fincher, and R. A. Fields, "Thermal modeling of continuous-wave end-pumped solid-state lasers," *Appl. Phys. Lett.*, vol. 56, pp. 1831–1833, 1990.

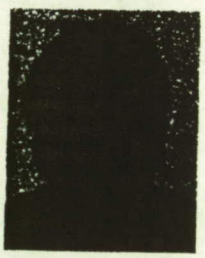

David Welford (S'79–M'80) was born in Whitby, North Yorkshire, England, on March 17, 1956. He received the B.Sc. degree in 1977, and the Ph.D. and D.I.C. degrees in 1980, all in physics, from the Imperial College of Science and Technology, University of London, England. His thesis research was on CW mode-locked dye lasers and their application in picosecond kinetics studies of organic molecules.

He was with the Massachusetts Institute of Technology, Lincoln Laboratory, Lexington, from 1980 to 1987, where he investigated the emission linewidth and modulation properties of semiconductor diode lasers and the application of diode lasers to optical communications. Since April 1987 he has been with Schwartz Electro-Optics Inc., Concord, MA. His primary research interests are tunable solid state laser materials and semiconductor diode pumped lasers.

Dr. Welford is a member of the Optical Society of America.

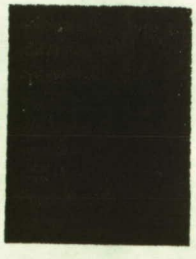

David M. Rines (A'88–M'91) was born in Rochester, NH, on July 19, 1966. He received the B.S. degrees in physics and mathematics from Gordon College, Wenham, MA, in 1988.

He was a summer staff member at Schwartz Electro-Optics Inc., Research Division, Concord, MA, in 1987 and became a full-time staff member in 1988. Since that time he has contributed to the development of both pulsed and CW solid-state lasers operating in the visible and near-infrared wavelength regions. Most recently he has been investigating a cadmium selenide optical parametric oscillator (OPO), pumped by a Q-switched erbium laser, as a tunable source in the 4 μm wavelength region.

Mr. Rines is a member of the Optical Society of America.

Bradley J. Dinerman was born in Salem, MA, on November 23, 1965. He received the B.A. degree in physics from Connecticut College, New London, in 1987 and the M.S. degree in physics from Boston College, MA, in 1991, where he is currently pursuing the Ph.D. degree in physics with a concentration in rare earth solid-state spectroscopy.

In 1990, he conducted his Master's degree research at NASA, Langley Research Center, Hampton, VA, on the spectroscopy and nature of energy transfer in Tm, Ho:YAG. In January 1991, he joined Schwartz Electro-Optics Inc., Research Division, Concord, MA, where he has since been investigating diode-pumped 2.8 μm laser systems.

Robert Martinsen was born in New York City, NY, on June 11, 1961. He received the B.S. degree in marine engineering from New York Maritime College in 1983, and the M.S. degree in mechanical and aerospace engineering from the University of Virginia, Charlottesville, in 1986.

He is currently pursuing Ph.D. research at the Massachusetts Institute of Technology, Cambridge, in optical remote sensing of oceanic wave spectra. Since 1983, he has been actively involved in the analysis and development of optical sensors for marine and aerospace applications. In March 1991, he founded Lightwave Atmospherics Inc. to investigate lidar remote sensing instruments for wind shear detection and pollution monitoring, and he has been working in cooperation with Schwartz Electro-Optics Inc., Research Division, to advance the performance of diode-pumped solid-state laser sources.

Mr. Martinsen is a member of the International Society for Optical Engineering (SPIE) and the Optical Society of America.

Presented at ASSL '93.

2.4-ns Pulse Generation in a Solid-State, Passively Q-Switched, Laser-Diode-Pumped Nd:YAG Laser

Y. Isyanova and D. Welford
Schwartz Electro-Optics Inc.
45 Winthrop Street
Concord, MA 01742
(508) 371-2299

Abstract

We report generation of 5-mJ, 2.4-ns Q-switched pulses from a single-frequency, TEM_{00}-mode, laser-diode-pumped Nd:YAG laser using F_2^- color centers in LiF.

Introduction

In the present work, we report the passive Q-switching of a laser-diode-pumped solid-state laser using a solid-state saturable absorber. Earlier work reported 12-ns duration, microjoule energy pulses [1] and 20-ns duration millijoule energy pulses [2]. Our work concentrated on the generation of much shorter (2.4 ns) pulses at millijoule energies for altimetry.

The saturable absorber material of choice for 1064-nm operation is LiF in which has been gamma-irradiated with a total dose of 5.5×10^8 rads. The active absorber site is the F_2^- color center [3]. The only addition to a conventional two-mirror linear resonator is the insertion of a window-like piece of AR-coated F_2^-:LiF material. The simplicity and small size of such a Q-switch is ideally suited for use in compact laser-diode-pumped laser designs. The use of a short resonator, high output coupling, and low unsaturated absorber transmission leads to short pulse generation and increased longitudinal mode selection.

In the past, F_2^- color centers have been observed to degrade rapidly [1,2,3]. The degradation is seen as an increase in saturated loss with a corresponding reduction in laser output energy. This is due to the presence of non-radiative F_3^- centers in the LiF crystal [3]. We have observed no drop in laser energy for $>10^7$ shots (138 hours) at 20 Hz operation, generating 5 mJ pulses of 2.4 ns duration.

Experimental Results

The resonator used in this work is shown in Figure 1. TEM_{00}-mode operation was obtained by the use of a novel side-pumping geometry, reported previously [4], that achieves near-Gaussian pump energy deposition in the laser rods. A pair of opposing Brewster-angled, 12-mm long, semicircular-cross-section (3-mm diameter) Nd:YAG laser rods were each side-pumped by a 5-bar stack of quasi-cw laser diodes (SDL 3230 devices). The resonator TEM_{00}-mode size matches that of the deposited energy in the laser rods, thereby ensuring efficient TEM_{00}-mode operation (see Figure 2).

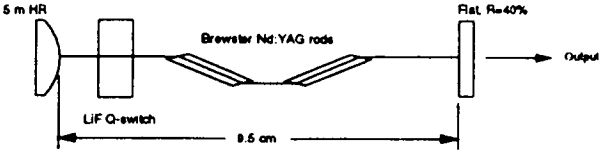

Figure 1. *Passively Q-switched laser resonator.*

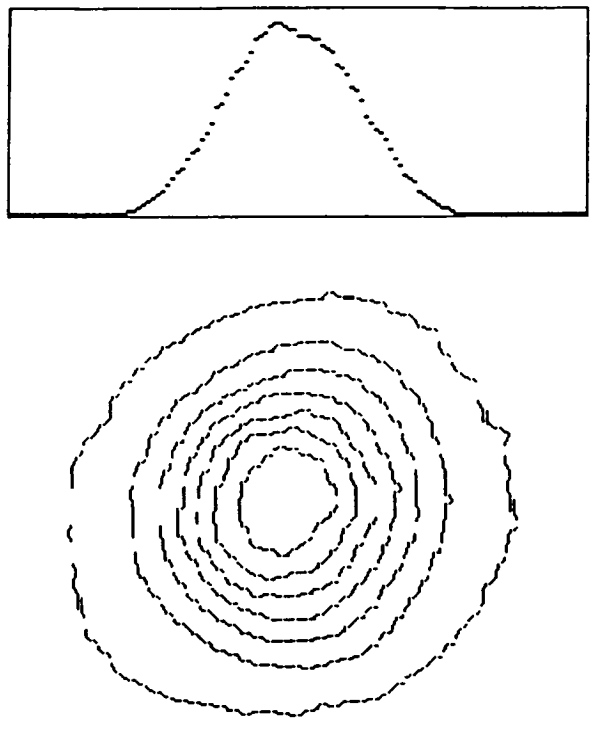

Figure 2. *TEM_{00}-mode beam profile.*

The laser was operated at a 20-Hz pulse repetition rate with 200-μs duration pump pulses. In normal-mode operation, the laser generated pulses at 19.5 mJ energy with 16% conversion efficiency and 22.6% slope efficiency. In Q-switched operation, 2.4-ns duration pulses were obtained at 5 mJ energies with 5.2% conversion efficiency. Figure 3 shows the output energy data.

Table 1 summarizes the Q-switched performance obtained using different length (from 6 mm to 30 mm) F_2^-:LiF crystals, which are characterized by their unsaturated single-pass transmissions, T_0. The diode-laser pump energy was equal to the threshold energy for single-pulse generation in each case. Further increasing the pump energy leads to multiple-pulse generation with the same energy in each pulse [2]. Note, that the data for the 12% transmission F_2^-:LiF material shows an improved pulse duration of 2 ns. However, the pulse energies were reduced to 4 mJ by the onset of damage to one of the Nd:YAG laser rods.

After replacing the damaged laser rod, we were able to generate 2.4-ns duration, 5 mJ pulses at a 20 Hz for $>10^7$ shots with no damage to laser rods or saturable absorber.

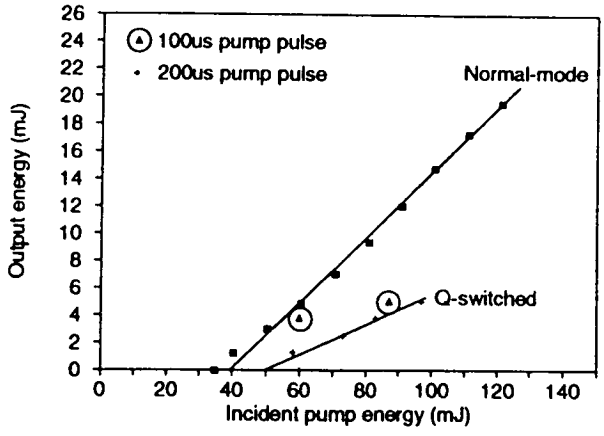

Figure 3. *Normal-mode and Q-switched output data.*

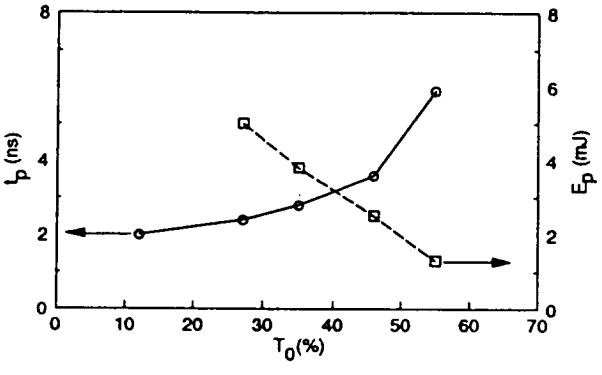

Figure 4. *Pulse energy, E_p, and pulse duration, t_p, as a function of unsaturated Q-switch transmission, T_0.*

Table 2 shows that shorter pump pulses improve the conversion efficiency in Q-switched operation. Pumping harder to reduce the build-up time reduces spontaneous emission losses from the excited level of the laser medium prior to energy extraction in the Q-switched pulse. Approximately 60% of the normal-mode energy could be extracted in a Q-switched pulse using 100-μs pump pulses. This represents an increase of 10% of the normal-mode energy extracted compared to the 200-μs pump pulse.

Table 1. *Passive Q-switched laser performance.*

T_0 (%)	E_{pump} (mJ)	E_p (mJ)	t_p (ns)
55	58	1.3	5.9
46	73	2.5	3.6
35	83	3.8	2.8
27	97	5.0	2.4
12	121	4.0	2.0

Table 2. *Q-switched energy extraction.*

T_0 (%)	E_{pump} (mJ)	t_{pump} (μs)	Normal-mode E_{out}(mJ)	Q-switched E_p(mJ)	NM to QSW Conversion (%)
35	83	200	8.2	3.8	46
35	60	100	6.5	3.8	58
27	97	200	10.2	5.0	49
27	87	116	8.3	5.0	60

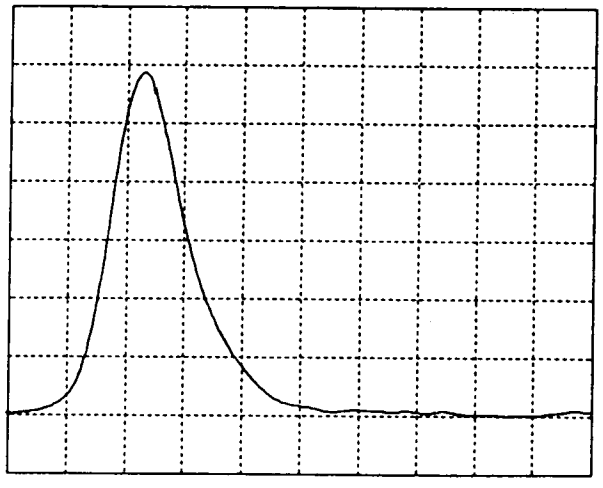

Figure 5. *2.4-ns duration Q-switched laser pulse. (2 ns/div timescale).*

A 2.4-ns duration pulse is shown in Figure 5. The lack of longitudinal mode-beating is a characteristic of single-frequency operation. This is a direct result of using the F_2^-:LiF material as our saturable absorber. The specific property of the solid-state saturable absorber (compared to dyes) which leads to better mode selectivity is the larger saturation fluence (typically a factor of 20). This leads to a longer pulse build-up time in the Q-switched laser. During the longer build-up time the difference in gain between adjacent longitudinal modes will produce a difference in build-up time between modes. Hence, the highest gain mode will Q-switch first and extract all the stored energy. *If the difference in build-up times, Δt_s, between adjacent modes is longer than the Q-switched pulse duration, t_p, the laser pulse will contain a single longitudinal mode.* This constitutes a temporal criterion for single-frequency Q-switched laser operation.

$$\Delta t_s > t_p$$

We have derived an expression for Δt_s [5]:

$$\Delta t_s = \frac{G t_l (1+k)}{2k^2 \sigma_n l_a N_{th}} \left(\frac{\sigma_n - \sigma_m}{\sigma_n} \right)$$

The reader is referred to [5] for a complete description of the parameters and their typical values. Estimates of Δt_s from this expression are plotted in Figure 6 with measured pulse durations for each sample

of saturable absorber tested. Δt_s is always greater than tp and the laser was observed to be single-frequency as confirmed by the absence of mode-beating in the temporal pulse profile.

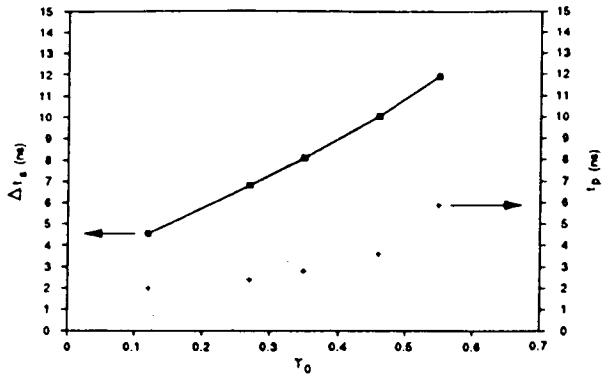

Figure 6. *Pulse build-up time difference, Δt_s, and pulse duration, t_p, as a function of unsaturated Q-switch transmission, T_0.*

Summary

In summary, we have demonstrated an all solid-state passively Q-switched laser that generates 5-mJ, 2.4-ns, single-frequency pulses with a TEM_{00} beam profile. The major advantages for this approach compared to electro-optic Q-switch technology are the elimination of drive electronics and simplified resonator configurations. This technology is ideally suited to space-based and commercial applications. Greater than 10^7 shots have been demonstrated at 20 Hz with no noticable performance degradation.

Acknowledgments

The authors wish to acknowledge the support of NASA Goddard Space Flight Center under Small Business Innovative Research program contract #NAS5-30882.

References

[1] J.A. Morris and C.R. Pollock, "Passive Q switching of a diode-pumped Nd:YAG laser with a saturable absorber," Optics Letts., **15**, 440, 1990.

[2] R. Beach, J. Davin, S. Mitchell, W. Benett, B. Freitas, and R. Solarz, "Passively Q-switched transverse-diode-pumped Nd^{3+}:YLF laser oscillator," Optics Letts., **17**, 124, 1992.

[3] Y. Isyanova, A.L. Levit, B.D. Lobanov, N.T. Maksimova, V.M. Ovchinnikov, Y.A. Pirogov, B.A. Simin, and P.A. Tsirulnik, "New developments in solid-state lasers," Bulletin of the Academy of Sciences of the USSR, Physical Science Series, **48**, 97, 1984.

[4] D. Welford, D.M. Rines, and B.J. Dinerman, "Efficient TEM_{00}-mode operation of a laser-diode side-pumped Nd:YAG laser," Optics, Letts., **23**, 1850, 1991.

[5] Y. Isyanova and D. Welford, "A Temporal Criterion for Single-Frequency Operation of Passively Q-switched Lasers," to be submitted to Optics Letters.

8 Technical References

[1] R. Beach, D. Mundinger, W. Benett, V. Sperry, B. Comaskey, and R. Solarz, "High-reliability silicon microchannel submount for high average power laser diode arrays," Appl. Phys. Letts., **56**, 2065, 1990.

[2] H. Kogelnik and T. Li, "Laser beams and resonators," Appl. Opt., **5**, 1550, 1966.

[3] M.E. Innocenzi, H.T. Yura, C.L. Fincher, and R.A. Fields, "Thermal modeling of continuous-wave end-pumped solid-state lasers," Appl. Phys. Lett., **56**, 1831, 1990.

[4] W. Koechner, "Thermal lensing," pp.388-393, in "Solid-State Laser Engineering," third edition, published by Springer-Verlag, New York, 1992.

[5] Equation (8), p666, A.E. Siegman, "Lasers," first edition, published by University Science Books, Mill Valley , CA 94941, 1986.

[6] T. M. Baer, D. F. Head, and P. Gooding, "High-efficiency diode pumping of Nd:YLF and Nd:YAG using a laser-diode bar," in the OSA Proceedings on Advanced Solid-State Lasers, H. P. Jensen and G. Dube, ed., (OSA , Salt Lake City, Utah., 1990).

[7] F. Hanson and D. Haddock, "Laser diode side pumping of Neodymium laser rods," Appl. Optics, **27**, 80, 1988.

[8] F. Hanson, "Laser-diode side-pumped Nd:$YAlO_3$ laser at 1.08 and 1.34 μm," Opt. Lett., **14**, 674, 1989.

[9] R.P. Hilberg and W.R. Hook, "Transient elastooptic effects and Q-switching performance in lithium niobate and KD*P Pockels cells," Appl. Optics, **9**, 1939, 1970.

[10] X.D. Wang, P. Basseras, R.J.D. Miller, J. Sweetser, and I.A. Walmsley, "Regenerative pulse amplification in the 10-kHz range," Optics Letts., **15**, 839, 1990.

[11] S.J. Davis, J.E. Murray, D.C. Downs, and W.H. Lowdermilk, "High performance avalanche transistor switchout for external pulse selection at 1.06 μm," Appl. Optics, **17**, 3184, 1978.

[12] D.C. Downs, J.E. Murray, and W.H. Lowdermilk, "Stabilizing the output of a Q-switched laser," IEEE. Journ. Quant. Electron., **14**, 571, 1978.

[13] J.A. Morris and C.R. Pollock, "Passive Q switching of a diode-pumped Nd:YAG laser with a saturable absorber," Optics Letts., **15**, 440, 1990.

[14] R. Beach, J. Davin, S. Mitchell, W. Benett, B. Freitas, and R. Solarz, "Passively Q-switched transverse-diode-pumped Nd^{3+}:YLF laser oscillator," Optics Letts., **17**, 124, 1992.

[15] A.G.Kalintsev, A.A.Mak, L.N.Soms, A.I.Stepanov, and A.A.Tarasov, "Residual losses in passive shutters made from LiF crystals with color centers", Sov. Phys. Tech. Phys., **26**, 1267, 1981.

[16] G.D. Boyd and D.A. Kleinman, "Parametric interaction of focussed Gaussain light beams," Journ. Appl. Phys., **39**, 3597, 1968.

[17] D.R. White, E.L. Dawes, and J.H. Marburger, "Theory of second-harmonic generation with high-conversion efficiency," IEEE. Journ. Quant. Electron., **QE-6**, 793, 1970.

[18] K. Kato, "Second-harmonic and sum-frequency generation to 4150 and 4589A in KTP," IEEE. Journ. Quant. Electron., **QE-24**, 3, 1988.

[19] M.S.Webb, S.P.Velsko, "Temperature Sensitivity of Phase-Matched Second-Harmonic Generation in $LiIO_3$," IEEE. Journ. Quant. Electron., **26,** 1394, 1990.

[20] S.P.Welsko, M.Webb, L.Davis, C.Huang, "Phase-Matched Harmonic Generation in Lithium Triborate (LBO)," IEEE. Journ. Quant. Electron., **27,** 2182, 1991.

[21] N.P. Barnes, D.J. Gettemy, and R.S. Adhav, "Variation of the refractive index with temperature and the tuning rate for KDP isomorphs," Journ. Opt. Soc. Am., **72**, 895, 1982.

[22] B. Boulanger, G. Marnier, J.P. Feve, B. Menaert, X. Cabirol, C. Bonnin, and P. Villeval, "Comparative experimental study of KTA and KTP for the SHG at 1.32 μm and 10.64 μm," Paper JWA2-1, in the OSA Proceedings on Advanced Solid-State Lasers, New Orleans, Louisiana, February 1993.

[23] A.J.W. Brown, M.S. Bowers, K.W. Kangas,, and C.H. Fisher, "High-energy, high-efficiency second-harmonic generation of 1064-nm radiation in KTP," Optics Letts., **17**, 109, 1992.

[24] W. Koechner, "Damage threshold of optical materials," pp.579-586, in "Solid-State Laser Engineering," third edition, published by Springer-Verlag, New York, 1992.

NASA

Report Documentation Page

1. Report No.	2. Government Accession No.	3. Recipient's Catalog No.

4. Title and Subtitle

Final Report for Diode-Pumped Laser Altimeter

5. Report Date

June 1993

6. Performing Organization Code

7. Author(s)

D. Welford and Y. Isyanova

8. Performing Organization Report No.

10. Work Unit No.

9. Performing Organization Name and Address

Schwartz Electro-Optics, Inc.
45 Winthrop Street
Concord, MA 01742

11. Contract or Grant No.

NAS5-30882

12. Sponsoring Agency Name and Address

NASA Goddard Space Flight Center
Greenbelt, MD 20771

13. Type of Report and Period Covered

Final Report
6/1/90-3/31/93

14. Sponsoring Agency Code

NASA GSFC

15. Supplementary Notes

16. Abstract

TEM_{00}-mode output energies up to 22.5 mJ with 23% slope efficiencies were generated at 1.064 μm in a diode-laser pumped Nd:YAG laser using a novel transverse-pumping geometry. 1.32-μm performance was equally impressive at 10.2 mJ output energy with 15% slope efficiency. The same pumping geometry was successfully carried forward to several complex Q-switched laser resonator designs with no noticeble degradation of beam quality. Output beam profiles were consistently shown to have greater than 90% correlation with the ideal TEM_{00}-order Gaussian profile.

A comparison study on pulse-reflection-mode (PRM), pulse-transmission-mode (PTM), and passive Q-switching techniques was undertaken. The PRM Q-switched laser generated 8.3 mJ pulses with durations as short as 10 ns. The PTM Q-switch laser generated 5 mJ pulses with durations as short as 5 ns. The passively Q-switched laser generated 5 mJ pulses with durations as short as 2.4 ns.

We were able to demonstrate frequency doubling of both 1.064 μm and 1.32 μm with conversion efficiencies of 56% in lithium triborate and 10% in rubidium titanyl arsenate, respectively. Sum-frequency generation of the 1.064 μm and 1.32 μm radiations was demonstrated in KTP to generate 1.1 mJ of 0.589 μm output with 11.5% conversion efficiency.

17. Key Words (Suggested by Author(s))	18. Distribution Statement
Diode-pumped, solid-state, laser, Nd:YAG Q-switched	Unclassified - Unlimited

19. Security Classif. (of this report)	20. Security Classif. (of this page)	21. No. of pages	22. Price
Unclassified	Unclassified	95	

NASA FORM 1626 OCT 86